The Effect of Anomalous Resistivity on the Electrothermal Instability

Robert Leo Masti

Dissertation submitted to the Faculty of the
Virginia Polytechnic Institute and State University
in partial fulfillment of the requirements for the degree of

Doctor of Philosophy
in
Aerospace Engineering

Bhuvana Srinivasan, Chair
Colin S. Adams
Wayne A. Scales
Stefano Brizzolara

May 7, 2021
Blacksburg, Virginia

Keywords: High Energy Density Physics, Electrothermal Instability, Anomalous Resistivity, Pulsed-Power

The Effect of Anomalous Resistivity on the Electrothermal Instability

Robert Leo Masti

(ABSTRACT)

The current driven electrothermal instability (ETI) forms when the material resistivity is temperature dependent, occurring in nearly all Z-pinch-like high energy density platforms. ETI growth for high-mass density materials is predominantly striation form which corresponds to magnetically perpendicular mode growth. The striation form is caused by a resistivity that increases with temperature, which is often the case for high-mass density materials. In contrast, low-density ETI growth is mainly filamentation form, magnetically aligned modes, because the resistivity tends to decrease with temperature. Simulating ETI is challenging due to the coupling of magnetic field transport to equation of state over a large region of state space spanning solids to plasmas. This dissertation presents a code-code verification study to effectively model the ETI. Specifically, this study provides verification cases which ensure the unit physics components essential to modeling ETI are accurate. This provides a way for fluid-based codes to simulate linear and nonlinear ETI. Additionally, the study provides a sensitivity analysis of nonlinear ETI to equation of state, vacuum resistivity, and vacuum density. Simulations of ETI typically use a collisional form of the resistivity as provided, e.g., in a Lee-More Desjarlais conductivity table. In regions of low-mass density, collision-less transport needs to be incorporated to properly simulate the filamentation form of ETI growth. Anomalous resistivity (AR) is an avenue by which these collision-less micro-turbulent effects can be incorporated into a collisional resistivity. AR directly changes the resistivity which will directly modify the linear growth rate of ETI, so a new linear growth rate is derived which includes AR's added dependency on current density. This linear growth rate is verified through a filamentation ETI simulation using an ion acoustic based AR model. Kinetically based simulations of vacuum contaminant plasmas provide a physical platform to study the use of AR models in pulsed-power platforms. Using parameters from the Z-machine pulsed-power device, the incorporation of AR can increase a collisional-based resistivity by upwards of four orders of magnitude. The presence of current-carrying vacuum contaminant plasmas can indirectly affect nonlinear ETI growth through modification of the magnetic diffusion wave. The impact of AR on nonlinear ETI is explored through pulsed-power simulations of a dielectrically coated solid metallic liner surrounded by a low-density vacuum contaminant plasma.

The Effect of Anomalous Resistivity on the Electrothermal Instability

Robert Leo Masti

(GENERAL AUDIENCE ABSTRACT)

High-energy-density physics (HEDP) is the study of materials with pressures that exceed 1 Mbar, and is difficult to reach here on Earth. Inertial confinement fusion concepts and experiments are the primary source for achieving these pressures in the laboratory. Inertial confinement fusion (ICF) is a nuclear fusion concept that relies on the inertia of imploding materials to compress a light fuel (often deuterium and tritium) to high densities and temperatures to achieve fusion reactions. The imploding materials in ICF are driven in many ways, but this dissertation focuses on ICF implosions driven by pulsed-power devices. Pulsed-power involves delivering large amounts of capacitive energy in the form of electrical current over very short time scales (nanosecond timescale). The largest pulsed-power driver is the Z-machine at Sandia National Laboratory (SNL) which is capable of delivering upwards of 30 MA in 130 ns approximately.

During an ICF implosion there exists instabilities that disrupt the integrity of the implosion causing non-ideal lower density and temperature yields. One such instability is the Rayleigh-Taylor instability where a light fluid supports a heavy fluid under the influence of gravity. The Rayleigh-Taylor is one of the most detrimental instabilities toward achieving ignition and was one of the main research topics in the early stages of this Ph.D. The study of this instability provided a nice intro for modeling in the HEDP regime, specifically, in the uses of tabulated equations-of-state and tabulated transport coefficients (e.g., resistivity and thermal conductivity). The magneto Rayleigh-Taylor instability occurs in pulsed-power fusion platforms where the heavy fluid is now supported by a magnetic field instead of a light fluid. The magneto Rayleigh-Taylor instability is the most destructive instability in many pulsed-power fusion platforms, so understanding seeding mechanisms is critical in mitigating its impact.

Magnetized liner inertial fusion (MagLIF) is a pulsed-power fusion concept that involves imploding a solid cylindrical metal annulus on laser-induced pre-magnetized fuel. The solid metal liners have imperfections and defects littered throughout the surface. The imperfections on the surface create a perturbation during the initial phases of the implosion when the solid metal liner is undergoing ohmic heating. Because a solid metal has a resistivity that increases with temperature, as the metal heats the resistivity increases causing more heating which creates a positive feedback loop. This positive feedback loop is similar to the heating process in a nichrome wire in a toaster, and is the fundamental bases of the main instability studied in this dissertation, the electrothermal instability (ETI).

ETI is present in all pulsed-power fusion platforms where a current-carrying material has a resistivity that changes with temperature. In MagLIF, ETI is dominant in the early stages of a current pulse where the resistivity of the metal increases with temperature. An increasing resistivity with temperature is connected to the axially growing modes of ETI which is denoted as the striation form of ETI. Contrary to the striation form of ETI, the filamentation form of ETI occurs when resistivity decreases with temperature and is associated with the azimuthally growing modes of ETI. Chapter 2 in this dissertation details a study of how to simulate striaiton ETI for a MagLIF-like configuration across different resistive magneto-hydrodynamics (MHD) codes.

Resistivity that decreases with temperature typically occurs in low-density materials which are often in a gaseous or plasma state. Low density plasmas are nearly collision-less and have resistivity definitions that often overestimate the conductivity of a plasma in certain experiments. Anomalous resistivity (AR) addresses this overestimation by increasing a collisional resistivity through micro-turbulence driven plasma phenomenon that mimic collisional behavior. The creation of AR involves reduced-modeling of micro-turbulence driven plasma phenomenon, such as the lower hybrid drift instability, to construct an effective collision frequency based on drift speeds. Because AR directly modifies a collisional resistivity for certain conditions, it will directly alter the growth of ETI which is the topic of Chapter 3.

The current on the Z-machine is driven by the capacitor bank through the post-hole convolute, the magnetically insulated transmission lines, and then into the chamber. Magnetically insulated transmission lines have been shown to create low-density plasma through desorption processes in the vacuum leading to a load surrounded by a low-density plasma referred to as a vacuum contaminant plasmas (VCP). VCP can divert current from the load by causing a short between the vacuum anode and cathode gap. In simulations, this plasma would be highly conducting when represented by a collisionally-based resistivity model resulting in non-physical vacuum heating that is not observed in experiments. VCP are current-carrying low-density and high-temperature plasmas which make them ideal candidates to study the role of AR as described in Chapter 4. Chapter 4 investigates the role AR in a VCP would have on striation ETI for a MagLIF-like load.

Dedication

To my parents David and Julia, my brothers Ryan and Adam, and my uncle Donnie

Acknowledgments

There are many individuals that have helped and contributed to my journey through these past 5 years, and without them, this dissertation would not have been possible. First and foremost, I would like to thank my advisor, Professor Bhuvana Srinivasan, for the guidance and wisdom in life and in research, and offering me a chance to join the group. Being one of her first Ph.D. students emphasizing in high-energy-density physics I have come to witness how her positivity and diligence helped push students through an often unfamiliar subject. In addition to my advisor, I would like to thank my fellow lab mates, specifically, Dr. Petr Cagas, Dr. Yang Song, Dr. Chirag Rathod, Camille Samulski, Megan McCracken, and Matthew Carrier, for being colleagues, and more importantly, friends during this journey. Lastly, from Virginia Tech (VT), I must thank my committee members, Professor Colin Adams, Professor Stefano Brizzolara, and Professor Wayne Scales, for their time and valuable suggestions.

I have received tremendous support from outside of VT specifically from Tech-X and Lawrence Livermore National Laboratory (LLNL). Dr. Jacob King, from Tech-X, provided oversight and guidance in diagnosing and implementing new tools to address the needs of my research. Dr. Peter Stoltz, from Tech-X, provided the expertise for using USim and had invaluable insight in how to approach simulations. Dr. C. Leland Ellison, formerly of LLNL, is chiefly responsible for crafting myself into the researcher I am today, his contributions to my Ph.D. were insurmountable for which I am grateful. Dr. William Farmer, from LLNL, provided valuable theoretical insight toward the later stages in my Ph.D. and helped to conglomerate my research into a dissertation. Outside of VT and LLNL, I have received valuable feedback for many presentations from my colleague and my dear friend, Peter Artuso. Lastly, I would like to acknowledge Annalee Mishrell, Rose Mishrell, Camille Samulski, and Megan McCracken for revising and editing this dissertation.

This work was supported through the Lawrence Livermore National Laboratory Weapons and Complex Integration (LLNL WCI) High Energy Density Fellowship, and through the US Department of Energy under grants DE-SC0016515 and DE-NA0003881. In addition, a portion of this work was sponsored by LLNL WCI HED summer program. This research used resources of the National Energy Research Scientific Computing Center (NERSC), a U.S. Department of Energy Office of Science User Facility operated under Contract No. DE-AC02-05CH11231. A portion of this work was performed under the auspices of the U.S. Department of Energy by Lawrence Livermore National Laboratory under Contract DE-AC52-07NA27344. This document was prepared as an account of work sponsored by an agency of the United States government. Neither the United States government nor Lawrence Livermore National Security, LLC, nor any of their employees makes any war-

This document has been approved for public release under the identifier LLNL-TH-816591.

Contents

Chapter 1

Introduction

Controlled nuclear fusion is the pinnacle of energy sources and has been sought after for generations. The fundamental premise behind nuclear fusion involves combining two light nuclei to create a heavier nucleus. The rest mass energy, $E_0 = mc^2$, of the heavier nuclei is less than the sum of the two lighter rest mass energies, and the difference is the energy released from a nuclear fusion reaction. The location of two nuclei on the nuclear binding energy curve shown in Figure 1.1 determines their ability to fuse and release energy. Fusing two nucleons on the left side of the peak in this figure results in a net release of energy, whereas fusing two nucleons on the right side of the peak in this figure requires additional energy[1]. The peak in this curve represents the most stable elements from a nuclear binding energy perspective and example of one such element is iron (Fe).

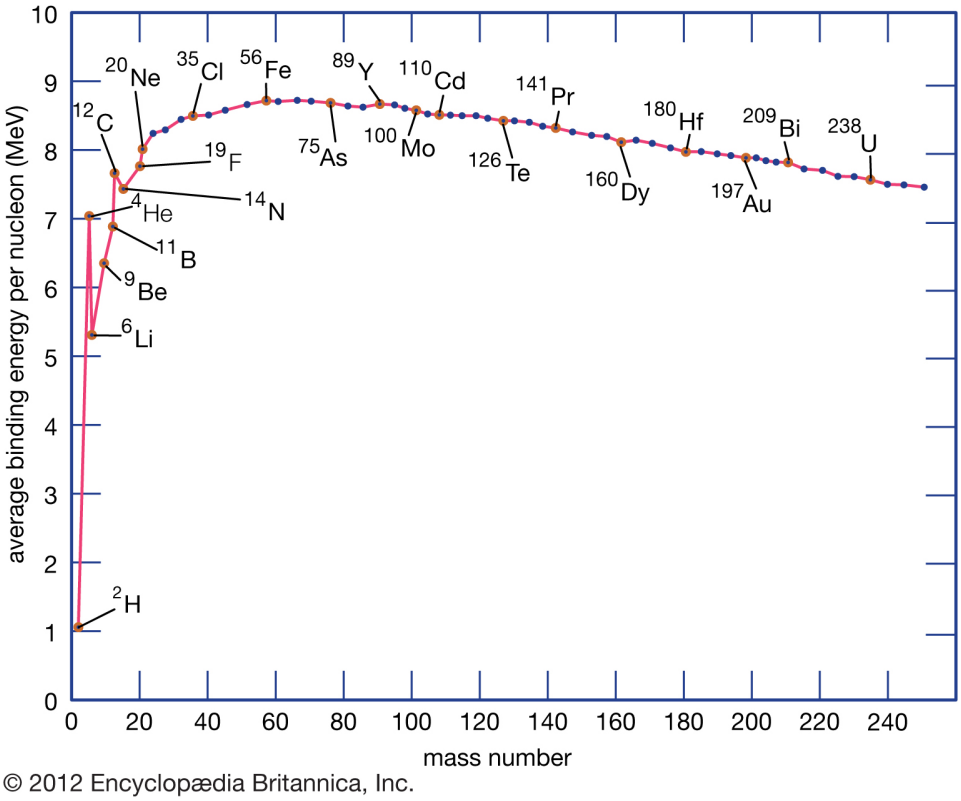

Figure 1.1: Nuclear binding is presented for varying atomic mass number. Source: link

Nuclear fission is the process where heavy nuclei split releasing energy through radioactive decay. Nuclear fission occurs with a net release of energy on the right side of the peak in Figure 1.1. A nuclear fission reaction of, e.g., uranium-235, would release around 200 MeV of energy per reaction. A nuclear fusion reaction, for example deuterium-tritium, only releases around 14 MeV which is significantly less than a nuclear fission reaction. Although a nuclear fusion reaction releases less energy than a nuclear fission reaction on a per-reaction basis, on a per-mass basis, nuclear fusion reactions release significantly more energy than nuclear fission reactions. Additionally, nuclear fusion does not suffer from the issue of radioactive waste as nuclear fission does in the form of spent fuel rods. There are many more benefits to achieving controlled nuclear fusion not discussed here[1].

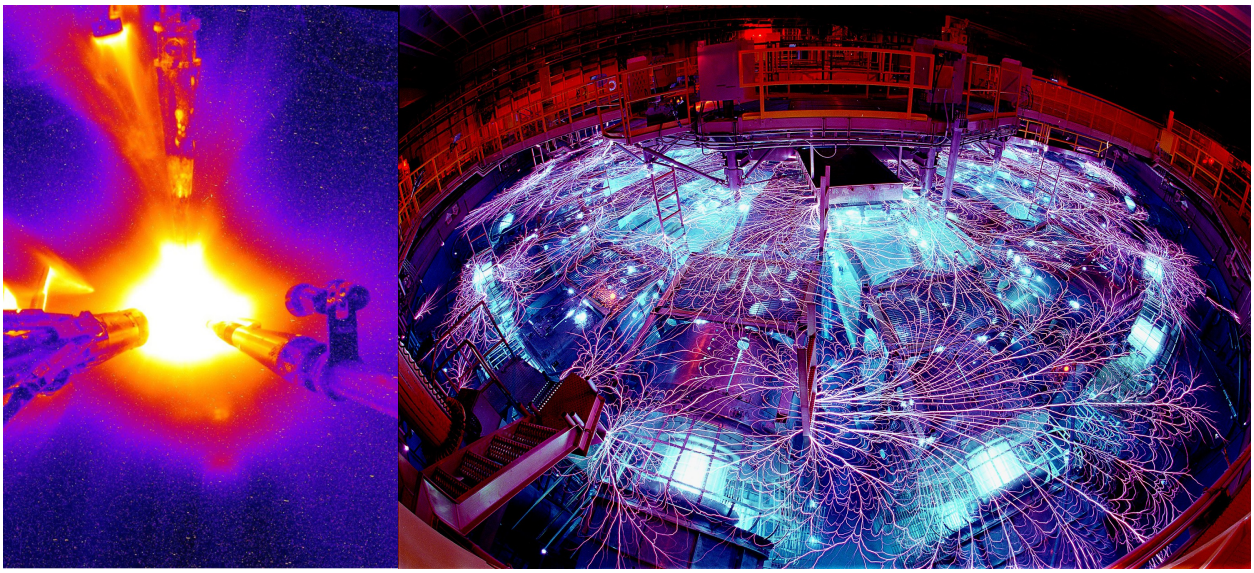

Figure 1.2: These figures present experimental examples of inertial confinement fusion implosions. The left image is of a shot at the National Ignition Facility sourced from LLNL link involving the use of lasers. The right image is of a shot at the Z-machine sourced from SNL link involving pulsed-power.

There are many benefits to achieving controlled nuclear fusion, but actually achieving it is **extremely difficult**. Nuclei are positively charged and combining them requires penetrating the Coulomb barrier of repulsion (like charges repel). In order to have a chance of penetrating this barrier, two nuclei will have to undergo a collision, and to achieve this requires pushing light nuclei materials to high number density. In addition to having high number density, the nuclei must be hot enough to have the necessary kinetic energy needed for the collision to exceed the Coulomb barrier. Density provides the collision frequency needed, and temperature provides the kinetic energy needed for a fusion reaction to take place. These requirements are often summarized in the Lawson criterion which provides a threshold to determine how dense, how hot, and how long one must hold nuclear fuel before fusion reactions produce net fusion energy (energy output exceeds input)[2]. These three

criteria can be met through different approaches, but the primary focus of this dissertation is on the inertial confinement fusion approach.

Inertial confinement fusion (ICF) approaches the Lawson criterion through achieving very high densities and temperatures at the expense of short time scales (examples shown in Figure 1.2). The ICF approach primarily involves accelerating a pusher to high velocities letting its inertia compress a light density fuel[1] to fusion conditions. There are many ways to accelerate this pusher, but the one of interest in this dissertation is through the form of electrical current (Section 1.1). The pusher in ICF implosions can compress nuclear fuel to very high mass density ($1 \times 10^6\,\mathrm{kg\,m^{-3}}$) and very high temperatures (greater than 10 keV)[2], and the study of materials at these densities and temperatures is referred to as high energy density (HED) science[3]. For a material to be in a HED state it must be at pressures higher than 1 Mbar which is easy to achieve in ICF where high densities and temperatures are reached[3].

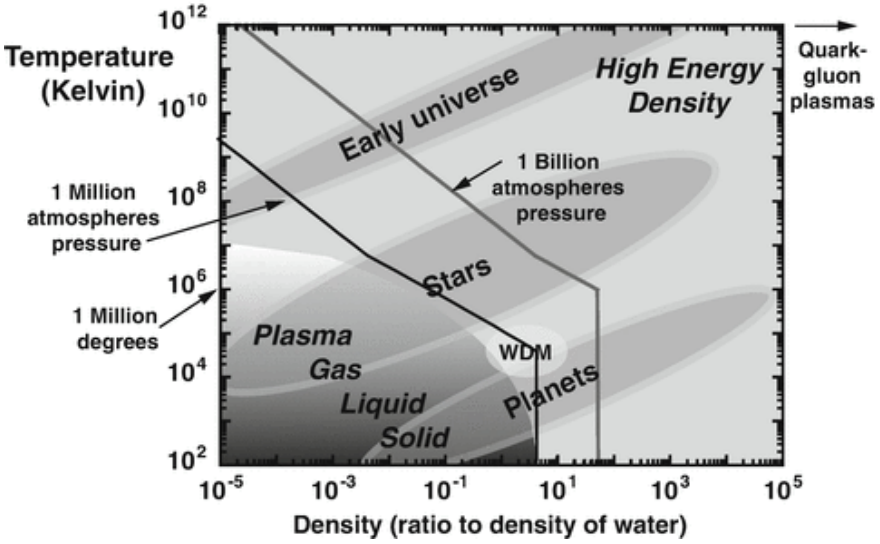

Figure 1.3: This plot shows Figure 1.1 of Drake [3], and depicts the region of high energy density on a log temperature and log density scale. For reference 1 million atmospheres pressure is 1 Mbar and denotes the approximate transition line into the high energy density regime.

Reaching a HED state in an ICF implosion often happens at large ICF facilities such as the National Ignition Facility at Lawrence Livermore National Laboratory (LLNL), and the Z-machine at Sandia National Laboratory (SNL) shown in the left and right images of Figure 1.2, respectively. However, these facilities cannot be run continuously as they take time to set up the target and prepare the energy for the shot, and this time is characterized by a "repetition rate" for a device. The finite repetition rate of these facilities limit the opportunities for discovery, which is the main drive for developing ICF implosion concepts

[1]Fuel in fusion lingo refers to material that have small atomic number such as hydrogen.

through simulations. Simulations are great in their lack of an associated repetition rate[2], but this often comes at a cost of accuracy when compared to the experimental results. Simulations in the HED regime are challenging due to a myriad of factors, such as non-ideal equations of state, electrical and thermal transport mechanisms, small temporal and spatial scales, radiation mechanics, etc. These ICF implosions often produce plasmas[3] which can add even more complexity and challenges to the already challenging HED simulation regime.

1.1 Pulsed-Power

Pulsed-power refers to delivering massive amounts of stored capacitive energy to a target in the form of electrical current. It is widely known, from fundamental electricity and magnetism[4], that two current carrying wires with current flow in the same direction experience an attractive force[4][4]. This fundamental force, often denoted as the $\mathbf{J} \times \mathbf{B}$ force in pulsed-power, is what drives the implosion for the pulsed-power driven ICF platform known as a Z-pinch[5]. The currents required to achieve HED states are on the order of 1×10^6 A, and the largest pulsed-power device in use today is the Z-machine which is able to drive currents up to 26 MA[6]. The Z-machine achieves these peak currents in a short amount of time, around 100 ns, and provides an excellent source of X-ray emissions with peak emissions at 350 TW[6].

Currently, the Z-machine uses a ring of 36 Marx-generator capacitor banks with each generator composed of 60 2.6 µF capacitors which in totality store 22 MJ of energy[6]. The banks are then triggered and the energy released enters a pulse forming region which connects to magnetically insulated transmission lines (MITL) which then deliver the stored energy to the target[6]. The MITLs deliver the large current exiting the pulse forming network to the load, and in doing so heat causing desorption of molecules such as water[7, 8]. The desorption in these MITLs creates low-density and high-temperature plasma which enter the target chamber and cause unwanted shorting of the current from the load[8]. The low-density high-temperature plasmas will be referred to as vacuum contaminant plasmas (VCP) and are a point of emphasis in this dissertation, primarily in Chapters 3 and 4. The targets shot on the Z-machine vary, but the one of interest for this dissertation is the magnetized liner inertial fusion (MagLIF) target[9].

[2] They do have an associated computation time, but this is mush less than the time it takes to have an experiment performed at one of the aforementioned facilities.

[3] a plasma is a quasineutral gas of charged and neutral particles which exhibits collective behavior[2]

[4] A magnetic field can only exert force on a moving charge

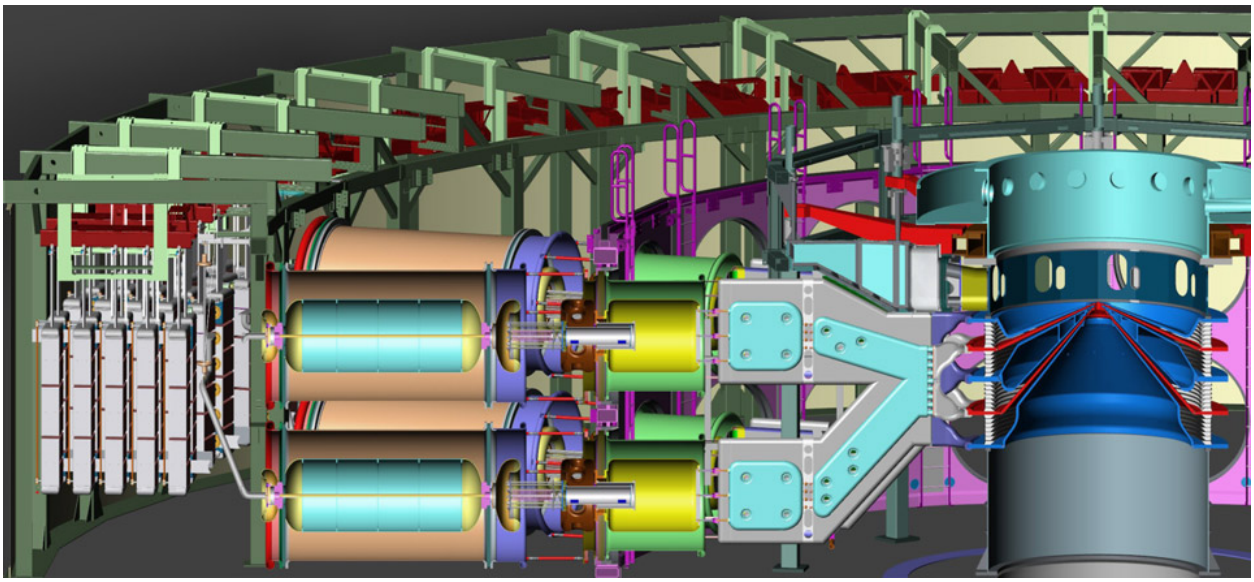

Figure 1.4: This provides an illustration of how the Z-machine works (source=SNL link), note the magnetically insulated transmission lines are on the right where the red and blue lines converge.

1.2 Magnetized liner inertial fusion

Figure 1.5 presents an overview of the MagLIF target and how it is intended to function. MagLIF involves imploding a dielectrically coated cylindrical metallic liner onto a laser induced pre-magnetized nuclear fuel (deuterium and tritium). This is accomplished by first supplying an externally applied magnetic field which diffuses into the MagLIF load such that the field lines enter and exit the top and bottom surface of the cylindrical target. Once the axial field is in place inside the center of the MagLIF load a laser is triggered to preheat the fuel causing it to magnetize or "lock" the magnetic field into place[2]. The laser causes the fuel to heat and as the fuel heats it eventually ionizes and enters a plasma state. Once in a highly conductive plasma state the magnetic field is locked in(see Alfvén's Theorem[2, 10]). After magnetizing the fuel the liner is imploded using pulsed-power, but laser-driven liner implosions has also been pursued[11].

What makes MagLIF an innovative fusion concept is that it incorporates benefits of magnetic confinement into an ICF platform. Magnetic confinement fusion will not be discussed here, but one of the main benefits is the ability to direct plasma/fuel with magnetic fields. For the case of MagLIF, pre-magnetizing the fuel increases the uniformity of the fuel burn by increasing fuel temperature through α particle[5] trapping[13], and stabilizing against instabilities that disrupt the liner integrity[14]. As MagLIF implodes, it compresses the pre-magnetized fuel lines which then increase the local magnetic field through flux compression[15]. Magnetic

[5] An α particle consists of two neutrons and two protons.

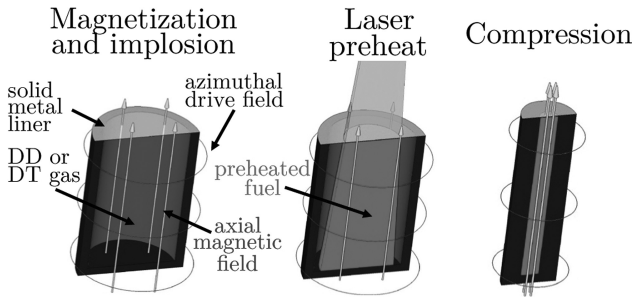

Figure 1.5: This schematic is Figure 1 from Sefkow et al. [12] displaying the main components of magnetized liner inertial (MagLIF).

flux compression hinges on magnetic flux conservation for an infinitely conductive fluid[2]. MagLIF on the Z-machine has reached convergence ratios (ratio of initial liner radius to liner radius at peak burn) of approximately 40 which implies a maximum magnetic flux compression [6] factor of 1600. For an initial axial magnetic field of 20 T a convergence ratio of 40 would result in a peak magnetic field of 3200 T which greatly inhibits undesirable α particle transport.

1.3 Rayleigh-Taylor instability

The previously mentioned axial magnetic field in MagLIF helps stabilize against disruptive instabilities that compromise the liner shape and integrity. One of the most disruptive instabilities in all of ICF is the Rayleigh-Taylor (RT) instability, which involves a light fluid supporting a heavy fluid under the influence of a gravitational acceleration[16]. In conducting fluids, an appropriately aligned magnetic field stabilizes against this instability[16]. Specifically, the magnetic field must be aligned parallel to the perturbation wave vector for any stabilizing effect[17]. In the early stages of MagLIF development, Sinars et al. [14] experimentally studied the magneto RT (MRT) instability[6] on the Z-machine. This paper provided a guide for the first two years of this journey which culminated in an interesting discovery for the proper handling of equation-of-state in a finite-volume code[18].

Figure 1.6 presents the impact an axial magnetic field has on MRT growth through images of density as a function of x and y following Sinars et al. [14]. The left plot shows the growth without an axial magnetic field, and the right plot shows the growth with an axial magnetic field. The impact of the magnetic field is apparent on the fine scale structure which are notably absent on the right plot. The distance between the bubble and spike in the mode growth of MRT is a good indicator for measuring instability growth. Although it is not apparent in Figure 1.6 it is apparent in Figures 5.6 and 5.5 in Chapter 5. The MRT

[6] magneto RT is a special case because the heavy fluid is supported by a magnetic field instead of a light fluid

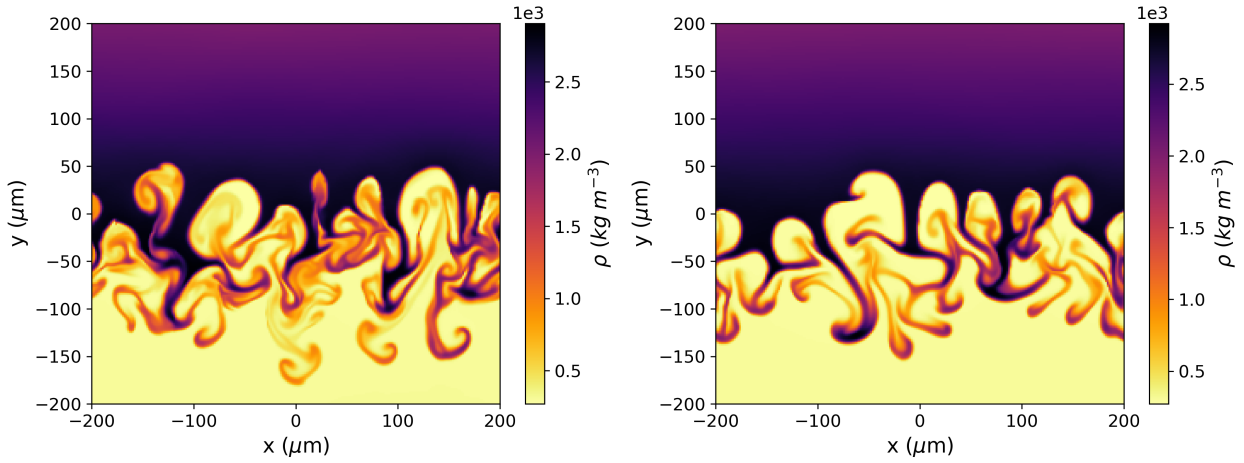

Figure 1.6: These plots present examples of Rayleigh-Taylor (RT) instability growth from Srinivasan et al. [17], where the heavy fluid (aluminum) on the top is supported by the light fluid (vacuum) on the bottom with a downward acceleration based on a MagLIF drive[**?**]. The left plot shows RT growth without a horizontal magnetic field and the right shows RT growth with a horizontal magnetic field[19].

instability only occurs when a perturbation or a seed is present[7], and mitigating these seeds will mitigate the growth of RT. The electrothermal instability (ETI) is the main instability studied in this dissertation (see Chapter 1.5 for details on ETI), and its seeding of MRT is its main motivation. In this dissertation, resistive magnetohydrodynamics simulations are used to study various aspects of ETI, including the influence of anomalous resistivity (AR) on its growth.

1.4 Resistive Magnetohydrodynamics

Magnetohydrodynamics (MHD), has been utilized for over 6 decades dating back to its origins in the 1940s[10]. Resistive-MHD is an extension of MHD which includes electrical resistive effects. Plasmas are inherently conducting[2], and because of this MHD serves as a vital tool for studying plasma-based phenomenon such as the MRT instability. The MHD equations are broken into conservation equations for mass, momentum, and energy, and the induction equation which are given by

$$\frac{\partial \rho}{\partial t} + \nabla \cdot [\rho \mathbf{u}] = 0, \tag{1.1}$$

$$\frac{\partial \rho \mathbf{u}}{\partial t} + \nabla \cdot \left[\rho \mathbf{u}\mathbf{u}^T - \frac{\mathbf{B}\mathbf{B}^T}{\mu_0} + \mathbb{I}\left(P + \frac{|\mathbf{B}|^2}{2\mu_0} \right) \right] = 0, \tag{1.2}$$

[7] There exists unstable equilibriums!

$$\frac{\partial \epsilon}{\partial t} + \nabla \cdot \left[\left(\epsilon + P + \frac{|\mathbf{B}|^2}{2\mu_0} \right) \mathbf{u} - \frac{1}{\mu_0} \mathbf{B} \cdot \mathbf{u}\mathbf{B} \right] = S_\epsilon, \tag{1.3}$$

and

$$\frac{\partial \mathbf{B}}{\partial t} = -\nabla \times \mathbf{E}, \tag{1.4}$$

where μ_0, ρ, $\mathbf{u}$, P, ϵ, $\mathbf{E}$, and $\mathbf{B}$, are the magnetic permeability of free space, mass density, 3D velocity, total pressure, total energy density, electric field vector, and magnetic field vector, respectively[20]. S_ϵ represents the source terms on the energy equation, e.g., ohmic heating. These equations are primarily work horse for many of the simulations done in the pulsed-power community[14, 21, 22, 23, 24, 25]. In resistive-MHD, the electric field, $\mathbf{E}$, is

$$\mathbf{E} = -\mathbf{u} \times \mathbf{B} + \eta \mathbf{j}. \tag{1.5}$$

Equations 1.1- 1.5 are not yet closed, it requires an equation-of-state (EOS). Specifically, there needs to be a relation of pressure (or internal energy density) to density and temperature to close the equation system. In plasma physics this is often just specified using the ideal gas EOS[2]. However, in simulations of pulsed-power ICF platforms the ideal gas EOS is not sufficient for covering the wide array of states that exist in an implosion. The use of an EOS that spans large ranges in temperature and density can address this issue, which in practice is done through EOS tables (pressure and specific internal energy density on a density and temperature grid)[26, 27]. The development of these tables is an active area of research which has seen the use of molecular dynamic simulations and density functional theory for construction[28]. In addition to tabulated EOS, there are tables for transport coefficients, which for resistive-MHD, is just electrical resistivity (η)[29][8].

Hyperbolic and parabolic partial differential equations are solved using a wide array of techniques[30]. This dissertation will isolate the use of finite-volume codes, which discretize the weak (integrated equality) form of the above equations. Finite-volume methods uses the notion of zones or cells to represent a fluid, where each cell has a constant value associated with the variable given above, e.g., density. In addition to spatial discretization, there is temporal integration as well, all of which are provided in Chapter 2 in detail. Chapter 2 presents how different choices of numerical techniques across two different codes can impact ETI growth as shown in Figure 1.9.

1.5 Electrothermal Instability

ETI is the main subject of this dissertation, and connects Chapters 2- 4. ETI occurs for any material whose resistivity depends on temperature and undergoes ohmic heating. Some of the most common occurrences of ETI are for materials at solid density such as a perturbed

[8] Note, resistive-MHD can also include the use of thermal conductivity which is not explicitly stated and does not change the classification to extended-MHD

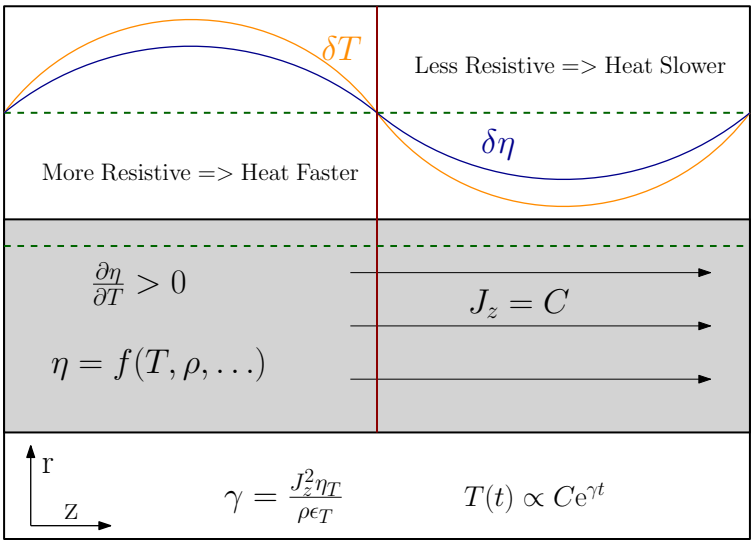

Figure 1.7: This shows a schematic of ETI growth. The gray region is the conducting material which contains a uniformly distributed current which then perturbed in the axial direction causes unstable ohmic heating → ETI growth.

nichrome wire subjected to electric current. The regions of the highest perturbed resistivity will see the largest power generated from ohmic heating (I^2R). Ohmic heating increases the temperature and as a result resistivity (if resistivity increases with temperature), leading to an unstable positive feedback loop. ETI is also referred to as the joule heating instability, and overheat instability[21]. A schematic showing one of the forms of ETI growth is shown in Figure 1.7. A uniformly distributed current that is perturbed along the axial direction, in an annulus, will cause axial non-uniform ohmic heating that increases in intensity, called the ETI (i.e., striation form).

There are two forms of ETI discussed in this work: the first is the striation form of ETI and the second is the filamentation form of ETI. The striation form of ETI is associated with magnetically perpendicular growing modes, and often only occurs at high density because the resistivity tends to increase with temperature in this regime. The filamentation form of ETI is associated with magnetically parallel growing modes, and occurs at lower density where the resistivity tends to decrease with temperature. The sign of $\partial\eta/\partial T$ determines what type is growing. Although this instability is always present in pulsed-power ICF platforms throughout an implosion, it is a rather weak instability in comparison to MRT. The MRT instability can physically disrupt the pusher and often quickly overshadows the ETI[22]. ETI is not as disruptive as MRT, but it can still seed MRT and be a cause for concern in a pulsed-power ICF implosion. For MagLIF, in between when MRT overtakes ETI there is a small "electro-choric" instability phase which is not explored in this dissertation[31].

ETI applied to MagLIF has been an active area of research[20, 22, 23, 24, 32, 33], but the instability has been addressed through the use of dielectric coatings on the surface of

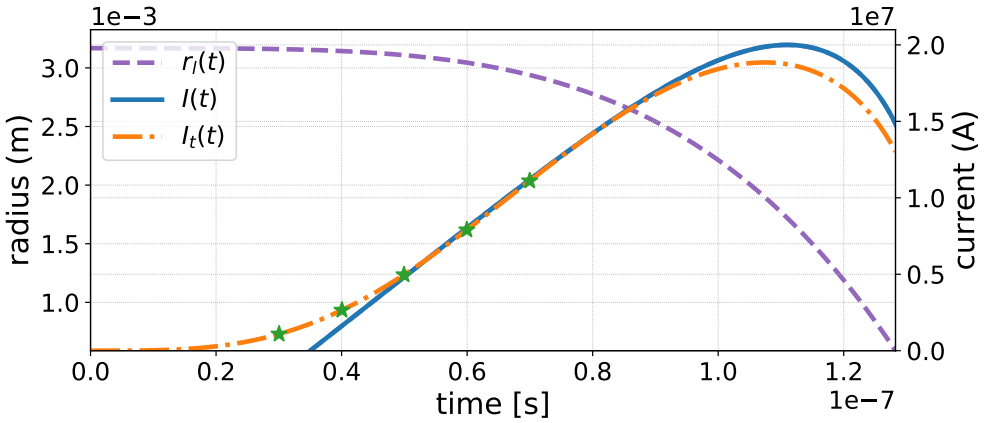

Figure 1.8: This plot presents current as a function of time (along with outer liner radius) including a pre-pulse and without a pre-pulse with the former being critical for simulating ETI[20] (see Chapter 2).

a MagLIF liner[24, 32]. These dielectric coatings serve as a mass tamper which inhibit expansion of the liner as it heats initially from ohmic heating[24]. An important aspect that is often overlooked when simulating ETI in a MagLIF-like load is the structure of the current pulse. From the original MagLIF paper (Slutz et al. [9]) the analytical form of current as a function of time used a linear rise with a peak at approximately 100 ns, as shown in Figure 1.8. This form of current is fine for running late stage large scale MRT simulations, but for ETI which is on the µm length scale it is sensitive to the structure of the pulse early in time. Chapter 2 details what numerical techniques and simulation choices impact ETI modeling including sensitivity to vacuum resistivity, vacuum density, and EOS.

ETI has been experimentally shown to seed the MRT instability for the MagLIF concept[22, 23, 24, 32]. Understanding the formation of ETI is key to help mitigate the seeding of the disruptive MRT instability. The "fast" form of ETI occurs when the skin depth is much larger than the thickness of the liner and results in an ETI growth rate of[5, 22]

$$\gamma = \frac{1}{2}\left[\gamma_z - \gamma_0 + \sqrt{(\gamma_z - \gamma_0)^2 - 4\gamma_0\gamma_z \cos 2\alpha}\right], \tag{1.6}$$

where $\gamma_z = \frac{\partial \eta}{\partial T} J_z^2/(\rho \epsilon_T)$ (striation ETI growth rate), $\gamma_0 = 2\eta|\mathbf{k}|/(\mu_0 h)$ (characteristic current penetration time), and α is the angle between the perturbation wavevector $\mathbf{k}$ and the magnetic field. η, T, J_z, ρ, ϵ_T, μ_0, and h, are the resistivity, temperature, axial current density, mass density, derivative of specific internal energy density with respect to temperature, permeability of free space, and characteristic shell height, respectively. A linear growth rate is used to compare theory with simulation and is obtained through linearizing the equation system (Equations 1.1-1.5) and extracting the first order terms by neglecting the higher order terms. In application to ETI, one can track the exponential growth of a temperature perturbation through time and compare this to the growth rate (see Chapters 2 and 3 for examples). Filamentation ETI occurs when the perturbation is aligned with the azimuthal

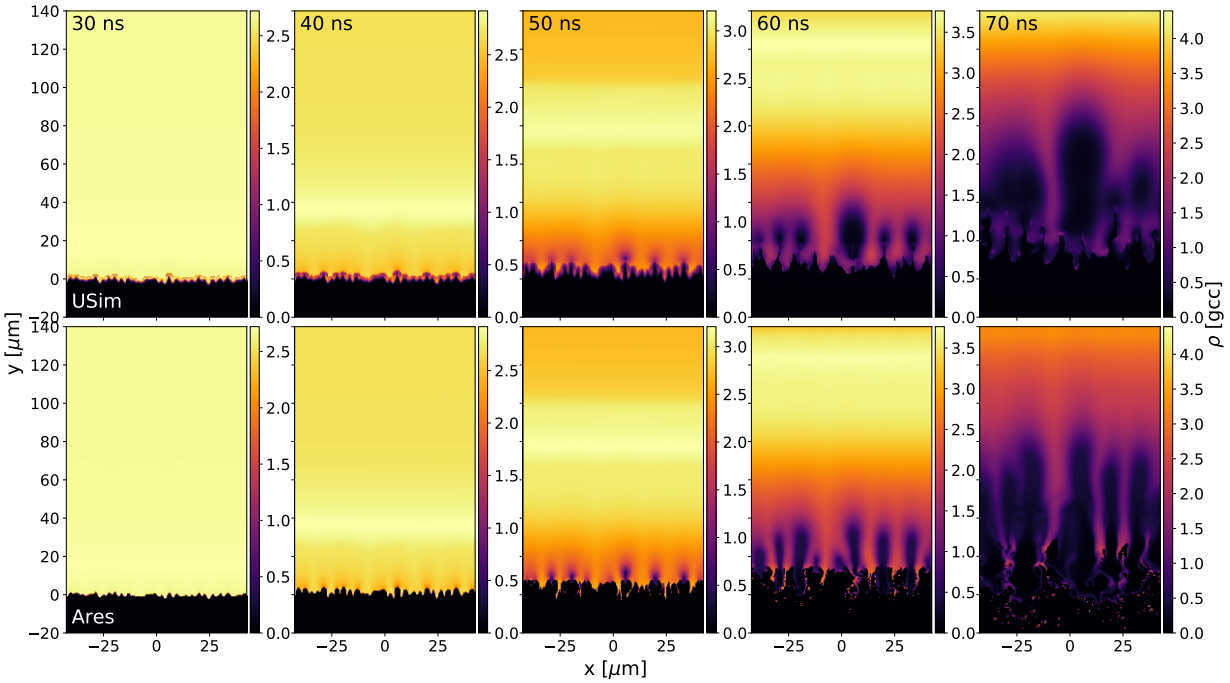

Figure 1.9: Density as a function of space for a set of points in time (correspond to green stars in Figure 1.8) is plotted as an example of nonlinear ETI growth[20].

magnetic field direction ($\alpha = 0°$), and the linear growth rate is

$$\gamma = \frac{1}{2}\left[\gamma_z - \gamma_0 + \sqrt{(\gamma_z - \gamma_0)^2 - 4\gamma_0\gamma_z}\right].$$

Simulations of ETI typically use a collisional form of the resistivity as provided, e.g., in a Lee-More Desjarlais conductivity table[29]. However, in regions of low density a collisional form of resistivity is not sufficient, collision-less transport needs to be incorporated to properly simulate the filamentation form of ETI growth. Anomalous resistivity (AR) is an avenue by which collision-less micro-turbulent effects can be incorporated into a collisional resistivity[34, 35] (see Chapter 1.6). Filamentation ETI has not been of particular interest to the pulsed-power community in recent years, but with garnered interest on vacuum contaminant plasmas, the filamentation ETI in pulsed-power warrants discussion[7, 8]. These current carrying low density vacuum contaminant plasmas are a prime candidate for studying AR. Chapter 3 evaluates the impact of AR on Equation 1.6 through the derivation of a new linear growth rate.[9] Lastly, Chapter 4 presents how AR indirectly influences the striation form of the ETI through modifying the evolution of the magnetic diffusion wave.

[9]AR and ETI can also be applied to gas puff Z-pinches where instead of a solid liner like MagLIF has, they have a gaseous liner[36, 37].

1.6 Anomalous Resistivity

Anomalous resistivity is an augmentation of a collisionally based resistivity through micro turbulent instabilities that exhibit collision-like behavior. For example, some of these micro turbulent instabilities are manifestations of collision-less phenomenon such as the ion acoustic wave[34, 38, 39, 40, 41, 42], the lower hybrid drift instability[35, 43], and the Buneman instability[34, 43, 44]. Historically, AR models have mostly been applied to atmospheric plasmas and have not, until recently, been applied to plasmas in HED fusion concepts[35, 45].

AR models are created using quasilinear theory[34, 43, 46] and kinetic simulations[35, 46]. These AR models manifest into resistivity through development of an AR characteristic collision frequency of the form

$$\eta_{\text{AR}} \equiv \sigma^{-1}\tau_{ei}\nu_{\text{AR}} = \frac{m_e m_i}{e^2 Z_{\text{eff}}\rho}\nu_{\text{AR}}, \tag{1.7}$$

where η_{AR}, σ, m_e, m_i, e, Z_{eff}, ρ, and ν_{AR}, are AR resistivity, collisional conductivity, electron mass, ion mass, elementary charge, effective ionization level, mass density, and AR electron scattering frequency, respectively. This form of η_{AR} assumes a Spitzer-like form of the resistivity proportional to the electron-ion collision frequency. Additionally, Equation 1.7 incorporates the collisional resistivity through τ_{ei} and the effective AR collision frequency ν_{AR} which can be an individual frequency or a sum of frequencies dependending on whether one or multiple AR models are used. This total η_{AR} resistivity is then added into the collisional resistivity to get the effective resistivity as simply

$$\eta_{\text{eff}} = \eta + \eta_{\text{AR}},$$

where η is the collisional resistivity which can be of any form (analytical, tabulated, etc.). For the work in this dissertation, a tabulated collisional resistivity is primarily used. Figure 1.10 presents this incorporation into a tabulated conductivity and shows that AR can change the collisional resistivity by upwards of 12 orders of magnitude.

AR couples to ETI directly through changes in γ_z and γ_0 in Equation 1.6. Specifically, AR will change γ_z through changes in the derivative of resistivity with respect to temperature, and will change γ_0 through changes in the resistivity alone. With no experimental validation and so many available AR models, it is difficult to discern which AR model or combination of models is the most accurate. However, all of these models are dependent on the drift speed of electrons, so current-carrying low density vacuum plasmas are prime candidates to investigate AR with respect to ETI. Chapters 3 and 4 study how AR influences the "fast" form of ETI both directly and indirectly.

Although AR is shown to not have a significant impact on the striation form of ETI directly, as discussed in Chapter 3, it can impact the striation form of ETI indirectly through the magnetic diffusion wave. The magnetic diffusion wave occurs numerically in resistive-MHD simulations through magnetic field accumulation in the liner. Pulsed-power simulations

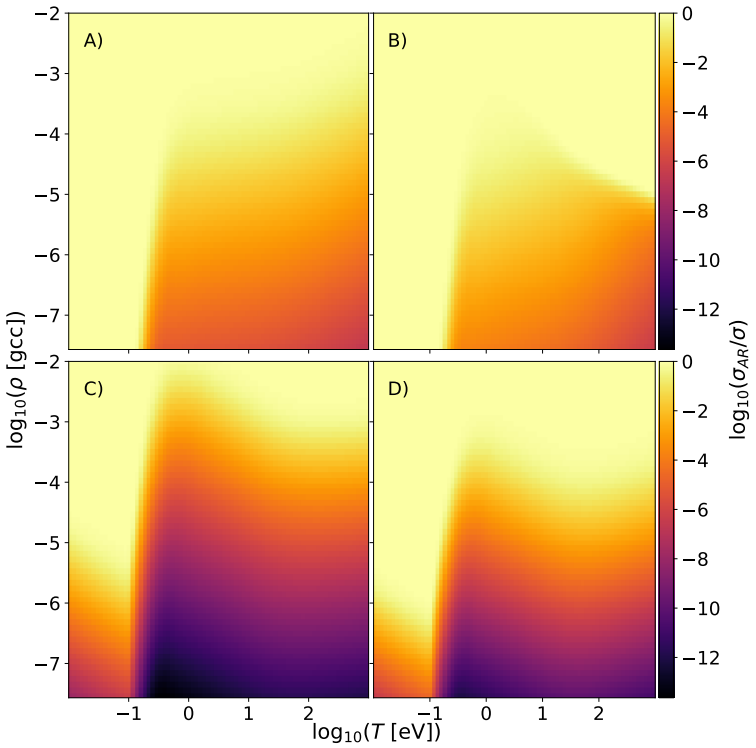

Figure 1.10: Plot of $\eta_{\text{table}}/\eta_{\text{eff}}$ (note $\sigma = 1/\eta$) for aluminum with a current density of $j = 1.8 \times 10^{11}\,\text{A}\,\text{m}^{-2}$. A), B), C), and D), represent the ion acoustic, Buneman, Davidson LHD, and Tummel LHD AR models, respectively [47].

are usually driven by injected magnetic flux at the outer radial boundary (in cylindrical coordinates). The magnetic field diffuses dynamically into the liner which results in a build up of magnetic field through a wave that manifests in mass density[22]. This "magnetic diffusion wave" controls the current distribution over time which can affect the striation ETI growth in a MagLIF liner. Chapter 4 examines how AR's manipulation of the magnetic diffusion wave influences the subsequent ETI growth in the presence of current-carrying vacuum contaminant plasmas[7].

1.7 Structure and Content

This dissertation follows the *Manuscript* format and the next three chapters each consist of a peer-reviewed journal publication. The dissertation is divided into two parts focusing on modeling ETI, Chapter 2, and assessing AR influence on ETI, Chapters 3 and 4.

The content of each chapter is as follows:

Chapter 1: is divided into an ETI section which introduces ETI, pulsed-power, HED,

MagLIF, and the "fast" thermal form of ETI growth rate, and an AR section which introduces AR, the elevant quantities therein, applications, and how it couples to ETI.

Chapter 2: Consists of a peer reviewed paper, entitled "*Cross-Code verification and sensitivity analysis to effectively model the electrothermal instability*" and published in the Journal of High Energy Density Physics[20]. This paper presents the important aspects of modeling ETI from a numerical algorithm level, and investigates nonlinear ETI sensitivity to the equation-of-state, vacuum density, and vacuum resistivity. Additionally, this paper provides a verification test suite for the important individual components of ETI such as magnetic diffusion and ohmic heating.

Chapter 3: Consists of a peer reviewed paper, entitled "*The effect of anomalous resistivity on the fast electrothermal instability*" and to be submitted following post-review revisions to the Physics of Plasmas (or journal of Plasma Physics). This paper presents anomalous resistivity models and how they change the effective resistivity with Z-machine-like conditions. Additionally, a newly derived growth rate is included that incorporates a resistivity dependence on current density. This growth rate is then verified through simulation of filamentation ETI with and without AR included.

Chapter 4: Consists of a peer reviewed paper, entitled "*The impact of anomalous resistivity in vacuum contaminant plasmas on the electrothermal instability*" in a completed state in preparation for submission to a journal. This paper presents the indirect impact anomalous resistivity has on the electrothermal instability for a MagLIF-like configuration through the magnetic diffusion wave. The magnetic diffusion wave is shown to vary in the delay of the peak liner current location across the different anomalous resistivity models using 1D simulations. These delays manifest into different evolutions of ETI and are shown through 2D simulations.

Chapter 5: Culminates the main takeaways from the previous sections and provides an avenue for future work.

1.8 Contributions

The main contributions of this dissertation towards the modeling of ETI are the following:

1. Provides a verification test suite that evaluates a code's handling of equations directly relevant to ETI such as the induction and energy equation.
2. Highlights what aspects of a numerical scheme are most important in modeling ETI, e.g., time integration of parabolic equations.
3. A sensitivity analysis of nonlinear ETI to vacuum conditions shows insensitivity to vacuum density and sensitivity to vacuum resistivity.

4. A liner-to-vacuum resistivity ratio of 1.0×10^4 obtains the converged result, converged meaning in the limit of near infinite vacuum resistivity (ratio of greater than 1.0×10^{10}).

5. Nonlinear ETI is shown to be highly sensitive to equation-of-state in the high density and low temperature region of state space.

The main contributions of this dissertation towards determining the role of AR in ETI growth are the following:

1. The regimes in which AR is relevant to 1.0×10^7 A pulsed-power machines are at low densities (under $1.0 \times 10^{-3}\,\mathrm{g\,m^{-3}}$).

2. AR is only applicable in the region where $\partial\eta/\partial T < 0$ at these lower densities meaning it is significant to filamentation ETI growth.

3. AR is conversely shown to not influence the striation ETI when using conditions typical of Z-machine pulsed-power machines, but it can begin to play a role at much larger current densities.

4. A newly derived growth rate shows that resistivity dependence on current density will affect the filamentation ETI only and is supported through basic physics arguments.

5. The new growth rate is verified through simulation and the added current density dependence is shown to reduce the magnitude of growth over time.

The main contributions of this dissertation towards determining the impact of AR in VCP on ETI are the following:

1. VCP parasitically divert current away from the drive and in resistive-MHD simulations, this results in a delay of the current pulse penetrating the liner.

2. AR in VCP is shown to mitigate this delay equally for both a dielectrically-coated aluminum and beryllium liner.

3. For MagLIF-like settings this delay is shown to be around 8 ns at 60 ns and is reduced to nearly 0 ns through use of AR models DA, KT, and IA. The BU AR model is shown to reduce only by 4 ns.

4. The 2D simulations show a two-fold reduction in the delay due to 2D turbulence disrupting the VCP layer early in time.

5. Significant RT mode growth is observed on the outside of the dielectric and varies with AR model.

6. The beryllium liner simulations show the largest variation in ETI growth across AR models, and the aluminum liner simulations show very little variation.

7. The aluminum liner simulations show the largest variation in peak liner current density across the AR models conversely to the beryllium liner simulations.

1.9 Publications

Peer-reviewed journal publications related to the modeling ETI:

- **Robert L. Masti**, C. Leland Ellison, Jacob R. King, Peter H. Stoltz, and Bhuvana Srinivasan. *Cross-Code verification and sensitivity analysis to effectively model the electrothermal instability.* Journal of High Energy Density Physics, 2021.https://doi.org/10.1016/j.hedp.2021.100925.

Peer-reviewed journal publications related to AR role in the ETI:

- **Robert L. Masti**, C. Leland Ellison, William A. Farmer, Kurt Tummel, and Bhuvana Srinivasan. *The effect of anomalous resistivity on the fast electrothermal instability.* Physics of Plasmas, 2021.(post-review draft complete, and preparing for resubmission).

Peer-reviewed journal publications related to impact of AR in VCP on ETI:

- **Robert L. Masti**, William A. Farmer, and Bhuvana Srinivasan. *The impact of anomalous resistivity in vacuum contaminant plasmas on the electrothermal instability.* Journal of High Energy Density Physics, 2021.(draft complete preparing for submission).

Other peer-reviewed journal publications published during my Ph.D. studies:

- Jacob R. King, **Robert L. Masti**, Bhuvana Srinivasan, and Kris Beckwith. *Multi-dimensional Tests of a Finite-Volume Solver for MHD With a Real-Gas Equation of State.* IEEE Transactions on Plasma Science, 2020.https://doi.org/10.1109/TPS.2020.2981238.

- Bhuvana Srinivasan, Petr Cagas, **Robert Masti**, Chirag Rathod, Rajath Shetty, and Yang Song. *A survey of fluid and kinetic instabilities relevant to space and laboratory plasmas.* Radiation Effects and Defects in Solids, 2019.https://doi.org/10.1080/10420150.2019.1577853.

- Bhuvana Srinivasan, Petr Cagas, **Robert Masti**, Chirag Rathod, and Yang Song. *Fluid and kinetic simulations of plasma instabilities.* Radiation Effects and Defects in Solids, 2017.https://doi.org/10.1080/10420150.2017.1398247.

1.10 Attributions

Technical research is collaborative in nature and is reflected in the number of co-authored papers produced during my Ph.D. studies. The individual contributions of the co-authors to this research are as follows:

- *Dr. Bhuvana Srinivasan* is my Ph.D. advisor. She participated in big-picture planning, giving direction, discerning phenomena, and reviewed and edited my writing.
- *Dr. Jacob R. King* is a collaborator from Tech-X. He helped in debugging any unphysical numerical artifacts visualized in USim simulation results and guided in other tools such as python.
- *Dr. Peter H. Stoltz* is a collaboration from Tech-X. He helped in developing USim simulation prefiles.
- *Dr. C. Leland Ellison* is a collaborator formerly of Lawrence Livermore National Laboratory. He guided in the use of Ares, setting up simulations, providing understanding and references for AR, and participated in planning paths to publications.
- *Dr. William A. Farmer* is a collaborator from Lawrence Livermore National Laboratory. He provided continued support with Ares as well as guidance with all theoretical based questions, especially in linear theory.

Bibliography

[1] Kenneth S Krane, David Halliday, et al. *Introductory nuclear physics*. 1987.

[2] Francis F Chen and Schweickhard E von Goeler. Introduction to plasma physics and controlled fusion volume 1: Plasma physics. *Physics Today*, 38:87, 1985.

[3] R Paul Drake. Introduction to high-energy-density physics. In *High-Energy-Density Physics*, pages 1–20. Springer, 2018.

[4] David J Griffiths. Introduction to electrodynamics, 2005.

[5] DD Ryutov, MARK S Derzon, and M KEITH Matzen. The physics of fast z pinches. *Reviews of Modern Physics*, 72(1):167, 2000.

[6] DB Sinars, MA Sweeney, CS Alexander, DJ Ampleford, T Ao, JP Apruzese, C Aragon, DJ Armstrong, KN Austin, TJ Awe, et al. Review of pulsed power-driven high energy density physics research on z at sandia. *Physics of Plasmas*, 27(7):070501, 2020.

[7] MR Gomez, RM Gilgenbach, ME Cuneo, CA Jennings, RD McBride, EM Waisman, BT Hutsel, WA Stygar, DV Rose, and Yitzhak Maron. Experimental study of current loss and plasma formation in the z machine post-hole convolute. *Physical Review Accelerators and Beams*, 20(1):010401, 2017.

[8] DR Welch, N Bennett, TC Genoni, DV Rose, C Thoma, C Miller, and WA Stygar. Electrode contaminant plasma effects in 1.0e7-a z pinch accelerators. *Physical Review Accelerators and Beams*, 22(7):070401, 2019.

[9] S. A. Slutz et al. Pulsed-power-driven cylindrical liner implosions of laser preheated fuel magnetized with an axial fielda). *Physics of Plasmas*, 17(5):056303, 2010. doi: http://dx.doi.org/10.1063/1.3333505. URL http://scitation.aip.org/content/aip/journal/pop/17/5/10.1063/1.3333505.

[10] Hannes Alfvén. Existence of electromagnetic-hydrodynamic waves. *Nature*, 150(3805): 405–406, 1942.

[11] JR Davies, DH Barnak, R Betti, EM Campbell, P-Y Chang, AB Sefkow, KJ Peterson, DB Sinars, and MR Weis. Laser-driven magnetized liner inertial fusion. *Physics of Plasmas*, 24(6):062701, 2017.

[12] Adam B Sefkow, SA Slutz, JM Koning, MM Marinak, KJ Peterson, DB Sinars, and RA Vesey. Design of magnetized liner inertial fusion experiments using the z facility. *Physics of Plasmas*, 21(7):072711, 2014.

[13] SA Slutz, MR Gomez, SB Hansen, EC Harding, BT Hutsel, PF Knapp, DC Lamppa, TJ Awe, DJ Ampleford, DE Bliss, et al. Enhancing performance of magnetized liner inertial fusion at the z facility. *Physics of Plasmas*, 25(11):112706, 2018.

[14] D. B. Sinars et al. Measurements of magneto-rayleigh-taylor instability growth during the implosion of initially solid metal liners. *Physics of Plasmas*, 18(5):056301, 2011. doi: 10.1063/1.3560911. URL http://aip.scitation.org/doi/abs/10.1063/1.3560911.

[15] F García-Rubio, J Sanz, and R Betti. Magnetic flux conservation in an imploding plasma. *Physical Review E*, 97(1):011201, 2018.

[16] Subrahmanyan Chandrasekhar. *Hydrodynamic and hydromagnetic stability*. Courier Corporation, 2013.

[17] Bhuvana Srinivasan, Petr Cagas, Robert Masti, Chirag Rathod, and Yang Song. Fluid and kinetic simulations of plasma instabilities. *Radiation Effects and Defects in Solids*, 172(9-10):723–727, 2017.

[18] JR King, R Masti, B Srinivasan, and K Beckwith. Multidimensional tests of a finite-volume solver for mhd with a real-gas equation of state. *arXiv preprint arXiv:2001.11481*, 2020.

[19] Robert Masti, Bhuvana Srinivasan, Jacob King, Peter Stoltz, David Hansen, and Eric Held. Enhancing understanding of highenergy-density plasmas using fluid modeling with kinetic closures. In *2017 IEEE International Conference on Plasma Science (ICOPS)*, pages 1–1. IEEE, 2017.

[20] RL Masti, CL Ellison, JR King, PH Stoltz, and B Srinivasan. Cross-code verification and sensitivity analysis to effectively model the electrothermal instability. *High Energy Density Physics*, 38:100925, 2021.

[21] Vladimir Ivanovich Oreshkin. Thermal instability during an electrical wire explosion. *Physics of Plasmas*, 15(9):092103, 2008.

[22] K. J. Peterson et al. Electrothermal instability growth in magnetically driven pulsed power liners. *Physics of Plasmas*, 19(9):092701, 2012. doi: http://dx.doi.org/10.1063/1.4751868. URL http://scitation.aip.org/content/aip/journal/pop/19/9/10.1063/1.4751868.

[23] Kyle J Peterson, Edmund P Yu, Daniel B Sinars, Michael E Cuneo, Stephen A Slutz, Joseph M Koning, Michael M Marinak, Charles Nakhleh, and Mark C Herrmann. Simulations of electrothermal instability growth in solid aluminum rods. *Physics of Plasmas*, 20(5):056305, 2013.

[24] Kyle J. Peterson, Thomas J. Awe, Edmund P. Yu, Daniel B. Sinars, Ella S. Field, Michael E. Cuneo, Mark C. Herrmann, Mark Savage, Diana Schroen, Kurt Tomlinson, and Charles Nakhleh. Electrothermal instability mitigation by using thick dielectric coatings on magnetically imploded conductors. *Phys. Rev. Lett.*, 112:135002, Apr 2014. doi: 10.1103/PhysRevLett.112.135002. URL https://link.aps.org/doi/10.1103/PhysRevLett.112.135002.

[25] CE Seyler, Matthew R Martin, and ND Hamlin. Helical instability in maglif due to axial flux compression by low-density plasma. *Physics of Plasmas*, 25(6):062711, 2018.

[26] S. D. Crockett. Al-13. *LA-UR-04-6442*, Aug. 28. URL http://www.lanl.gov/org/padste/adtsc/theoretical/physics-chemistry-materials/_assets/docs/LAUR-92-3407.pdf.

[27] Charles W Cranfill. Eospac: A subroutine package for accessing the los alamos sesame eos data library. Technical report, Los Alamos National Lab., NM (USA), 1983.

[28] Travis Sjostrom, Scott Crockett, and Sven Rudin. Multiphase aluminum equations of state via density functional theory. *Physical Review B*, 94(14):144101, 2016.

[29] MP Desjarlais, JD Kress, and LA Collins. Electrical conductivity for warm, dense aluminum plasmas and liquids. *Physical Review E*, 66(2):025401, 2002.

[30] Randall J LeVeque. *Numerical methods for conservation laws*, volume 132. Springer, 1992.

[31] JD Pecover and JP Chittenden. Instability growth for magnetized liner inertial fusion seeded by electro-thermal, electro-choric, and material strength effects. *Physics of Plasmas*, 22(10):102701, 2015.

[32] T. J. Awe, K. J. Peterson, E. P. Yu, R. D. McBride, D. B. Sinars, M. R. Gomez, C. A. Jennings, M. R. Martin, S. E. Rosenthal, D. G. Schroen, A. B. Sefkow, S. A. , Slutz, K. Tomlinson, and R. A. Vesey. Experimental demonstration of the stabilizing effect of dielectric coatings on magnetically accelerated imploding metallic liners. *Phys. Rev. Lett.*, 116:065001, Feb 2016. doi: 10.1103/PhysRevLett.116.065001. URL https://link.aps.org/doi/10.1103/PhysRevLett.116.065001.

[33] Trevor M Hutchinson, Thomas James Awe, BS Bauer, KC Yates, Edmund P Yu, William G Yelton, and Stephan Fuelling. Experimental observation of the stratified electrothermal instability on aluminum with thickness greater than a skin depth. *Physical Review E*, 97(5):053208, 2018.

[34] Paulett C Liewer and NA Krall. Self-consistent approach to anomalous resistivity applied to theta pinch experiments. *The Physics of Fluids*, 16(11):1953–1963, 1973.

[35] K Tummel, CL Ellison, WA Farmer, JH Hammer, JB Parker, and KR Lechien. Kinetic simulations of anomalous resistivity in high-temperature current carrying plasmas. *Physics of Plasmas*, 27(9):092306, 2020.

[36] J Narkis, HU Rahman, P Ney, MP Desjarlais, FJ Wessel, F Conti, JC Valenzuela, and FN Beg. Shock formation in ne, ar, kr, and xe on deuterium gas puff implosions. *Physics of Plasmas*, 23(12):122706, 2016.

[37] J Narkis, HU Rahman, JC Valenzuela, F Conti, RD McBride, D Venosa, and FN Beg. A semi-analytic model of gas-puff liner-on-target magneto-inertial fusion. *Physics of Plasmas*, 26(3):032708, 2019.

[38] BB Kadomstev, AB Mikhailovskii, and AV Timofeev. Negative energy waves in dispersive media. *rn*, 2:4ne2n0, 1965.

[39] Sidney L Ossakow. Anomalous resistivity along lines of force in the magnetosphere. *Journal of Geophysical Research*, 73(19):6366–6369, 1968.

[40] AA Galeev and RZ Sagdeev. Theory of neoclassical diffusion. *RvPP*, 7:257, 1979.

[41] Vadim N Tsytovich. Nonlinear effects and plasma physics. In *Nonlinear Effects in Plasma*, pages 1–19. Springer, 1970.

[42] V Yu Bychenkov, Viktor Pavlovič Silin, and SA Uryupin. Ion-acoustic turbulence and anomalous transport. *Physics Reports*, 164(3):119–215, 1988.

[43] RC Davidson and NA Krall. Anomalous transport in high-temperature plasmas with applications to solenoidal fusion systems. *Nuclear Fusion*, 17(6):1313, 1977.

[44] K Papadopoulos. A review of anomalous resistivity for the ionosphere. *Reviews of Geophysics*, 15(1):113–127, 1977.

[45] JP Chittenden. The effect of lower hybrid instabilities on plasma confinement in fiber z pinches. *Physics of Plasmas*, 2(4):1242–1249, 1995.

[46] JD Huba. Anomalous transport in current sheets. In *Symposium-International Astronomical Union*, volume 107, pages 315–328. Cambridge University Press, 1985.

[47] Robert L. Masti, Charles L. Ellison, William A. Farmer, Kurt Tummel, and Bhuvana Srinivasan. The effect of anomalous resistivity on the fast electrothermal instability. *In review*, to be published in 2021.

Chapter 2

Cross-Code verification and sensitivity analysis to effectively model the electrothermal instability

Cross-Code verification and sensitivity analysis to effectively model the electrothermal instability

R. L. Masti[a,b], C. L. Ellison[b], J. R. King[c], P. H. Stoltz[c], B. Srinivasan[a,*]

[a] *Virginia Polytechnic Institute and State University, Blacksburg, VA 24060, USA*
[b] *Lawrence Livermore National Laboratory, Livermore, CA 94550, USA*
[c] *Tech-X Corporation, 5621 Arapahoe Ave., Boulder, CO 80303, USA*

Abstract

This manuscript presents verification cases that are developed to study the electrothermal instability (ETI). Specific verification cases are included to ensure that the unit physics components necessary to model the ETI are accurate, providing a path for fluid-based codes to effectively simulate ETI in the linear and nonlinear growth regimes. Two software frameworks with different algorithmic approaches are compared for accuracy in their ability to simulate diffusion of a magnetic field, linear growth of the ETI, and a fully nonlinear ETI evolution. The nonlinear ETI simulations show early time agreement, with some differences emerging, as noted in the wavenumber spectrum, late into the nonlinear development of ETI. A sensitivity study explores the role of equation-of-state (EOS), vacuum density, and vacuum resistivity. EOS and vacuum resistivity are found to be the most critical factors in the modeling of nonlinear ETI development.

Keywords: electrothermal instability, MagLIF, z-pinch, vacuum resistivity, equation-of-state sensitivity

1. Introduction

The current-driven electrothermal instability (ETI) forms when the material resistivity is dependent on temperature, occurring in nearly all Z-pinch-like high energy density (HED) platforms.[1] Previous work models the early time behavior of current-driven metallic explosions for pulsed wire array configurations as well as for imploding metal liner configurations such as in the magnetized liner inertial fusion (MagLIF) experiments.[2, 3] A number of codes have been used to simulate and understand the ETI, making it important to quantify how numerical modeling choices influence the evolution of the instability. [1, 2, 4, 5]

This work provides a series of verification cases in both linear and nonlinear regimes ensuring ETI-relevant unit physics is simulated accurately. Comparing these cases across codes highlights which differences between the codes are most important when simulating ETI such as time integration schemes for diffusion, spatial differencing methods, and numerical treatment of the highly resistive vacuum in which the ETI target resides. Additionally, this work performs cross-code comparisons for simulations of nonlinear ETI in regimes relevant to MagLIF and other pulsed-power driven HED platforms.

The two codes are USim, a commercially available multiphysics fluid code from Tech-X [6], and Ares, a Lawrence Livermore National Laboratory (LLNL) multiphysics radiation-hydrodynamics code.[7, 8, 9] USim is an unstructured-mesh-based Eulerian code while Ares is a structured-mesh-based arbitrary Lagrangian-Eulerian (ALE) code, and for this study, diffusion is temporally handled explicitly in USim and implicitly in Ares. Both codes solve the resistive magneto-hydrodynamics (MHD) equations with thermal conductivity. Obtaining similar results with such different algorithmic approaches provides confidence in the underlying discretization techniques and implementation in both codes.

This paper is structured as follows. Section 2 presents code descriptions for Ares and USim along with details on equation-of-state (EOS). Section 3 presents code verification that ensures the magnetic diffusion is captured accurately relative to an analytic solution and that the linear growth of ETI, in regimes of relevance to the Z-machine experiments [2, 4, 5], compares well with theory. Following code verification in the analytic and linear ETI regime, Section 4 presents comparisons of nonlinear ETI including a sensitivity study of nonlinear ETI dynamics to EOS treatment, vacuum resistivity, and vacuum density.

The key contributions of this paper are two-fold. First, analytic and theory-driven unit physics cases provide verification of the critical physics components necessary to accurately model ETI. Second, the nonlinear studies highlight the sensitivity of vacuum parameters and EOS in converged nonlinear ETI behavior. The sensitivity analysis shows nonlinear ETI behavior is influenced by vacuum resistivity more than vacuum density.

*Corresponding Author
Email addresses: rlm7819@vt.edu (R. L. Masti), srinbhu@vt.edu (B. Srinivasan)

2. Code Descriptions

For this study, the Ares and USim codes solve the magnetohydrodynamic equations which are given in conservative form as

$$\frac{\partial \rho}{\partial t} + \nabla \cdot [\rho \mathbf{u}] = 0, \tag{1}$$

$$\frac{\partial \rho \mathbf{u}}{\partial t} + \nabla \cdot \left[\rho \mathbf{u}\mathbf{u}^T - \frac{\mathbf{B}\mathbf{B}^T}{\mu_0} + \mathbb{I}\left(P + \frac{|\mathbf{B}|^2}{2\mu_0} \right) \right] = 0, \tag{2}$$

$$\frac{\partial \epsilon}{\partial t} + \nabla \cdot \left[\left(\epsilon + P + \frac{|\mathbf{B}|^2}{2\mu_0} \right) \mathbf{u} - \frac{1}{\mu_0} \mathbf{B} \cdot \mathbf{u}\mathbf{B} \right] = S_\epsilon, \tag{3}$$

and

$$\frac{\partial \mathbf{B}}{\partial t} = -\nabla \times S_{\mathbf{E}}, \tag{4}$$

where μ_0, ρ, $\mathbf{u}$, P, ϵ and $\mathbf{B}$, are the magnetic permeability of free space, mass density, 3D velocity, total pressure, total energy density, and magnetic field vector, respectively. S_ϵ and $S_{\mathbf{B}}$ represent the source terms for ohmic heating and thermal conduction in the former, and resistive magnetic diffusion in the latter.

The codes differ in multiple ways such as in their variable storage scheme (e.g. zone or node storage), mesh evolution, diffusion evaluation, and diffusion time integration. The different treatment of the diffusion terms, represented in S_ϵ and S_B in Equations 3 and 4, respectively, significantly influences ETI growth. For this work, S_ϵ is given by

$$S_\epsilon = \frac{-1}{\mu_0} \nabla \cdot \left(\frac{\eta}{\mu_0} \nabla \times \mathbf{B} \right), \tag{5}$$

where η is the electrical resistivity, and the contribution to the $S_{\mathbf{B}}$ in Equation 4 is given by

$$S_{\mathbf{B}} = -\nabla \times \left(\frac{\eta}{\mu_0} \nabla \times \mathbf{B} \right). \tag{6}$$

For this study, differences exist algorithmically in the temporal integration and spatial differentiation of these terms. Section 4 explores these differences leading to substantially different computational challenges and numerical limitations.

2.1. USim Code

USim uses finite-volume algorithms on an unstructued Eulerian grid to solve conservative equation systems. In the simulations presented here, USim uses the Monotone Upwinding Scheme for Conservation Laws (MUSCL) to perform cell interface reconstruction for the computation of the Eulerian fluxes.[10] For these fluxes, USim utilizes the Harten-Lax-van Leer-Discontinuities (HLLD) approximate Riemann solver given by Miyoshi and Kusano [11] (5-wave) modified to incorporate the changes to the waves introduced by the real-gas EOS.[12] Additionally, USim utilizes hyperbolic divergence cleaning as given by Dedner et al. [13]. For hyperbolic temporal integration, USim uses a 2^{nd} order Runge-Kutta time integration scheme with variable time step.

For this study, USim uses super-time-stepping (STS) to handle the parabolic terms embedded in S_ϵ and $S_{\mathbf{B}}$. STS modifies the number of Runge-Kutta stages for the parabolic terms so they can be evolved at the hyperbolic time step. [14] The number of stages is proportional to the ratio of the hyperbolic time step to the diffusion time step, which can be many orders of magnitude for the nonlinear ETI simulations in Section 4, albeit there are limits to the number of stages before STS begins to impact accuracy.[14] Although USim's STS is capable of 2^{nd} order accuracy, only the first-order accurate implementation is used for direct comparisons between codes. Section 3.1 tests the magnetic diffusion contribution to S_ϵ in Equation 3 which is given by Equation 5, and contribution to $S_{\mathbf{B}}$ in Equation 4 which is given by Equation 6.

USim implements the divergence and curl operators through a polynomial fit approximation as this algorithm is suitable for problems with a general unstructured mesh. With this method a field variable, such as B_x, is fitted with a multi-dimensional polynomial and the value of the derivative is computed to obtain the differentiated quantity; e.g. the current density.[15] Discontinuities in field variables can cause oscillations in the fitting procedure of the least-squares method. Circumventing these oscillations requires using a large stencil which reduces or smooths out the magnitude of the derivatives at the discontinuity.[1] As an example, $S_{\mathbf{B}}$ from Equation 6, experiences large gradients due to the discontinuous resistivity at the vacuum-liner interface during the nonlinear ETI simulations, and a small stencil would over represent the gradient magnitude at this interface. While USim typically uses a 2nd order derivative reconstruction, the large gradients in the diffusive quantities in Eq. 6 require a first order reconstruction due to numerical instability with the higher order polynomial fits.

Nonlinear ETI simulations in Section 4 include thermal diffusion in addition to magnetic diffusion augmenting the S_ϵ term. USim evolves the total energy density given in Equation 3, so an inverse EOS operation is performed at every time step to get the temperature from the internal energy density. For this study, USim applies thermal diffusion through a source term given as

$$\frac{\partial T}{\partial t} = \nabla \cdot (\alpha \nabla T), \tag{7}$$

where α is the thermal diffusivity. This equation requires the use of an additional EOS operation to compute internal energy density (ϵ_{int}) updating the total energy density (ϵ) from Equation 3 through the relation $\epsilon = \epsilon_{int} + 1/2\rho\mathbf{u}^2 + 1/(2\mu_0)\mathbf{B}^2$. For the nonlinear ETI simulations in Section 4, both codes use thermal conduction,

[1] A stencil of 20 was found to be sufficient in evaluating diffusive fluxes

as it improves numerical stability and is physically relevant in the linear ETI growth phase of the simulation.[1, 2]

USim handles the multi-material setup of the nonlinear ETI simulation (liner-vacuum) through the use of a marker which is a unit-less identifier (-1 to 1). This marker is evolved with the normalized advective fluxes of Equation 1 which follows the movement of each material respectively. Due to the density voids created in the nonlinear ETI growth and the lack of vacuum energy conservation (see Section 4 and Figure 8), this marker is filtered such that a zone containing liner material above the interface cannot transition to a vacuum zone (marker is always > 0 above interface). This implementation does not allow for ejection of liner material into the vacuum, but it does allow for seldom transition from liner material to vacuum along the continuous interface through the marker going from > 0 to < 0.

2.2. Ares Code

Ares is one of LLNL's multiphysics radiation hydrodynamics codes specializing in inertial confinement fusion (ICF), high energy density (HED) physics, and energetic materials [9, 7, 8]. At its core, Ares solves single-fluid multi-material multi-component[2] Euler or Navier-Stokes hydrodynamic equations on a structured, arbitrary Lagrangian-Eulerian (ALE), adaptive mesh refinement (AMR) grid. Depending on the application, additional physics packages are incorporated in an operator split fashion. Major physics packages include resistive and extended magnetohydrodynamics, laser ray tracing and energy deposition, single- or multi-group radiation diffusion, S_n radiation transport, Reynolds-Averaged Navier-Stokes (RANS) turbulence models, and thermonuclear burn.

For this work, all of the Ares simulations use the 2D resistive MHD package without AMR. The 2D MHD package assumes that currents reside in the $x - y$ or $r - z$ simulation plane, while a single component of the magnetic field evolves perpendicular to the simulation plane. During the Lagrange step, the zone-centered magnetic field is frozen into the fluid. After the Lagrange step, the mesh can optionally be relaxed towards it's initial position according to the user's ALE prescription. All mesh variables are then interpolated from the post-Lagrange mesh to the relaxed mesh using conservative, finite-volume, total variation diminishing flux-limited advection schemes. In the case of the magnetic field, the finite volume advection preserves magnetic fluxes. Note that for the purposes of this work, Ares was run in full relaxation "Eulerian mode", which compares nicely to USim's Eulerian formulation.

[2]I.e., Ares evolves a single fluid velocity but multiple material densities and temperatures within any multi-material zones, and each material allows multiple components (equations of state) that are required to be in pressure and temperature equilibrium with other components of the same material in the zone.

Resistive diffusion of the magnetic field and the hydrodynamics motion are treated separately using operator splitting methods. Both the magnetic diffusion equation and the thermal diffusion are advanced implicitly in time using a first-order accurate backward-Euler method. Similarly, both diffusion operations employ a second-order accurate finite volume spatial discretization.[16] This method is akin to a bilinear finite element discretization.

Ohmic heating is applied explicitly in time after the implicit magnetic diffusion update. The updated magnetic field is differenced to calculate edge-centered currents according to Ampere's Law. The ohmic heating incurred by the edge-centered currents is partitioned into the two adjacent zones by treating the two zones as resistors in parallel.

Ares handles multi-material dynamics with a volume-of-fluid approach. This approach assigns a volume fraction to each material present within a given zone. In addition to the sub-zonal volume, each material is allowed its own sub-zonal thermodynamic state including density, temperature, and pressure. However, only a single (node-centered) fluid velocity is maintained (thus the single-fluid multi-material designation for the code). For MHD, a zone-averaged conductivity is required for magnetic diffusion and ohmic heating. For this study, Ares uses a mass-fraction-weighted average of the conductivities for zones that contain multiple materials.

2.3. Equation of State

Since ETI growth depends on the resistivity of a material, and the resistivity is a function of the material's state, an accurate EOS is important. HED simulations of experiments often rely on tabular EOS libraries to provide accurate representations of the material state across a wide range of densities and temperatures. These EOS tables provide the P and the ϵ as functions of density and temperature, including into HED regimes. In previous work[2, 4], the SESAME EOS database was used to model ETI specifically using SESAME 3720 (SES3720) [17] for an aluminum EOS, and Sandia Lee-More based Desjarlais (QLMD) tables for aluminum transport properties.[18]

The nonlinear ETI simulations in Section 4 employ an analytic Birch-Murnaghan EOS (BMEOS) for ease of code-code comparisons. The magnetic diffusion and linear ETI simulations in Section 3 employ an ideal gas EOS. Sensitivity studies in Section 4.2 assess how the nonlinear ETI behavior differs between BMEOS and SES3720 EOS. For this study, the QLMD effective ionization table is used in conjunction with the BMEOS to span a large state space. BMEOS is an analytic equation of state determined through data regression, and this work uses the functional form used by McBride and Slutz [19] where the

pressure and internal energy are given by [20, 21, 22, 19]

$$P = P_0 + \frac{3}{2}A_1\left[\left(\frac{\rho}{\rho_0}\right)^{g_1} - \left(\frac{\rho}{\rho_0}\right)^{g_2}\right]\left[1 + \frac{3}{4}(A_2 - 4)\left[\left(\frac{\rho}{\rho_0}\right)^{g} - 1\right]\right], \tag{8}$$

where for aluminum $P_0 = (1 + Z_{\text{eff}})k_B\rho T/m$, $m = 4.509 \times 10^{-26}\,\text{kg}$, $A_1 = 76 \times 10^9\,\text{Pa}$, $\rho_0 = 2700\,\text{kg m}^{-3}$, $g_1 = 7/3$, $g_2 = 5/3$, $A_2 = 3.9$, and $g = 2/3$ with Z_{eff}, k_B, ρ, T, representing the effective ionization level, Boltzmann constant, density [kg m^{-3}], and temperature [K], respectively.[19] Similarly, the specific internal energy density is given by

$$\epsilon = \epsilon_0 + \frac{9}{16}A_1\rho_0^{-1}\left[A_2\left[\left(\frac{\rho}{\rho_0}\right)^{g} - 1\right]^3 + \left[\left(\frac{\rho}{\rho_0}\right)^{g} - 1\right]^2\left[6 - 4\left(\frac{\rho}{\rho_0}\right)^{g}\right]\right], \tag{9}$$

where $\epsilon_0 = 3/2(1 + Z_{\text{eff}})k_BT/m$. BMEOS has a max difference to SES3720 of 40%; see Appendix A

Implementing tabulated EOS or tabulated transport coefficients requires a choice of interpolation algorithm such as bilinear or bicubic. Section 4.2 shows the effect of interpolation algorithm and EOS on the Ares nonlinear ETI simulation. For this study, Ares uses LLNL's LEOS [23, 24, 25] algorithms for table interpolation, and USim uses Los Alamos's EOSPAC interpolation library. [26]

3. Cross Code Verification

This work provides a guide to running nonlinear ETI simulations by sequentially verifying the individual physics components relevant to ETI. The first verification test is of magnetic diffusion where solutions from the two codes are compared against an analytical result. The second verfication test is a linear ETI simulation with negligible magnetic diffusion relative to the ohmic heating in S_ϵ of Equation 3, isolating the ohmic heating and resistive feedback mechanisms.

3.1. Magnetic Diffusion

This test case involves an x-directed magnetic field varying sinusoidally along the y direction resistively diffusing due to a constant resistivity in space and time. This test uses Cartesian coordinates with the fluid initially at rest. The magnetic field diffuses towards the steady state solution of a constant field. Comparing this time evolution to the analytically-derived solution quantifies the numerical error.

The diffusion equation in Equations 4 and 6 with constant resistivity reduces the curl operations to a simple Laplacian diffusion equation in Cartesian coordinates. In order to isolate magnetic diffusion from the full MHD equation, the initial conditions and strength of electrical resistivity must satisfy certain conditions. These conditions are that any thermal pressure due to ohmic heating be negligble relative to the magnetic pressure, and that any motion due to the magnetic pressure occurs at much longer time-scales than the magnetic diffusion time-scale. Using a plasma beta, the ratio of thermal pressure to magnetic pressure, of unity satisfies the first condition, and a Lundquist number of unity satisfies the second condition. Although only the magnetic field is needed to analyze Equation 6, the codes evolve the full MHD equations; hence, a low plasma beta and a low Lundquist number are chosen to study the isolated effect of magnetic diffusion in Equations 4 and 6.

The chosen simulation grid uses an x domain of 0.25 m and an y domain of 1 m with a resolution of 50x200 grid cells, respectively. The uniform initial state is P_0 =1.0133 $\times 10^5$ Pa and ρ_0 =0.164 kg m^{-3} with an ideal gas equation of state (EOS) using $\gamma = \frac{5}{3}$.[3] The initial magnetic field is $\mathbf{B_0} = \langle 0.5044\cos(2\pi y), 0, 0\rangle$ T, and the initial electrical resistivity is η =1.396 $\times 10^{-3}\,\Omega\,\text{m}$. Given these parameters, the characteristic magnetic diffusion rate is

$$\gamma_{md} = \frac{4\pi^2}{L_yL_u}\sqrt{\frac{2P_0}{\beta\rho}} \approx 4.387 \times 10^4\,\text{s}^{-1}, \tag{10}$$

and the chosen simulation end time is t_f =45.59 µs $(2/\gamma)$.

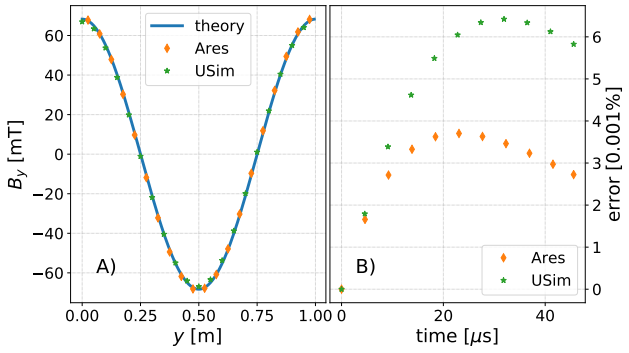

Figure 1: Plot A on the left shows the x-direction magnetic field in [mT] along the vertical direction at the magnetic diffusion simulation end time of 45.59 µs over a subset of the simulation range. Plot B on the right shows the L_2 norm of the error between the simulated magnetic field and the analytically-derived magnetic field over time.

Figure 1 presents the error of both codes as a function of time, and an instantaneous lineout of each simulation along with the analytically-derived solution. This configuration results in a maximum global error of less than 0.01% for both the Ares and USim simulations. This low error provides confidence in the magnetic diffusion capabilities of both codes, and is critical for resolving the nonlinear ETI magnetic diffusion wave.

[3] The choice of initial state or EOS has no impact on this test

3.2. Linear ETI

ETI occurs whenever ohmic heating is applied to a material with a temperature-dependent resistivity. The combination of the changing resistivity and ohmic heating creates a positive feedback loop causing hot spots to develop internally. The linear ETI growth rate is given by[27, 2]

$$\gamma = \frac{\eta_T J_z^2 \left(1 - \frac{2\cos^2\alpha}{1+\gamma/\gamma_0}\right) - k^2\kappa}{\rho\epsilon_T}, \tag{11}$$

where $\gamma_0 = 2k\eta/\mu_0\Delta r$. $\mathbf{k}$, κ, η, T, ϵ_T, and α, are the wavevector, the thermal conductivity, the resistivity, the temperature, the partial derivative of the specific internal energy ($\mathrm{J\,kg^{-1}}$) with respect to temperature, and the angle between the wavevector and magnetic field, respectively. For $\eta_T \equiv \frac{\partial\eta}{\partial T} > 0$ (most commonly the case for metals at solid densities and low temperatures), the maximum growth occurs when $\alpha = 90°$, resulting in a growth rate of

$$\gamma = \frac{\eta_T J_z^2 - k_z^2\kappa}{\rho\epsilon_T}\,. \tag{12}$$

While the magnetic diffusion test verifies the effect of the electrical resistivity on the magnetic field evolution, this linear ETI test verifies the effect of the electrical resistivity on the internal energy density evolution. Figure 2 shows the problem setup. In the absence of thermal conductivity, the growth rate becomes

$$\gamma = \frac{\eta_T J_z^2}{\rho\epsilon_T}. \tag{13}$$

This form of the theoretical growth rate depends heavily on ohmic heating, so reproducing this analytical result through simulation provides confidence in each code's ability to capture ohmic heating and the feedback of such heating on the evolution of the material state. For this simulation, the initial parameters (relevant current, length, and time scales) are set to reproduce ohmic heating in a typical pulsed power regime. This test uses aluminum as the conducting material following the state parameters and conductivities derived from the SES3720 and QLMD 29373 tables, respectively.[17, 18].

This test uses initial parameters of $\rho_0 = 2700\,\mathrm{kg\,m^{-3}}$, $T_0 = 250\,\mathrm{K}$, $I_0 = 10\,\mathrm{MA}$, over an annulus with a thickness of $500\,\mu\mathrm{m}$ starting at a radial location of 2.68 mm. Uniformally distributing the current in the annulus results in a current density of $J_z = 1.09 \times 10^{12}\,\mathrm{A^2\,m^{-1}}$, and is similar to the values from Figure 4 of Peterson et al. [4] ($1 \times 10^{12}\,\mathrm{A^2\,m^{-1}}$ to $7 \times 10^{12}\,\mathrm{A^2\,m^{-1}}$). From the growth rate defined in Equation 13, the η_T and the ϵ_T for this simulation use values consistent with realistic solid metallic parameters relevant to pulsed power HED regimes.

Figure 3 shows the conductivity for aluminum at solid density over the entire range of the QLMD table in panel A) and a linear fit to a small range of temperatures in panel B).[18] The fit from plot B yields an $\eta_T = 1.099 \times 10^{-8}\,\mathrm{s\,K^{-1}}$ (in mks: $\eta_T = 1.099 \times 10^{-10}\,\Omega\,\mathrm{m\,K^{-1}}$). This η_T is valid for constant density solid aluminum between 200 K to 900 K; note that the electrical resistivity is more sensitive to the density than the temperature in this state space region. [2]

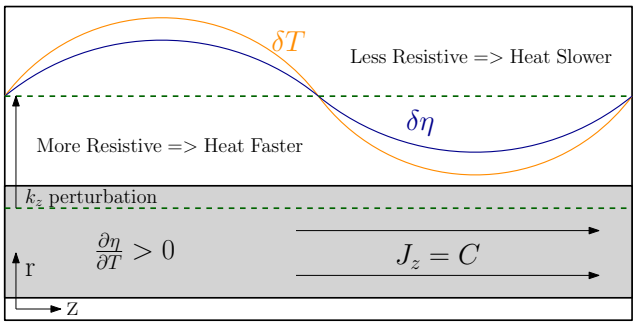

Figure 2: Schematic depicting the linear ETI test in cylindrical coordinates wherein a spatially varying resistivity exists inside a uniformly distributed current. The perturbed temperature (or the internal energy density) perturbs resistivity, and provided the resistivity increases with temperature, this configuration is ETI unstable as implied by Equation 12.

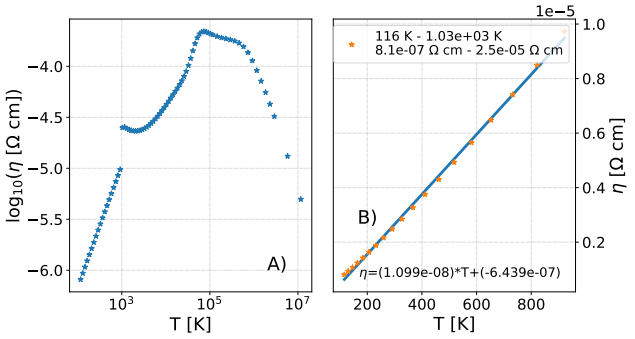

Figure 3: Plot A on the left shows a constant density contour of the logged QLMD conductivity table for aluminum for a certain temperature range.[18] Plot B on the right shows a subset of Plot A in the low temperature regime, where the resistivity linearly increases with temperature. The fitted linear region in plot B yields an estimate for η_T.

The specific heat capacity, ϵ_T, is approximately $822\,\mathrm{J\,kg^{-1}\,K^{-1}}$ based on SES3720 at the initial state. This test uses an ideal gas EOS with the adiabatic index, γ, chosen to maintain a constant ϵ_T. Knowing ϵ_T, the adiabatic index is $\gamma = 1 + [k_B/(m\epsilon_T)]$ where k_B is the Boltzmann constant and m is the atomic weight, resulting in an adiabatic index of $\gamma \approx 1.373$.

The simulation radial domain is from 2.54 mm to 3.16 mm with the inner annulus radius set to 2.66 mm, and the simulation axial domain is ± 0.25 mm and is arbitrary based on Equation 13 (absent k_z dependence). The resolution varies in the radial direction from 38 to 300 cells and in the axial direction from 25 to 200 using a factor of two refinement levels to produce the convergence plot in

Figure 4.

With these parameters, the ETI growth rate from Equation 12 is $\gamma \approx 5.891 \times 10^7\,\mathrm{s}^{-1}$. The end time for this simulation is three growth periods corresponding to $3/\gamma \approx 57.5\,\mathrm{ns}$. The error between the simulated linear ETI growth[4] and the theoretical growth rate produces Figure 4 using different spatial resolutions and time steps.

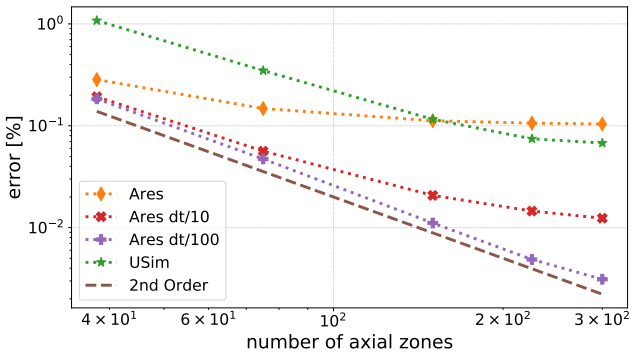

Figure 4: Plot of percent error, relative to the theoretical growth rate, of the linear ETI simulation in Section 3.2 for different radial and axial resolutions. The Ares convergence exhibits second-order spatial convergence (error $\propto \Delta z^{-2}$=zone size^{-2}) provided the time discretization errors are small (USim was not tested in this limit), and both codes asymptote to similar percent error when using similar time steps .

The rate (order) of convergence describes how the error (difference between exact solution and numerical approximation) decreases for increasing spatial or temporal resolution. Figure 4 presents convergence results of USim and Ares for the linear ETI simulation. For the largest time step, Ares asymptotes to 0.1 percent error and USim approaches first-order spatial convergence. This difference is due to Ares using a fixed time step and USim using an adaptive time step. The error depicted in Figure 4 has contributions from both the spatial discretization and temporal discretization. The temporal discretization error, at sufficiently small time step size, becomes small relative to spatial discretization error thereby recovering the Ares spatial order-of-accuracy of second order for uniform meshes. Comparing the asymptotic errors exhibited by Ares in the high resolution limit, there is reasonable agreement with the anticipated first-order accuracy in time outlined in Section 2. Additionally, while Ares uses a fixed maximum time step for this simulation, USim has an adaptively changing time step that decreases slightly as the solution evolves, which likely contributes to the lower asymptotic error.

In summary, both codes accurately capture the theoretical growth rate to within 0.1% in the asymptotic limit given the maximum stable time step. Figure 4 shows the Ares spatial order-of-accuracy is second order, and the temporal order-of-accuracy is approximately first order. This case shows excellent agreement between the linear ETI growth rate from Equation 12 and the simulated linear ETI growth across both codes.

[4]Obtained by fitting an exponential growth of the temperatue deviation from the mean (maximum - minimum)

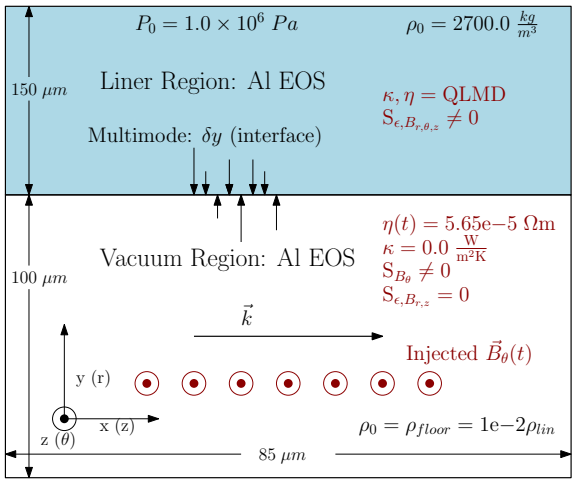

Figure 5: The simulation setup for the nonlinear ETI discussed in Section 4, showing the different regions, densities, source terms, and conductivities.

4. Nonlinear ETI

The nonlinear ETI case explores, in planar coordinates, the effect of resolving the magnetic diffusion wave through a medium (aluminum). The subsequent current redistribution, and the spatially non-uniform ohmic heating leads to nonlinear growth of ETI. This nonlinear ETI case builds upon the verfied magnetic diffusion from Section 3.1 and the verified ohmic heating from Section 3.2 to run a physically-relevant ETI simulation for solid cylindrical and wire explosion regimes.[1, 2, 4] This specific case, as shown in Figure 5, is based on the simulation work done by Peterson et al. [4].

4.1. Baseline Nonlinear ETI

For the current source in these simulations, Ares allows the user to directly specify the current as a function of time whereas USim requires specifying the value of the magnetic field at the boundary. Within the code, Ares uses Ampere's law to specify the magnetic field at the boundary, and given the same coordinate system, this is the same as directly specifying the magnetic field at the boundary as done in USim. Limitations in the accuracy of USim's curl operator in cylindrical coordinates lead to using planar geometry in both codes for these simulations. Although the simulations are in planar geometry, the specified magnetic field boundary condition is consistent with the cylindrical geometry.

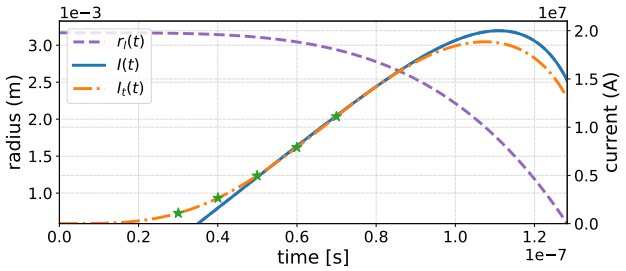

Figure 6: Liner outer radius $r_l(t)$, normal current $I(t)$, and adjusted current $I_t(t)$ as a function of time with the adjusted current profile providing inclusion of the prepulse phase typical of a Z-machine shot.

From Slutz et al. [3], closed-form expressions for liner radius and current are empirically-derived from pulsed-power experiments conducted on the Z machine. The purple dashed curve in Figure 6 represents the outer liner radius, r_l, as a function of time given by

$$r_l(t) = r_{l_0}\left(1 - \left(\frac{t}{t_p}\right)^4\right), \tag{14}$$

where r_{l_0} is the initial outer liner radius (2.92 mm to 3.168 mm) and t_p is the pulse time (≈135 ns). [3, 28, 2] Current, I, as a function of time is given by

$$I(t) = I_x\left(\frac{27}{4}\right)^{\frac{1}{4}}\sqrt{\left(\frac{t}{t_p}\right)^2 - \left(\frac{t}{t_p}\right)^6}, \tag{15}$$

where I_x is the peak current (20 MA to 27 MA).

Most high power, pulsed-power machines, such as Z, have a prepulse phase before the full pulse is delivered. On the Z machine, this prepulse lasts anywhere from 40 ns to 80 ns as evident from experimentally-measured load data.[3, 28, 2] Equation 15 does not have slowly rising pre-pulse behavior, which would cause premature ablation disrupting the perturbation of the liner-vacuum interface. To incorporate this experimentally-observed initial rise, the functional form of the current drive in Equation 15 is modified to obtain I_t. Figure 6 depicts the original current I and the modified current I_t. The adjusted form of the current is

$$I_t(t) = I(t)\left(1 - \exp\left[-\left(\frac{t}{t_r}\right)^2\right]\right)^{1.25}, \tag{16}$$

where $I(t)$ is given by Equation 15 and t_r is the adjustable pre-pulse time of 60 ns. Note that although the simulations shown in this section are early in time, this current form is usable to accurately approximate late time phenomena in Z-like pulses. Though the peak current of the adjusted form is noticeably smaller than the peak of the original form, it is closer to the experimentally-measured peak current from Figure 11b of Peterson et al. [2].

To convert this current drive to a planar magnetic boundary condition for USim, Ampere's law is used in cylindrical coordinates to determine the magnetic field at the time-varying radial location of the liner interface. For Ares, the current is set as

$$I_{\text{Ares}}(t) = \frac{I_t(t)}{2\pi r_l(t)},$$

so that the magnetic field in both planar problems is the same and representative of the magnetic field experienced by the liner on Z.

Ares solves parabolic equations implicitly, contrarily, USim solves parabolic equations semi-explicitly (as discussed in Section 2). With an implicit sover, Ares can handle large vacuum resistivity values without excessive computational cost. Because USim uses the semi-explicit STS scheme, it is not computationally practical to run with the same large vacuum resistivity as this leads to an impractically large number of STS stages making the computational cost significantly more expensive. Thus, a much lower vacuum resistivity needs to be specified with certain constraints. First, if the resistivity of the vacuum is relatively low, this results in unphysical currents in the vacuum, diverting the current away from the liner region. These currents cause unphysical ohmic heating in the vacuum resulting in a highly restrictive time-step. Hence, the vacuum resistivity is set to a large value, and ohmic heating is neglected in the vacuum.[5] Further numerical challenges include the creation of density voids during ETI development due to a finite diffusion rate of the magnetic field through the vacuum. This finite diffusion rate leads to waves in the vacuum creating low density regions where large magnetosonic speeds further restrict the time-step. Avoiding this requires a large enough vacuum resistivity such that the vacuum magnetic diffusion transit time is small relative to the hyperbolic time-step.

Figure 5 presents the simulation setup consisting of an x domain of 85 µm and y domain of 250 µm with a resolution of 256x640 cells, respectively. The multimode perturbation of the interface is of the form

$$\delta = \frac{1}{32}\sum_{m=1}^{m=32}\beta_m \cos\left[2\pi\left(\frac{m\cdot x}{\lambda_{max}} + \beta_m\right)\right], \tag{17}$$

where β is a random number from 0 to 1, $\lambda_{max} = 200\ \mu m$ is the maximum wavelength associated with the lowest mode (see Appendix B for the coefficients used). Figure 5 shows the initial state. This setup uses a pressure equilibrium to avoid bulk motion of the liner, as material strength models are not employed. Note the EOS interpolation algorithm is the birational LEOS interpolation scheme for Ares[23, 24, 25] and the birational EOSPAC interpolation scheme for USim[26]. For thermal and electrical conductivities of the liner, the QLMD table 29373 for aluminum is used, and

[5] This violates energy conservation (at least in the vacuum), but is necessary for an accurate current rise in the liner given a finite resistive vacuum when using an explicit or semi-explicit scheme.

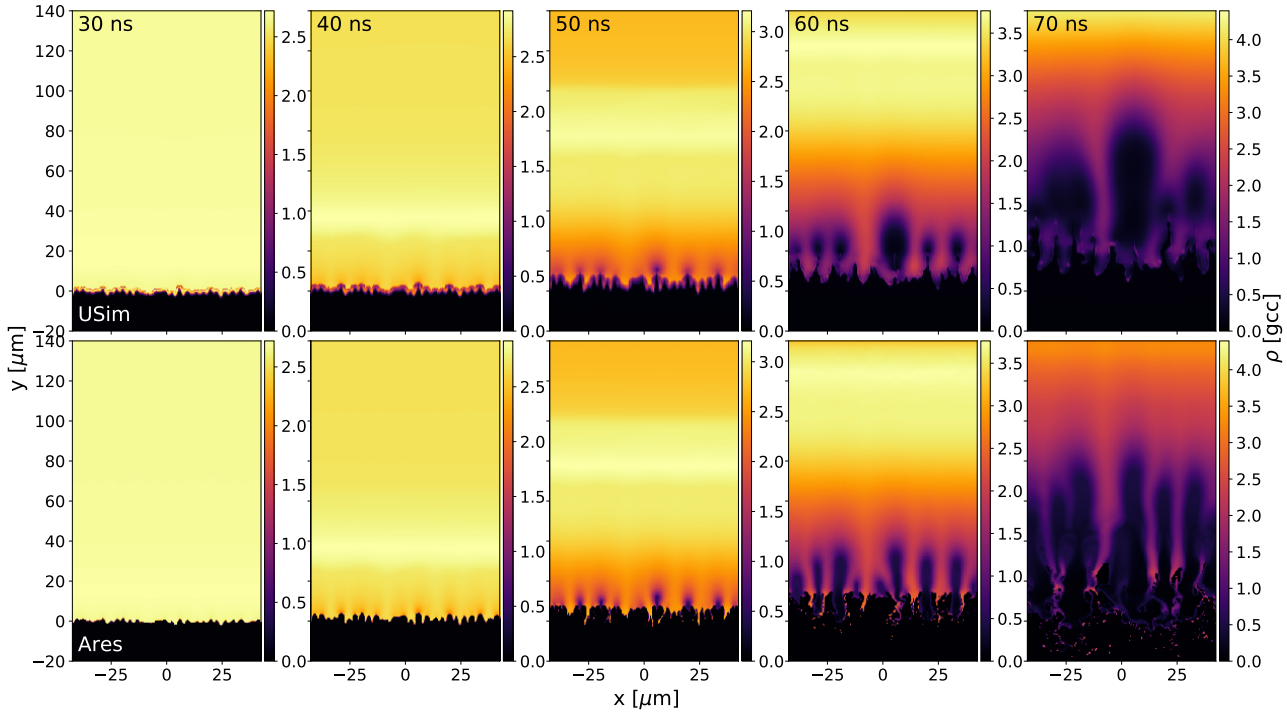

Figure 7: Density plots of the nonlinear ETI simulation outlined in Section 4 at different times (correspond to Figure 6) with the top row showing the USim results, and the bottom row showing the Ares results. The current at these times is indicated by the green markers in Figure 6

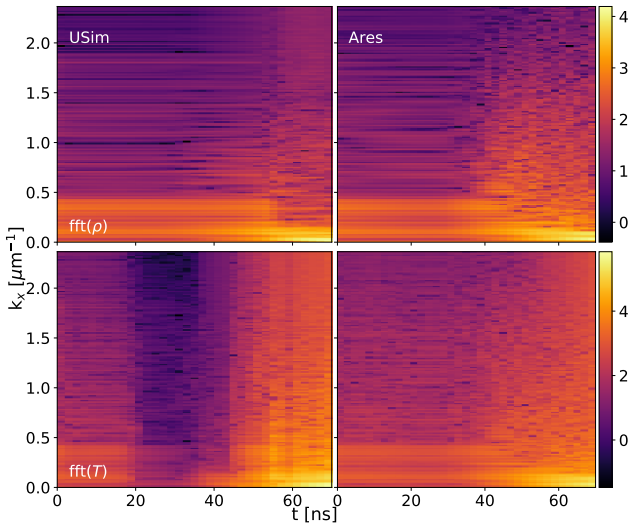

Figure 8: The fast Fourier Transform of y-averaged values, of density (top) and temperature (bottom), over a range of −100 µm to 145 µm along the x-direction are presented. Plots shown are different snapshots in time from 0 ns to 70 ns of the nonlinear ETI simulation outlined in Section 4. The colorbar corresponds to spectral energy, the x-axis corresponds to time, and the y-axis corresponds to the wave number along the x-direction.

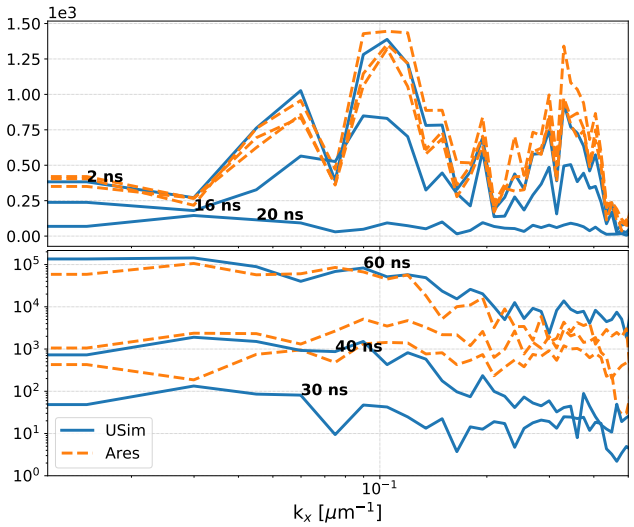

Figure 9: Vertical lineouts of the temperature FFTs is shown in the bottom row of Figure 8 at various times for both the Ares and USim results. Note that the differences between the codes are more pronounced early-in-time (top plot) whereas the solutions agree more closely late-in-time (bottom plot).

the EOS for the vacuum and liner is BMEOS, as discussed in Section 2.3.[18]

Figure 7 shows snapshots in time of the simulation results for USim (top) and Ares (bottom). Both codes show a similar magnetic diffusion wave and a density spike that is propagating inward in the 40 ns, 50 ns, and 60 ns snapshots at $y \approx 38$ µm, $y \approx 79$ µm, and $y \approx 122$ µm, respectively.[6]. While the USim results do not allow ablation into the vacuum, resulting in no mixing of material regions, the Ares results do show ablation into the vacuum, as its multimaterial treatment handles mixing of material regions. This ablation/finger development, seen in the Ares results and slightly in the USim results, is the beginning of the subsequent electro-choric instability (ECI) as discussed by Pecover and Chittenden [29]. Due to the difference in multimaterial treatment between the codes [7] this is not explored further, but note the time for when ECI begins to form (60 ns) matches the observations from the Pecover and Chittenden [29] simulations.

Earlier in time, the interface in the USim simulation is diffuse, showing a smoother density gradient relative to the Ares result at 30 ns and 40 ns. At 70 ns, the Ares result shows smaller wavelength growth with a sharper density gradient at the spike interface even though the spikes penetrate to a similar distance (≈ 40 µm). At 60 ns, both codes show similar wavelength modes of ETI, whereas at 70 ns, Ares retains more shorter-wavelength modes compared to USim.

Figure 8 presents a discrete fast Fourier transform of density and temperature along the x-direction, and highlights how the mode structures change over time. Figure 8 also shows the early time (30 ns, 40 ns, and 50 ns) suppression of the perturbation in the USim results due to numerical diffusion at the interface. Diffusion is more pronounced in the FFT of temperature (bottom left plot) in Figure 8. Both codes converge later in time to lower mode (lower k) growth, as is observed qualitatively in Figure 7 and quantitatively in Figure 8.

Figure 9 shows FFT of the temperature at several different times corresponding to the decrease and increase in amplitude shown for the USim results in the bottom left plot of Figure 8. By doing so, Figure 9 highlights the USim result diverging from the Ares result early in time while approaching the Ares result later in time. This suppression and growth of the perturbation in USim could be due to USim's handling of the source terms in the vacuum. This could also be due to the diffusion stencil at the interface reducing mode amplitude early in time, and increases in temperature variation caused by signifcant ohmic heating raising mode amplitude late in time.

4.2. EOS Sensitivity

A sensitivity analysis performed with Ares shows how different choices of EOS and interpolation scheme impact the development of ETI in the nonlinear regime. From Equation 12, the growth rate of ETI is dependent on ϵ_T (specific heat capacity), and this value is deduced from the

[6]Figures 7 uses a subsection of the simulation result and is why the peak is not seen explicitly in the 70 ns plot

[7]USim currently does not have vapourisation capabilities

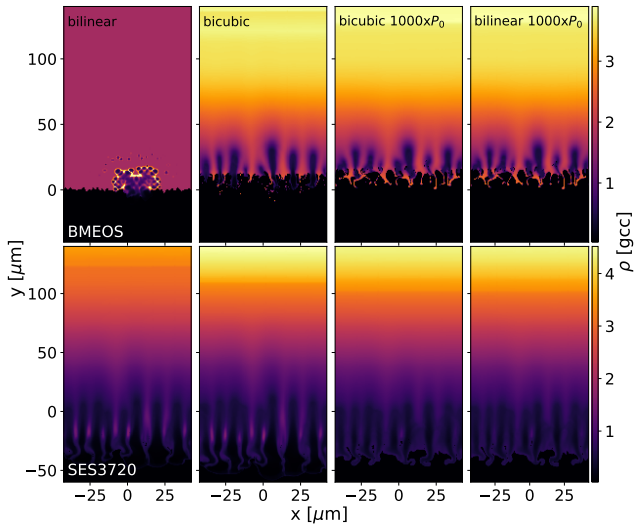

Figure 10: Density evolution of the nonlinear ETI simulations is presented at 60 ns using different EOS interpolation schemes (bilinear and bicubic) and different EOS (BMEOS and SES3720).[17]

representative EOS. Choices of table interpolation, inversion, and monotonicity, will influence the nonlinear ETI behavior directly through ϵ_T (indirectly through η_T).

Figure 10 shows the effect of using different EOS on the ETI mode growth in the Ares simulations with the BMEOS (top) and the SES3720 EOS (bottom). Using bilinear interpolation at low pressure and high density results in the crash of both the BMEOS and the SES3720 simulations as noted in the leftmost subplots (top for BMEOS and bottom for SES3720) of Figure 10. This crash is from the evaluation of the sound speed, obtained from derivatives of the pressure with respect to density and temperature, encountering imaginary values (imaginary time-step) for both EOS simulations. The qualitative differences between the bilinear interpolation BMEOS and SES3720 cases before the simulations crash (leftmost plots) are likely due to the resolution of the table at the high-density, low-temperature regime and/or the magnitude of the sound speed evaluated in this region. Using bicubic interpolation produces the same result as more high fidelity interpolation schemes such as birational, bihermite, bimonotonic, and biquintic, not shown here.

The bilinear interpolation becomes suitable in the high-pressure, high-density regime, as this is a better-defined region of the table.[8] The two right-most columns of Figure 10 reflect this by showing no difference between bicubic and bilinear interpolation, and the simulation is able to run to completion. Increasing the initial pressure moves the initial state to higher temperature (not linearly) and into a smoother region in both tables, permitting the simulation to run to completion. This smoother region has a 30 percent difference between the BMEOS and SES3720, while the lower initial pressure region has 40 percent difference. This difference is still large and explains the qualitatively different result in the 2 right-most columns of Figure 10. Initial pressure is varied instead of density because the electrical resistivity is highly sensitive to density near reference solid density, as mentioned in Peterson et al. [2], and it would change the η_T value through differences in collisional quanities.

Qualitatively the representative SES3720 and BMEOS simulations show differences late in time, while early in time they show similar smaller wavelength mode structure (not shown here). These differences late in time highlight the importance of the EOS on nonlinear ETI development. For the parameters surveyed in this study, the dependence on interpolation algorithm is not as significant as long as an interpolation scheme is used with higher fidelity than bilinear interpolation.

4.3. Vacuum Resistivity Sensitivity

In this work, the vacuum is treated as a separate material from the liner that has a fixed (i.e., constant) large resistivity ($5.65 \times 10^{-5}\,\Omega\,\mathrm{m}$) while the liner material uses tabulated electrical conductivity (see Section 2.3 and Figure 5). The only difference between the treatment of the liner and vacuum regions in these Ares simulations is in the different electrical and thermal conductivities. The mesh is initialized such that the interface contains multi-material zones which are handled with the method stated in Section 2.2. The presence of multiple-materials due to the liner being ejected into the vacuum is evident in the late-stage evolution presented in Section 4.1 (60 ns and 70 ns).

The vacuum resistivity changes the rate that the magnetic field diffuses through the vacuum and is important in evaluating the ohmic heating due to the spatial variation in resistivity. For explicit codes, the vacuum resistivity should be as low as possible while still achieving a similar result to the infinitely resistive vacuum limit. To determine the role of vacuum resistivity on ETI development, the Ares nonlinear ETI simulations are repeated while multiplying the vacuum resistivity by up to 100 times the nominal value used in the preceding studies ($5.65 \times 10^{-5}\,\Omega\,\mathrm{m}$).

Figure 11 shows the result of varying the resistivity and height of the vacuum. As the resistivity increases in the vacuum, the solution converges as noted in the upper row of Figure 11. Qualitatively, the 5x, 10x, and 100x η_v simulations show no differences, but the 1x and 2x η_v simulations show noticeable differences. The main difference is in the magnitude of density inside the liner hotspots. Figure 12 presents horizontal lineouts at $y = 25\,\mu\mathrm{m}$ for the top row of Figure 11. These lineouts show that the magnitude of density inside the liner hotspots varies greatly (50% at $x = 5\,\mu\mathrm{m}$) between the 1x and 2x runs, and varies

[8] Better as in satisfying monotonicity, or having positive pressure and energy values. Negative values result from the imaginary state space of the Van Der Waal's isotherm loops

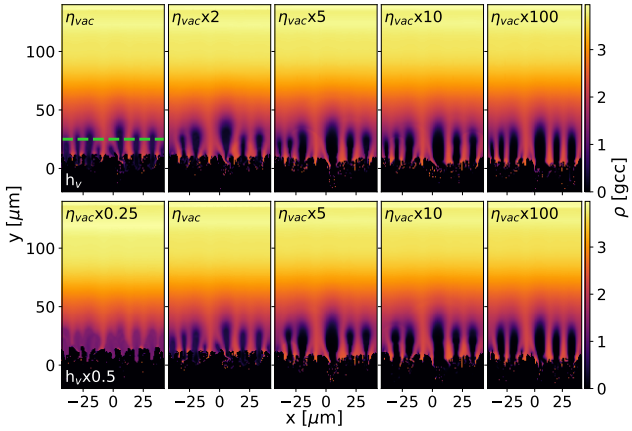

Figure 11: Density evolution of the nonlinear ETI is presented at 60 ns with the resistivity varying by column and the initial height of the vacuum (h_v) varying by row. The bottom row is for half of the vacuum height compared to the top row. The green dashed line indicates the lineout location used for the top row to generate Figure 12.

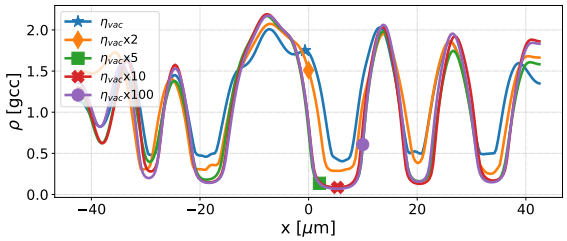

Figure 12: Horizontal lineouts of the top row of Figure 11 is presented for all vacuum resistivity cases with the original vacuum height (h_v). The horizontal lineout, indicated by the dashed green line in the upper leftmost plot of Figure 11, is at $y = 25\,\mu$m for all cases.

little (<5% at $x = 5\,\mu$m) between the 5x, 10x, and 100x runs. These results indicate that a resistivity ratio of approximately $5.65 \times 10^{-4}\,\Omega\,$m (10x which has <1% variation with the 100x run and the not shown 1000x run) is sufficient in capturing ETI in the infinitely resistive limit for this nonlinear ETI setup.

To investigate the underlying mechanism for the converged vacuum resistivity threshold, an additional resistivity scan is performed in a configuration with half the original vacuum height. The vacuum height is the initial spatial distance in the y-direction between the liner-vacuum interface and the outer edge of the vacuum region (lower boundary in the y-direction). For the simulations presented in Figure 11, the vacuum height, h_v, is 100 µm. The bottom row of Figure 11 shows the reduced vacuum size simulations of varying vacuum resistivity. Reducing the vacuum height probes the influence of the characteristic time for the magnetic field to diffuse through the vacuum on ETI development. Reducing the vacuum height by a half would result in a quarter of the vacuum resistivity needed to maintain the same vacuum magnetic diffusion transit time. Reducing the vacuum resistivity needed for a converged result would be beneficial for codes with explicit diffusion algorithms.

The two left-most plots of Figure 11 have the same magnetic diffusion transit time, but show starkly different ETI growth. This implies the vacuum magnetic diffusion transit time is not an underlying mechanism for the converged vacuum resistivity threshold, suprisingly. The converged vacuum resistivity is approximately 5 times the nominal resistivity from previous studies, and is the same for both vacuum sizes. A more relevant scale parameter for the converged results may be the ratio of the liner resistivity to the vacuum resistivity, as this influences the reconstruction of derivatives given the spatially-varying resistivity. Changing the numerical derivatives leads to different values of current through its impact on ohmic heating, thereby producing differences in the nonlinear ETI growth.

Based on these findings, to get the converged ETI result (infinitely resistive vacuum) requires a minimum vacuum-to-liner resistivity ratio of 2×10^4. Ares is used here because of the challenges associated with performing such a convergence study with an explicit diffusion vacuum model, such as with USim's STS diffusion algorithm, so care is needed when checking the convergence of vacuum resistivity using explicit codes.

4.4. Vacuum Density Sensitivity

When simulating a vacuum using a fluid code, the vacuum density is traditionally set relatively low. [2, 4] Not evolving ohmic heating, S_ϵ in Equation 3, and the magnetic acceleration of the vacuum, Equation 2 through $S_{\mathbf{B}}$ in Equation 4, allows for a less restrictive time step by reducing the sound speed. For the nonlinear ETI simulations, the vacuum density is evolved with a floor value of the initial vacuum density ($2.7 \times 10^{-2}\,\mathrm{g\,cm^{-3}}$). Varying

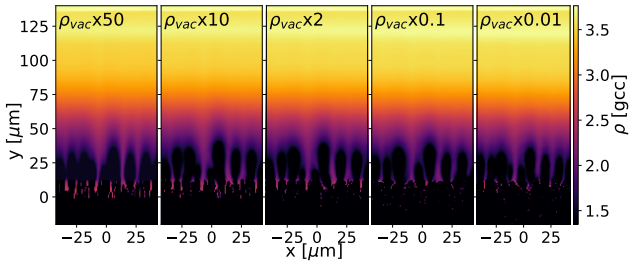

Figure 13: Density evolution of the nonlinear ETI simulations is presented at 60 ns varying the vacuum density.

this floor value determines the effect of vacuum hydrodynamics on nonlinear ETI behavior for this particular setup.

Figure 13 shows the nonlinear ETI simulation at 60 ns for vacuum density varying from 50x to 0.01x of the base vacuum density ($2.7 \times 10^{-5}\,\mathrm{kg\,m^{-3}}$). There is no discernable difference between the simulations in Figure 13. All other values of vacuum density show qualitatively similar results when neglecting ohmic heating and magnetic acceleration of the vacuum. Running with too small of a vacuum density leads to long simulation times due to short time steps required to resolve potential hydrodynamic (acoustic) oscillations in the vacuum. More moderate values of vacuum density of approximately 2 to 3 orders of magnitude lower than the reference liner density produce converged results. Using such a large vacuum density only changes the dynamics when significant vacuum inertia is added that impedes the ablation of the liner. Including magnetic acceleration and ohmic heating would change the outcome of this converged density ratio, but is not explored here.

5. Conclusion

This work compares nonlinear ETI simulations using two different codes with significantly different algorithmic approaches to solving the resistive-MHD equations. Although these codes differ in many ways, the most significant difference, relative to simulating nonlinear ETI, is in the spatial and temporal discretization of the diffusion terms as discussed in Section 2. The handling of these terms directly affects the evaluation of the magnetic diffusion wave and ohmic heating which are both essential in simulating nonlinear ETI growth. Furthermore, the range of viable parameters for stable and efficient computational results is dictated by the discretization methods. For these nonlinear ETI simulation comparisons, a tabulated EOS for aluminum, BMEOS, is developed that compares well with the previously used SES3720 table. [2]

Section 3 shows development of verification test cases evaluating each code's diffusion capabilities for S_ϵ and $S_{\mathbf{B}}$ from Equations 3 and 4, respectively. First, the codes simulate a simple magnetic diffusion test case showing that both codes accurately recover the analytical solution. Next, the codes recover the theoretical linear ETI growth rate shown in Equation 13. Comparing the simulation growth rate to the theoretical one for varying spatial resolution and time step size results in the convergence shown in Figure 4, where the anticipated orders of accuracy of spatial and temporal discretization are obtained. These tests give confidence in each code's ability to handle the fundamental aspects of simulating nonlinear ETI.

Section 4 compares the codes for simulating nonlinear ETI with the baseline setup shown in Figure 5. This simulation has full coupling of both source terms S_ϵ and $S_{\mathbf{B}}$ to the full set of MHD equations, Equations 1-4, and also includes the non-ideal-gas BMEOS. The simulation uses an analytic form for the current rise akin to a typical Z-machine current rise with a correct prepulse as represented in Figure 6. Figures 7-9 show qualitative and quantitative agreement between the two codes, although interesting differences arise in the details of mode evolution.

Additionally, the Ares nonlinear ETI simulation undergoes a sensitivity analysis for the vacuum conditions shown in Sections 4.3 and 4.4. The analyses show a strong dependence on the vacuum resistivity, but not the vacuum density. Specifically, the resistivity analysis shows that a vacuum-to-liner resistivity ratio of $\approx 2 \times 10^4$ is sufficient to capture the converged (i.e., the infinitely resistive vacuum limit) nonlinear ETI simulation. The EOS implementation is tested across different interpolation algorithms, EOS tables, and initial conditions, showing a large dependence of nonlinear ETI growth to the EOS table and interpolation algorithm, specifically near the solid density and low pressure state. These sensitivity analyses provide guidelines for how codes that explicitly integrate diffusion terms can still capture nonlinear ETI without the need for a infinitesimally dense and infinitely resistive vacuum.

Acknowledgement

This work was supported through the Lawrence Livermore National Laboratory Weapons and Complex Integration (LLNL WCI) High Energy Density Fellowship, and through the US Department of Energy under grants DE-SC0016515, DE-SC0016531, & DE-NA0003881. In addition a portion of this work was sponsored by LLNL WCI HED summer program. This research used resources of the National Energy Research Scientific Computing Center (NERSC), a U.S. Department of Energy Office of Science User Facility operated under Contract No. DE-AC02-05CH11231.

A portion of this work was performed under the auspices of the U.S. Department of Energy by Lawrence Livermore National Laboratory under Contract DE-AC52-07NA27344. This document was prepared as an account of work sponsored by an agency of the United States government. Neither the United States government nor Lawrence Livermore National Security, LLC, nor any of their employees makes any warranty, expressed or implied, or assumes any legal liability or responsibility for the accu-

racy, completeness, or usefulness of any information, apparatus, product, or process disclosed, or represents that its use would not infringe privately owned rights. Reference herein to any specific commercial product, process, or service by trade name, trademark, manufacturer, or otherwise does not necessarily constitute or imply its endorsement, recommendation, or favoring by the United States government or Lawrence Livermore National Security, LLC. The views and opinions of authors expressed herein do not necessarily state or reflect those of the United States government or Lawrence Livermore National Security, LLC, and shall not be used for advertising or product endorsement purposes.

References

[1] V. I. Oreshkin, Thermal instability during an electrical wire explosion, Physics of Plasmas 15 (2008) 092103.

[2] K. J. Peterson, D. B. Sinars, E. P. Yu, M. C. Herrmann, M. E. Cuneo, S. A. Slutz, I. C. Smith, B. W. Atherton, M. D. Knudson, C. Nakhleh, Electrothermal instability growth in magnetically driven pulsed power liners, Physics of Plasmas 19 (2012) 092701.

[3] S. A. Slutz, et al., Pulsed-power-driven cylindrical liner implosions of laser preheated fuel magnetized with an axial field), Physics of Plasmas 17 (2010). URL: http://scitation.aip.org/content/aip/journal/pop/17/5/10.1063/1.3333505. doi:http://dx.doi.org/10.1063/1.3333505.

[4] K. J. Peterson, E. P. Yu, D. B. Sinars, M. E. Cuneo, S. A. Slutz, J. M. Koning, M. M. Marinak, C. Nakhleh, M. C. Herrmann, Simulations of electrothermal instability growth in solid aluminum rods, Physics of Plasmas 20 (2013) 056305.

[5] K. J. Peterson, T. J. Awe, E. P. Yu, D. B. Sinars, E. S. Field, M. E. Cuneo, M. C. Herrmann, M. Savage, D. Schroen, K. Tomlinson, C. Nakhleh, Electrothermal instability mitigation by using thick dielectric coatings on magnetically imploded conductors, Phys. Rev. Lett. 112 (2014) 135002. URL: https://link.aps.org/doi/10.1103/PhysRevLett.112.135002. doi:10.1103/PhysRevLett.112.135002.

[6] J. Loverich, S. C. Zhou, K. Beckwith, M. Kundrapu, M. Loh, S. Mahalingam, P. Stoltz, A. Hakim, Nautilus: A tool for modeling fluid plasmas, in: 51st AIAA Aerospace Sciences Meeting including the New Horizons Forum and Aerospace Exposition, Grapevine, Texas, 2013.

[7] B. E. Morgan, J. A. Greenough, Large-eddy and unsteady rans simulations of a shock-accelerated heavy gas cylinder, Shock Waves 26 (2016) 355–383. URL: https://doi.org/10.1007/s00193-015-0566-3. doi:10.1007/s00193-015-0566-3.

[8] C. L. Ellison, H. D. Whitley, C. R. D. Brown, S. R. Copeland, W. J. Garbett, H. P. Le, M. B. Schneider, Z. B. Walters, H. Chen, J. I. Castor, R. S. Craxton, M. Gatu Johnson, E. M. Garcia, F. R. Graziani, G. E. Kemp, C. M. Krauland, P. W. McKenty, B. Lahmann, J. E. Pino, M. S. Rubery, H. A. Scott, R. Shepherd, H. Sio, Development and modeling of a polar-direct-drive exploding pusher platform at the national ignition facility, Physics of Plasmas 25 (2018) 072710. URL: https://doi.org/10.1063/1.5025724. doi:10.1063/1.5025724. arXiv:https://doi.org/10.1063/1.5025724.

[9] R. M. Darlington, T. L. McAbee, G. Rodrigue, A study of ale simulations of rayleigh–taylor instability, Computer Physics Communications 135 (2001) 58–73.

[10] B. Van Leer, Towards the ultimate conservative difference scheme. v. a second-order sequel to godunov's method, Journal of computational Physics 32 (1979) 101–136.

[11] T. Miyoshi, K. Kusano, A multi-state hll approximate riemann solver for ideal magnetohydrodynamics, Journal of Computational Physics 208 (2005) 315–344.

[12] J. R. King, R. Masti, B. Srinivasan, K. Beckwith, Multidimensional tests of a finite-volume solver for mhd with a real-gas equation of state, IEEE Transactions on Plasma Science 48 (2020) 902–913.

[13] A. Dedner, F. Kemm, D. Kröner, C.-D. Munz, T. Schnitzer, M. Wesenberg, Hyperbolic divergence cleaning for the mhd equations, Journal of Computational Physics 175 (2002) 645–673.

[14] V. Alexiades, G. Amiez, P.-A. Gremaud, Super-time-stepping acceleration of explicit schemes for parabolic problems, Communications in numerical methods in engineering 12 (1996) 31–42.

[15] D. Mavriplis, Revisiting the least-squares procedure for gradient reconstruction on unstructured meshes, in: 16th AIAA Computational Fluid Dynamics Conference, 2003, p. 3986.

[16] G. Pert, Physical constraints in numerical calculations of diffusion, Journal of Computational Physics 42 (1981) 20 – 52. URL: http://www.sciencedirect.com/science/article/pii/002199918190231X. doi:https://doi.org/10.1016/0021-9991(81)90231-X.

[17] S. D. Crockett, Al-13, LA-UR-04-6442 (Aug. 28). URL: http://www.lanl.gov/org/padste/adtsc/theoretical/physics-chemistry-materials/_assets/docs/LAUR-92-3407.pdf.

[18] M. Desjarlais, J. Kress, L. Collins, Electrical conductivity for warm, dense aluminum plasmas and liquids, Physical Review E 66 (2002) 025401.

[19] R. D. McBride, S. A. Slutz, A semi-analytic model of magnetized liner inertial fusion, Physics of Plasmas 22 (2015) 052708.

[20] F. Birch, Finite elastic strain of cubic crystals, Phys. Rev. 71 (1947) 809–824. URL: https://link.aps.org/doi/10.1103/PhysRev.71.809. doi:10.1103/PhysRev.71.809.

[21] F. D. Murnaghan, Finite deformations of an elastic solid, American Journal of Mathematics 59 (1937) 235–260. URL: http://www.jstor.org/stable/2371405.

[22] F. D. Murnaghan, The compressibility of media under extreme pressures, Proceedings of the National Academy of Sciences 30 (1944) 244–247. URL: https://www.pnas.org/content/30/9/244. doi:10.1073/pnas.30.9.244. arXiv:https://www.pnas.org/content/30/9/244.full.pdf.

[23] R. More, K. Warren, D. Young, G. Zimmerman, A new quotidian equation of state (qeos) for hot dense matter, The Physics of fluids 31 (1988) 3059–3078.

[24] D. A. Young, E. M. Corey, A new global equation of state model for hot, dense matter, Journal of applied physics 78 (1995) 3748–3755.

[25] F. N. Fritsch, The LEOS Interpolation Package, Technical Report, Lawrence Livermore National Lab., CA (US), 2003.

[26] C. W. Cranfill, EOSPAC: A subroutine package for accessing the Los Alamos SESAME EOS data library, Technical Report, Los Alamos National Lab., NM (USA), 1983.

[27] D. Ryutov, M. S. Derzon, M. K. Matzen, The physics of fast z pinches, Reviews of Modern Physics 72 (2000) 167.

[28] D. B. Sinars, et al., Measurements of magneto-rayleigh-taylor instability growth during the implosion of initially solid metal liners, Physics of Plasmas 18 (2011) 056301. URL: http://aip.scitation.org/doi/abs/10.1063/1.3560911. doi:10.1063/1.3560911. arXiv:http://aip.scitation.org/doi/pdf/10.1063/1.3560911.

[29] J. Pecover, J. Chittenden, Instability growth for magnetized liner inertial fusion seeded by electro-thermal, electro-choric, and material strength effects, Physics of Plasmas 22 (2015) 102701.

Appendix A. Comparison of BMEOS and SES3720

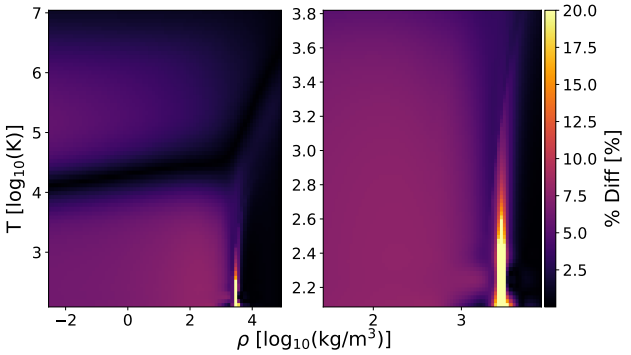

Figure A.14: Percent difference of the specific internal energy density between the BMEOS and SES3720 in the state space relevant to the nonlinear ETI evolution in HED regimes. The plot on the right is an expanded scale of the left plot to highlight the region of largest difference.

Appendix B. Coefficients of the multimode perturbation

mode (i)	β_i
1	0.883494
2	0.313251
3	0.139670
4	0.438109
5	0.642904
6	0.176107
7	0.856669
8	0.630685
9	0.682887
10	0.941226
11	0.236611
12	0.699510
13	0.440243
14	0.124690
15	0.643533
16	0.018313
17	0.415389
18	0.403712
19	0.122180
20	0.313884
21	0.207358
22	0.915150
23	0.038463
24	0.991615
25	0.755673
26	0.558353
27	0.586421
28	0.896183
29	0.305981
30	0.495188
31	0.476349
32	0.057556

Chapter 3

The effect of anomalous resistivity on the fast electrothermal instability

The effect of anomalous resistivity on the fast electrothermal instability

R. L. Masti,[1,2,a)] C. L. Ellison,[1] W. A. Farmer,[1] K. Tummel,[1] and B. Srinivasan[2,b)]
[1)] *Lawrence Livermore National Laboratory, Livermore, CA 94550, USA*
[2)] *Virginia Polytechnic Institute and State University, Blacksburg, VA 24060, USA*

(Dated: May 7, 2021)

This manuscript presents a new theoretical contribution towards the growth rate of the "fast" form of the electrothermal instability (ETI) in the presence of anomalous resistivity (AR). The current-driven ETI is present in all pulsed-power platforms, and has been shown to seed the disruptive magneto Rayleigh-Taylor instability. Fluid simulations of low-density, current-carrying plasmas are often subject to unphysical runaway ohmic heating due to an under predicted resistivity when using purely collisional resistivity models. AR models provide mechanisms to increase the resistivity as the drift speed increases through increased current density. The derivation of a new, generalized growth rate is presented for the ETI, which includes a resistivity that is dependent on current density, and marks the key contributions of this work. This new growth rate is then compared to the growth rate without AR. Although the striation form of the ETI growth rate is unaffected by the inclusion of AR, the filamentation form of the ETI growth rate depends on the AR. Hence, the new growth rate is verified through 3D ETI simulations of the filamentation form of ETI. The impact of AR can be significant: up to twelve orders of magnitude on the temporally-varying local growth rate for a certain choice of parameters. For experimentally relevant conditions based on kinetic simulations, the growth rate can be increased by up to four orders of magnitude if the AR is dominated by the lower-hybrid drift instability.

I. INTRODUCTION

The pulsed-power high energy density (HED) community has exhibited increased interest in the influence of vacuum contaminant plasmas on current delivery[1,2]. These parasitic plasmas can contribute to current loss from the target. In resistive magnetohydrodynamic (MHD) simulations, these contaminant plasmas can experience unphysical runaway heating and cause shorting when a classical resistivity model is applied to the contaminants[3]. A resolution to the discrepancy between the resistive MHD simulations and the experimentally observed current delivery is the presence of anomalous resistivity (AR). An important mechanism at play in these ohmic-heating plasmas is the ubiquitous electrothermal instability (ETI)[4–6], which is always unstable in either the axial or azimuthal direction, depending on the sign of the derivative of the temperature-dependent resistivity. Understanding ETI growth in this vacuum contaminant plasma with AR is important to understanding the dynamic evolution of these systems and, ultimately, the amount of shorting incurred by the contaminant plasma.

In resistive-MHD simulations, the aforementioned runaway heating of the vacuum contaminant plasma can be remedied by approximate collisionless kinetic effects. AR enhances magnetic diffusion and reduces ohmic heating of the weakly collisional plasma. AR augments the collisionally-based resistivity because of micro-turbulent plasma phenomenon driven by an underlying plasma instability, e.g., the ion acoustic instability[7]. Observations of enhanced magnetic diffusion in high-temperature plasmas have motivated the development of AR models, which provide a mechanism to incorporate additional dissipation mechanisms apart from collisions[8–18]. This was observed in both theta and screw pinch plasmas[8–12] and in space and laboratory plasmas[13–18]. These observations have motivated the development of reduced models approximating the effect of these micro-turbulent instabilities on material conductivity[19–22]. This work explores how AR influences the fast thermal instability[6] form of ETI through linear theory, and assesses its relevance in pulsed-power HED regimes.

This fast thermal instability occurs when the thickness of the distributed current is much less than the skin depth (which removes the radial dependence of ETI), and the mechanical motions of the shell are neglible[6]. The canonical ETI theory considers two configurations of the instability: the striation form wherein the perturbation wave vector is perpendicular to the magnetic field (k_z), and the filamentation form wherein the perturbation wave vector is aligned with the magnetic field (k_θ)[4,5]. These two configurations are unstable in complementary configurations dependent on the sign of $\partial\eta/\partial T$ with striation corresponding to $\partial\eta/\partial T > 0$ and filamentation corresponding to $\partial\eta/\partial T < 0$, where η is resistivity and T is temperature.

Traditional ETI theory has only considered a material's resistivity dependence on temperature and density[4–6,23], but the inclusion of AR introduces additional dependencies such as current density. This work examines how AR affects the traditional theory for both the striation and filamentation form of ETI[5], and derives a new growth rate for the filamentation form that includes the resistivity's dependence on current density (Eq. (6)). AR does not affect the functional form of the ETI growth rate in the striation configuration, yet it modifies both the functional form and dramatically al-

[a)] Electronic mail: rlm7819@vt.edu
[b)] Electronic mail: srinbhu@vt.edu

ters the magnitude of the growth rate in the filamentation mode (increasing it by approximately six orders of magnitude in parameter regimes of interest). This increase in growth rate is attributed to the enhancement of the material's resistivity by the micro-turbulence; the added dependence on current density is shown to be stabilizing, but insufficient to overcome the overall enhancement of the instability. *The key contribution of this work is in the derivation of this new theoretical growth rate of the ETI instability that incorporates the effect of AR along with a verification of this growth rate through 3D ETI simulations.*

This work is organized as follows. Section II presents the effect of AR on ETI theory through the derivation of a new growth rate. Section III presents simulation results verifying the theory shown in Sec. II. In the appendix, Sec. A presents the four AR models used in this work, and how these AR models are incorporated into a tabulated collisionally-based resistivity model.

II. ELECTROTHERMAL INSTABILITY THEORY

While aluminum is relevant to the study of ETI in solid density pulsed power targets,[5,24,25] hydrogen is more relevant to the study of ETI in vacuum contaminant plasmas due to the prominent contribution of water in these contaminants[2]. The water desorption process from power flow electrodes is an active area of research for understanding the current loss in the load[1,26,27]. Thus, hydrogen is chosen to study the effect of AR on ETI specifically for the filamentation form of the instability in this section.

For the theory presented here, the skin depth is much greater than the thickness of the annulus, the assumption of which denotes the fast form of ETI[6]. This form of ETI is useful in studying the experiments on mega ampere pulsed-power accelerators. This derivation assumes the radius of the current annulus is much larger than the thickness of the annulus allowing for the use of a Cartesian coordinate system, where the radial, azimuthal, and axial directions are denoted by the x, y, and z directions, respectively. For this derivation, the unperturbed equation system is the conservation of energy equation neglecting radiation, Ampere's law, Faraday's law, and Ohm's law represented as

$$\begin{aligned}\rho\epsilon_T\frac{\partial T}{\partial t} &= \eta|\mathbf{J}|^2,\\ \oint \mathbf{B}\cdot\mathbf{ds} &= \mu_0\int \mathbf{J}\cdot\mathbf{dA}\\ \frac{\partial \mathbf{B}}{\partial t} &= -\nabla\times\mathbf{E},\\ \mathbf{E} &= \eta\mathbf{J},\end{aligned}$$

where ρ is the mass density, ϵ_T is the derivative of specific internal energy density with respect to temperature, $\mathbf{B}$ is the magnetic field, $\mathbf{E}$ is the electric field, and μ_0 is the magnetic permeability of free space. Using Ohm's law, the surface electric field in terms of perturbed resistivity and perturbed current density results in

$$\frac{\delta\mathbf{E}_z}{h} = \eta_s\delta\mathbf{J}_z + \delta\eta_s\mathbf{J}_z, \tag{1}$$

where δ denotes perturbation of the form $\exp[\gamma t + ik_y y + ik_z z]$, and the subscript s denotes surface quantities (e.g. $\eta_s = \eta/h$ where h is the characteristic depth). Faraday's law in Cartesian coordinates gives the perturbed magnetic field in terms of perturbed electric field as

$$\gamma\delta B_x = ik_z\delta E_y - ik_y\delta E_z. \tag{2}$$

Using separation of variables, the curl-free magnetic field on either side of current annulus, and boundary conditions with Ampere's law gives the perturbed x-direction magnetic field in the current annulus as

$$\frac{\delta B_x}{h} = \frac{\mu_0 ik}{2k_y}\delta J_z, \tag{3}$$

where μ_0 is the magnetic permeability of free space, and $k = \sqrt{k_y^2 + k_z^2}$. Combining Eqs. (1) - (3), and noting $J_y = 0$, $k_y^2/k^2 = \cos^2\alpha$, and $\gamma_0 = 2\eta_s k/\mu_0$, the perturbed current densities are

$$\delta J_z = -J_z\frac{\cos^2\alpha}{1+\gamma/\gamma_0}\frac{\delta\eta_s}{\eta_s} \text{ and } \delta J_y = -\frac{k_z}{k_y}\delta J_z, \tag{4}$$

where α is the angle between the perturbation wave vector and the azimuthal magnetic field. These perturbations are then applied to the linearised energy equation, which assumes negligible radiation and thermal conduction effects, resulting in

$$\rho\epsilon_T\gamma\delta T = 2\eta J_z\delta J_z + \delta\eta J_z^2.$$

Expanding the first order quantities (δ),

$$\begin{aligned}\delta\eta &= \delta T\frac{\partial\eta}{\partial T} + \frac{\delta J_z}{\cos\alpha}\frac{\partial\eta}{\partial J},\\ \text{and } \delta T &= \frac{2\eta J_z}{\gamma\rho\epsilon_T}\delta J_z + \frac{J_z^2}{\gamma\rho\epsilon_T}\delta\eta.\end{aligned}$$

Solving this system of equations results in the growth rate of

$$\gamma = \frac{\frac{\partial\eta}{\partial T}J_z^2}{\rho\epsilon_T}\left(1 - \frac{2\cos^2\alpha}{1+\gamma/\gamma_0}\right)\left(1 + \frac{\cos^2\alpha}{1+\gamma/\gamma_0}\frac{\partial\log\eta}{\partial\log J}\right)^{-1}, \tag{5}$$

which contains a novel contribution through the last parenthetic multiplicative term. Unlike previous theoretical growth rates of ETI, this new growth rate formula incorporates the contribution of the current-density-dependent resistivity on the growth of the ETI. When excluding this last parenthetic multiplicative term, it is

identical to Peterson *et al.*[5]. Replacing $\partial\eta/\partial T J_z^2/\rho\epsilon_T \rightarrow \gamma_z$ and solving for γ (positive root) results in

$$\gamma = \frac{1}{2}\left[\gamma_z - \gamma_0^* + \sqrt{\left(\gamma_z - \gamma_0^*\right)^2 - 4\gamma_0\gamma_z\cos 2\alpha}\right], \quad (6)$$

where $\gamma_0^* = \gamma_0(1+\cos^2\alpha(\partial\log\eta/\partial\log J))$. In the limit that $\partial\log\eta/\partial\log J = (J/\eta)\partial\eta/\partial J \rightarrow 0$, Eq. (5) reduces to Eq.(6) from Peterson *et al.*[5]. Eq. (6) contains both the filamentation and the striation form corresponding to $\alpha = 0°$ and $\alpha = 90°$, respectively.

A. Filamentation without current-density-dependent resistivity

Considering the growth without the added current-density dependence is useful in testing the configurations of a filamentation ETI simulation as discussed in Sec. III. The filamentation form of the instability occurs when $\mathbf{k}$ is parallel to $\mathbf{B}$, or $\cos\alpha = 1$. With $\alpha \rightarrow 0$ and $\partial\log\eta/\partial\log J << 1$, Eq. (6) reduces to

$$\gamma = \frac{1}{2}\left[\gamma_z - \gamma_0 + \sqrt{\gamma_z^2 - 6\gamma_z\gamma_0 + \gamma_0^2}\right]. \quad (7)$$

The $\partial\log\eta/\partial\log J$ can be negligible for circumstances where the density and temperature are small. This form, which excludes the current density dependence, is still applicable to studying the effect of including AR at lower temperatures, below approximately 0.25 eV. This is highlighted in the differences between Fig. 1 and Fig 2.

Figure 1 presents the ratio of γ computed from Eq. (7) with AR effects included to when AR effects are excluded. Plots are presented on a log scale for the AR models discussed in Appendix A. Note that this shows the magnitude of the growth can change a maximum of 12 orders of magnitude when AR is included. This means that filamentation instability growth in these high temperature and low density regimes occurs at much shorter time scales than a purely collisionally based resistivity would suggest. Although AR can change the growth rate by a maximum of 12 orders of magnitude, this maximum occurs at much lower-density plasmas (2 orders of magnitude lower) than observed in kinetic simulations of vacuum contaminant plasma from magnetically-insulated transmission lines[2]. The densities of interest ($1.0\times10^{-6}\,\mathrm{g\,cm^{-3}}$ to $1.0\times10^{-7}\,\mathrm{g\,cm^{-3}}$)[2] show the growth rate changing by approximately 4-7 orders of magnitude.

Table I shows the different contributions to the growth rate formula of Eq. (7) for hydrogen at parameters of interest. Using $T = 100\,\mathrm{eV}$ and $\rho = 1.0\times10^{-6}\,\mathrm{g\,cm^{-3}}$ from the kinetic simulations of Welch *et al.*[2], the growth rate is increased a minimum of approximately one order of magnitude with a maximum of approximately five orders of magnitude. The minimum corresponds to the Buneman AR model (Appendix A 2), and the maximum corresponds to the Davidson lower-hybrid-drift (LHD) AR model (Appendix A 3) with the other two models, ion acoustic AR model (Appendix A 1) and Tummel LHD AR model (Appendix A 3), in between. All of the growth rates correspond to time-scales that are less than a nanosecond, making AR directly relevant to 10^7A pulsed-power current pulses with rise times around 100 nanoseconds.

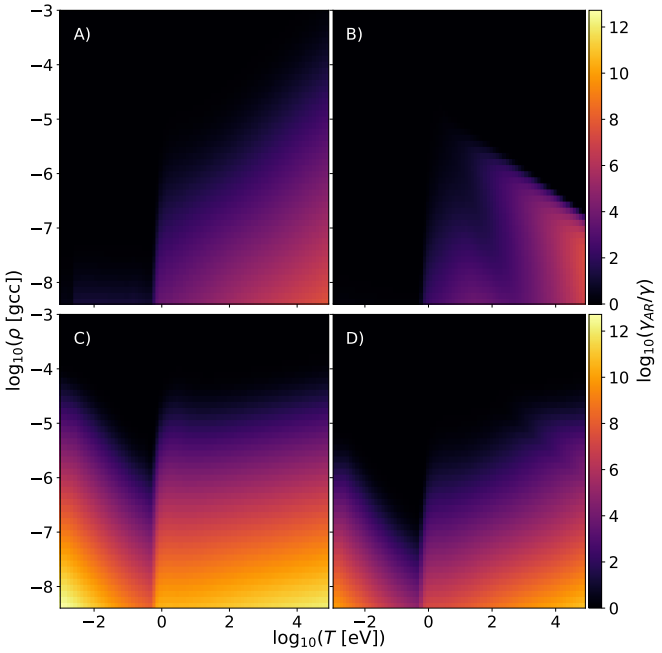

FIG. 1. The ratio of γ (Eq. (7)) when including AR effects to excluding AR effects is plotted for hydrogen at $J_z = 4.06\times10^{11}\,\mathrm{A\,m^{-2}}$, $h = 25\,\mu\mathrm{m}$, and $k_\theta = 5.34\times10^4\,\mathrm{rad\,m^{-1}}$. A), B), C), and D), represent the ion acoustic, Buneman, Davidson lower-hybrid-drift, and Tummel lower-hybrid-drift AR models, respectively. The AR models used here are described in the Appendix A.

B. Filamentation with current-density-dependent resistivity

In Sec. II A the filamentation ETI growth rate is explored neglecting the $\partial\log\eta/\partial\log J$ term. With this term,

$$\gamma = \frac{1}{2}\left[\gamma_z - \gamma_0^* + \sqrt{\left(\gamma_0^* - \gamma_z\right)^2 - 4\gamma_0\gamma_z}\right], \quad (8)$$

where $\gamma_0^* = \gamma_0\,(1+\partial\log\eta/\partial\log J)$. This form is similar to the filamentation ETI growth rate in Eq. (7). To understand the effect of the added current density dependence there are two things to consider: how large is the unit-less quantity $\partial\log\eta/\partial\log J$ compared to unity, and how large is γ_0 relative to γ_z. A fractional change in a large γ_0 relative to γ_z will have a significant impact on the overall growth rate.

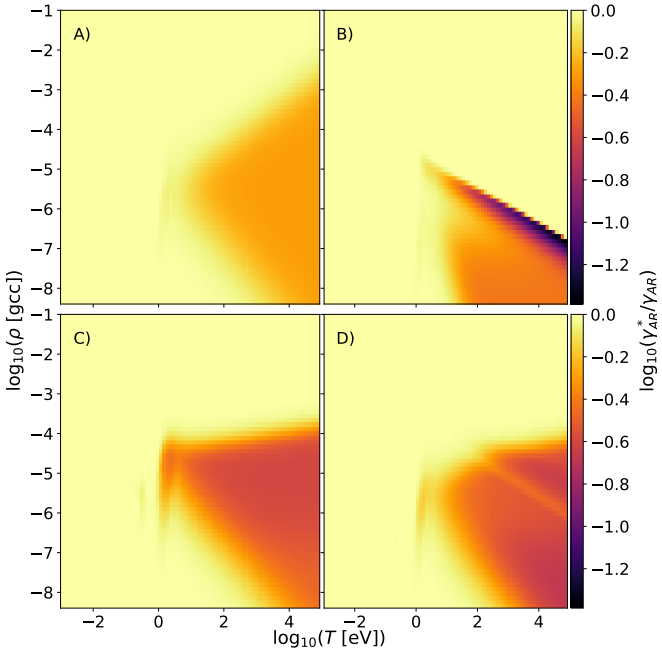

FIG. 2. The ratio of growth rate from Eq. (8) to Eq. (7) representing when the current density dependence is included to when it is excluded for hydrogen. The parameters for these AR models are $J_z = 4.06 \times 10^{11}\,\mathrm{A\,m^{-2}}$, $h = 25\,\mu\mathrm{m}$, and $k_\theta = 5.34 \times 10^4\,\mathrm{rad\,m^{-1}}$. A), B), C), and D), represent the ion acoustic, Buneman, Davidson LHD, and Tummel LHD AR models, respectively.

Figure 2 shows how the current density dependence changes the growth rate for the specified hydrogen conditions. Specifically, this figure compares the ratio of growth rate calculated using Eq. (8) to using Eq. (7). At a maximum, this added dependence reduces the growth rate by up to an order of magnitude, as is the case for the Buneman model. Note this change in the growth rate is in addition to the effect of the $\partial\eta/\partial T$ and η when including the different AR models as shown in Fig (1). In Fig. 2 the added current density dependence does not extend to the lower density and lower temperature regions of the table which showed AR significantly modifying the growth rate in Fig. 1. The ion acoustic AR model has the weakest influence due to the current density dependence because of its linear variation of collision frequency (Eq. (A3)) with drift speed.

Table I presents the growth rate contributions for the filamentation ETI from Eq. (7) resulting in total growth rates of $1.1 \times 10^{11}\,\mathrm{s^{-1}}$, $4.3 \times 10^{10}\,\mathrm{s^{-1}}$, $1.0 \times 10^{14}\,\mathrm{s^{-1}}$, and $2.5 \times 10^{11}\,\mathrm{s^{-1}}$, corresponding to the ion acoustic, Buneman, Davidson LHD, and the Tummel LHD AR models, respectively. Including the effect of current density dependence from Eq (8) would change these total growth rates to $5.9 \times 10^{10}\,\mathrm{s^{-1}}$, $1.1 \times 10^{10}\,\mathrm{s^{-1}}$, $3.5 \times 10^{13}\,\mathrm{s^{-1}}$, and $8.7 \times 10^{10}\,\mathrm{s^{-1}}$, respectively. The added current density dependence then decreases the predicted growth rate (Eq. (7) →Eq. (8)). Although these are only fractional

TABLE I. Tabulated growth rate contributions toward the filamentation ETI in Eq. (7) and Eq. (8) for Hydrogen. The estimates are for $T = 100\,\mathrm{eV}$, $\rho = 1.0 \times 10^{-6}\,\mathrm{g\,cm^{-3}}$, $J_z = 4.06 \times 10^{11}\,\mathrm{A\,m^{-2}}$, $h = 25\,\mu\mathrm{m}$, and $k_\theta = 5.34 \times 10^4\,\mathrm{rad\,m^{-1}}$. The rows correspond to without AR (W/O AR), ion acoustic AR (IA AR), Buneman AR (BU AR), Davidson LHD AR (DA AR), and Tummel LHD AR (TU AR), respectively, and the columns correspond to the different contributions and total growth rate for Eqs. (7) and (8).

unit: $[\mathrm{s^{-1}}]$	$-\gamma_z$	γ_0	γ:Eqn. 7	γ:Eqn. 8
W/O AR	3.7×10^{9}	1.2×10^{10}	2.5×10^{9}	2.5×10^{9}
IA AR	1.3×10^{11}	1.1×10^{12}	1.1×10^{11}	5.9×10^{10}
BU AR	9.0×10^{10}	1.2×10^{11}	4.3×10^{10}	1.1×10^{10}
DA AR	1.4×10^{14}	6.6×10^{14}	1.0×10^{14}	3.5×10^{13}
TU AR	3.0×10^{11}	2.7×10^{12}	2.5×10^{11}	8.7×10^{10}

changes with this added dependence, the time-scales of less than a nanosecond make any variation substantial for a nanosecond current pulse. Additionally, all of the changes reduce the total growth rate, but these reductions will not completely stabilize the filamentation ETI for the AR models chosen here. The reduction in growth rate is expected because of the effective resistivity being directly proportional to current density, where AR effects will oppose the redistribution of current occurring due to the filamentation ETI growth.

C. Striation

The striation form of the instability occurs when $\mathbf{k}$ is perpendicular to $\mathbf{B}$, or $\cos\alpha = 0$. As a result, $\gamma_0^* = \gamma_0$, and

$$\gamma = \gamma_z = \frac{\eta_T J_z^2}{\rho \epsilon_T}. \tag{9}$$

Note that this striation form of the growth rate does not depend on $\partial \log \eta / \partial \log J$. Thus, the only modification to striation growth from incorporated AR arrives through alterations of $\partial\eta/\partial T$.

A material state is striation unstable if the resistivity increases with temperature ($\partial\eta/\partial T > 0$) which is the case for high-density, low-temperature metallic liner material, e.g., copper, aluminum, and beryllium. For aluminum based on the QLMD 29373 table[28] this state region corresponds to densities within 10% of solid density and is reflected in Fig. 3(a). Comparing this region to Fig. 6, there is no overlap between where AR affects resistivity and where the material state is striation unstable. The same is true for hydrogen as shown in Fig. 3(b) and Fig. 7, where this form of the instability occurs at $\approx 0.1\,\mathrm{g\,cm^{-3}}$ to $1.0\,\mathrm{g\,cm^{-3}}$. AR models are derived using kinetic plasma theory, and the region of unstable striation ETI is exclusively for non-plasma states of matter which may explain why the two regions do not overlap.

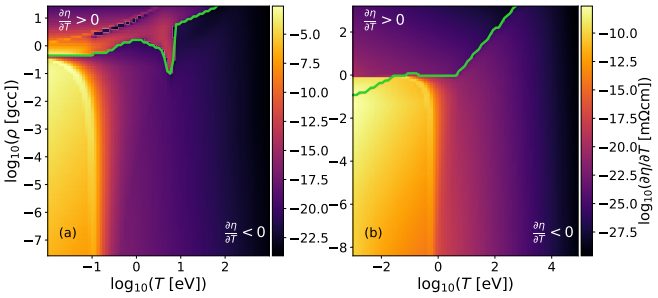

FIG. 3. Log $|\partial\eta/\partial T|$ as a function of log density and log temperature is presented for the aluminum[28] and hydrogen[29] QLMD tables (29373 and 25271) corresponding to the left plot and the right plot, respectively. On each plot there are two distinct regions which are separated by a green line. This green line indicates the location where the bulk $\partial\eta/\partial T$ transitions from greater than to less than zero with the former being striation ETI unstable and the latter filamentation ETI unstable.

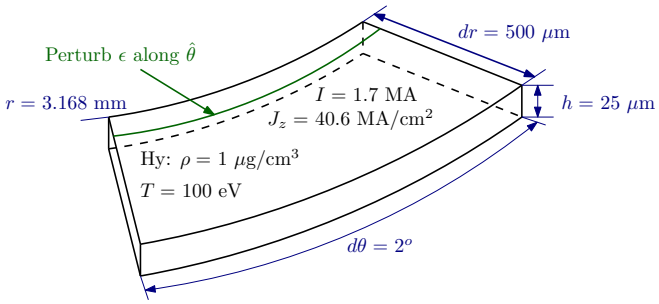

FIG. 4. This schematic presents the simulation setup for hydrogen in a filamentation ETI unstable configuration with relevant initial conditions, length scales, and electric current values. The wedge is radially surrounded with a 62.5 µm thick insulating vacuum region with $\eta = 1.0 \times 10^{10}$ mΩ cm.

Although AR is not important to striation ETI for these conditions, AR can become relevant at very high current densities. As an example, AR will not modify resistivity at solid density and room temperature until the current density exceeds $\approx 1.0 \times 10^{14}\,\mathrm{A\,m^{-2}}$ (a wire with 17 MA of current and radius 200 µm). Simulated current densities near $7.0 \times 10^{12}\,\mathrm{A\,m^{-2}}$ have been reported at fairly high mass density ($0.4\,\mathrm{g\,cm^{-3}}$), but is still not large enough to make AR relevant for striation ETI[24]. Future pulsed-power machines may achieve current densities at high enough mass density to see AR influence striation ETI, where the anomalous collision frequency time-scales are comparable to the electron-ion collision time. Accurate representation of the effects of anomalous resistivity would need to be re-derived in the warm dense matter regime given the strongly coupled character of these high density plasmas.

III. THEORY VERIFICATION AND ANALYSIS

To verify the AR-revised ETI growth rate, 3D filamentation ETI simulations are performed as shown in Fig. 4. This is done in Ares, a multi-physics radiation-hydrodynamics code[30–32]. Only the filamentation mode of ETI is simulated because AR would not influence striation ETI in a physically-relevant regime as shown the Sec. (II C). Ares is used to model pulsed-power experiments, and has been used recently for detailed ETI cross-code comparison[33]. For these simulations, Ares solves the resistive magnetohydrodynamic equations (MHD) without hydrodynamic motion[34]. This is done because ETI occurs even without motion, though there have been studies of the impact of hydrodynamic motion on ETI growth[4]. For more details on the equations being solved, numerical algorithms, see Masti *et al.*[33].

Figure 4 illustrates the domain of the simulation. The radial, azimuthal, and axial zone counts of these simulations are 192, 84, and 2, respectively. All time-relevant quantities such as time step and simulation end time vary because of the large differences in growth rates as observed in Table I across the different models. The time step is approximately one thousandth of the simulation end time which is a varying number of inverse growth rates (1-100) dependent on the increase in temperature.

For this work, a portion of the current in the liner is assumed to be diverted into a surrounding parasitic vacuum hydrogen plasma. Using conditions from Welch *et al.*[2], 17 MA is distributed uniformly over an annulus of outer radius 3.168 mm[35] with a thickness of 500 µm[24]. A diverted current from the liner of 10% (1.7 MA) is distributed uniformly over a thickness of 200 µm based on the findings of Welch *et al.*[2] using low density hydrogen ($\rho = 1\mu$g cm^{-3}) at 100eV. Appendix A 4 provides the justification for incorporating AR effects in this parameter regime when using the presented AR models due to their relevance only at low densities (under $10^{-4}\,\mathrm{g\,cm^{-3}}$).

The current is uniformly distributed over the entire annulus with only a fractional arc length corresponding to one azimuthal wavelength (2°). The internal energy density is perturbed by 1 % along the azimuthal direction to seed the instability. A short azimuthal resolution is used to reduce 3D resolution requirements, and does not significantly affect the comparison of including AR effects to excluding AR effects. As time evolves the deviation of the maximum temperature from the average temperature is tracked to produce Fig. 5 along with averaged temperature and resistivity used in the growth rate equations.

The theory presented in Sec. II is for the "fast" thermal instability[6] where the skin depth is much greater than the thickness of the current-carrying annulus. This assumption implies there is no radial variation in the distribution of heating, but some AR models such as the Buneman, Davidson LHD, and Tummel LHD (Appendix A) depend on the magnetic field. This magnetic field dependence inherently introduces a radial dependence on the resistivity and therefore, on the heating rate. For this reason, this work simulates just the ion acoustic AR model to ver-

ify the newly derived growth rate. To verify the "fast" thermal instability, the magnetic diffusion transit times in the radial direction over the annulus are compared against the inverse growth rates of ETI both with and without AR.

The initial magnetic diffusivity without AR is $5.04 \times 10^5\,\mu\mathrm{m}^2\,\mathrm{ns}^{-1}$ and with ion acoustic AR is $4.58 \times 10^7\,\mu\mathrm{m}^2\,\mathrm{ns}^{-1}$. These would diffuse the magnetic field over the annulus thickness in approximately 79 ps and 0.87 ps, respectively. To assess the assumption that this configuration is indicative of the "fast" thermal instability form discussed in Sec. II, these time scales are compared against inverse ETI growth times. From Table I, the timescales for ETI growth without AR and with ion acoustic AR is roughly 0.4 ns and 0.17 ns, respectively based on Eq (8). These times are larger than their comparative diffusion rate estimates making this configuration a valid simulation setup to study the "fast" thermal instability.

In deriving the growth rates from Sec. II, the heat loss from radiation is assumed to be negligible. To assess the validity of this assumption the power rates are compared. The power induced as a result of ohmic heating is $\eta J_z^2 \approx 7.5 \times 10^{16}\,\mathrm{W\,m^{-3}}$, and the power radiated, assuming a blackbody, would be $\sigma T^4/r \approx 3.246 \times 10^{19}\,\mathrm{W\,m^{-3}}$ for this configuration where r is the radius. This large difference between radiative cooling and ohmic heating would negate any ETI growth due to this large dissipative cooling rate. But when including the ion acoustic AR, this ohmic heating rate increases by more than 2 orders of magnitude making it comparable to the radiative cooling loss. Including the Davidson LHD AR model would increase ohmic heating rate by 5 orders of magnitude making it much larger than the radiative cooling rate. As T increases due to ETI, the radiative cooling eventually overwhelms the non-uniform ohmic heating due to ETI for resistivities that decrease with temperature slower than T^{-4}, which is the case for the models considered here. The increase in resistivity due to these AR models increases this maximum perturbed temperature. For these simulations, hydrogen is considered at $T = 100\,\mathrm{eV}$ and $\rho = 10^{-6}\mathrm{g\,cm^{-3}}$ based on Welch *et al.*[2]. For a cooler plasma at $T = 10\,\mathrm{eV}$, the ohmic heating rate would be over 4 orders of magnitude higher than radiative cooling without AR and would be substantially higher with AR. So although radiative cooling can have a substantial influence on the ETI growth, when including AR effects ohmic heating rates become comparable (for the considered current density) and can exceed radiative cooling rates. Additionally, this assumes a perfect black body emitter which is not entirely accurate for these magnetized low-density, high-temperature plasmas surrounding dense metal target liners. The metal target liners themselves act as black body emitters partially canceling out the radiative loss.

Figure 5 presents simulated perturbation growth and ETI growth rate of the simulation setup shown in Fig. 4. The filamentation growth rate without $\partial\eta/\partial J$ dependence, Eq. (7), and with $\partial\eta/\partial J$ dependence, Eq. (8) both have dependencies on the instantaneous resistivity via γ_0. This dependence causes the growth rate to be transient in nature. Note that the ratio of $\gamma/(\partial\gamma/\partial t)$ is still large in comparison to the simulation time which makes the assumptions used in deriving the growth rate still valid, e.g., the reduced form of Faraday's law in Eq (2). Thus, in comparing theory to simulation in Fig. 5,

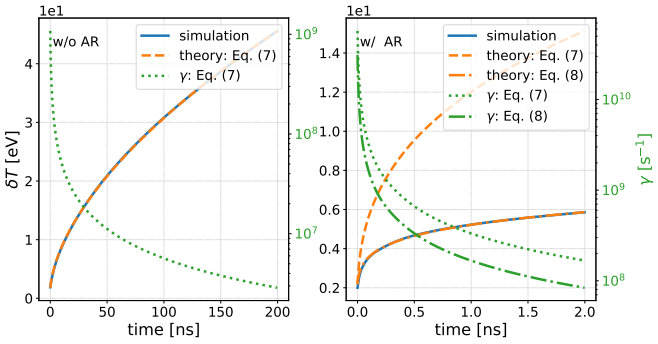

FIG. 5. Simulation results are presented excluding AR (left) and including ion acoustic AR (right). Each figure shows perturbed temperature and corresponding growth rate as a function of time, with the perturbed temperature compared with the theoretical prediction using Eq. (10). All dashed lines represent the result of using Eq. (7) which applies for the case without AR in the left plot as well as the case with AR but without a $\partial\eta/\partial J$ dependence in the right plot. All dash-dot lines represent the result of using Eq. (8) which incorporates AR with the $\partial\eta/\partial J$ dependence (right). The solid blue line represents the simulated perturbed temperature growth and the orange line represents the predicted perturbation growth from Eq. (10). Blue and orange lines correspond to the left vertical axis and green lines correspond to the right vertical axis of each plot.

$$\delta T = \delta T_0 \exp\left[\int \gamma dt\right], \tag{10}$$

is used where δT, δT_0, γ, and t, are the instantaneous perturbation magnitude, initial perturbation magnitude, transient growth rate, and time. The instantaneous perturbation magnitude is obtained from the simulation through measuring the peak-to-valley amplitude of the difference between temperature and average bulk temperature along the green line of Fig 4. As a result of the time-varying growth rate, the perturbation growth is not exponential as seen in Fig. 5 with the blue and orange lines.

The perturbation growth from theory is computed using Eq. (10) as described and the perturbation growth from simulation is directly calculated from the numerical output. These perturbation growths along with the growth rates without and with AR are presented in Fig. 5. The left plot of Fig. 5 shows the perturbation growth without AR, i.e., no $\partial\eta/\partial J$ dependence and no AR contribution to the resistivity, producing agreement to within 5% between theory (Eq. (7) denoted by the

dashed orange line) and simulation (denoted by the blue line) in the absence of AR.

Note that Eq. (7) captures the effect of not including any AR contribution to the resistivity as well as including AR without any $\partial\eta/\partial J$ dependence. This is the key difference between the perturbation growth (dashed orange line) and the growth rate (dotted green line) in the left and right plots of Fig. 5 with the right plot including AR. The right plot of Fig. 5 shows the perturbation growth and growth rate when ion acoustic AR is included without and with the $\partial\eta/\partial J$ contribution. The perturbation growth with AR but without the $\partial\eta/\partial J$ dependence in the right plot (dashed orange line) and the corresponding growth rate (dotted green line) are significantly different from the left plot which does not include any AR. Also, note the difference in the time scales between the left and right plots associated with growth. In the right plot, when including AR without the $\partial\eta/\partial J$ dependence, there is a significant difference between the theory (orange dashed line) and simulation (blue line) perturbation growths. When the $\partial\eta/\partial J$ contribution to the growth rate is included (green dash-dot line) as shown in the right plot with AR, the simulation perturbation growth (blue line) agrees with the theory in Eq. (8) (orange dash-dot line) to within 5%. This agreement illustrates that when AR effects are included one must account for the dependence on electric current density in determining ETI growth rates.

From the right plot of Fig. 5, the theoretical prediction with AR shows a reduction in the perturbed temperature growth. This is consistent with the initial values from the two right-most columns of Table I, and the reduction in growth shown in Fig. 2. Although the $\partial\eta/\partial J$ term reduces the growth rate, including AR increases the overall ohmic heating rate.

The results presented here highlight three main conclusions. First, the newly-derived generalized growth rate presented in this work agrees with simulation as shown in the right plot of Fig. 5 (blue and orange dash-dot curves). Second, the $\partial\eta/\partial J$ term reduces the growth rate. Lastly, AR causes ohmic heating power to be comparable and exceed the radiative dissipative power. This makes current-carrying, low-density, and low-temperature plasmas ideal conditions to experimentally validate AR models where the radiative condensation instability[6,36,37] is not as prevalent as ETI.

IV. SUMMARY AND CONCLUSIONS

Section II derives and presents a new ETI growth rate that includes the dependence of anomalous resistivity, including the novel contribution of the current density dependence of resistivity on the ETI growth rate. This added dependence has no effect on the striation form of ETI, and the highest current densities currently accessible are not significant enough to affect the growth rate. However, the filamentation ETI exhibits the effect of AR more than striation because of its application in the low density regime of vacuum contaminant plasma where AR is relevant (Fig. 3).

Appendix A presents the effects of including several AR models in combination with the tabular conductivity models for parameters of interest to pulsed power experiments. With realistic conditions based on Welch *et al.*[2], AR produces a significant increase in resistivity for both aluminum and hydrogen as shown in Figs. 6 and 7, respectively. The effect of AR is significant in the low density regions for both aluminum and hydrogen, at orders of magnitude less than atmospheric densities.

AR's influence on filamentation ETI growth is highlighted in Fig. 1 showing the ratio of the growth rate when including AR to excluding AR for the hydrogen configuration. AR increases the growth rate by many orders of magnitude, but the added dependence on current density (Eq. 8) mitigates this increase in growth as shown in Fig. 2. Table I shows values relevant to Eq. 7 and 8 for hydrogen at $1.0 \times 10^{-6}\,\mathrm{g\,cm^{-3}}$ and 100 eV.

Section III presents simulation results of the filamentation ETI growth (problem setup in Fig. 4) that verify the newly derived growth rate in Eq. 8, and highlight the important role of AR when simulating ETI through a comparison of ohmic heating rates to radiative cooling rates. Theory compares well with simulation resulting in less than 5 % difference globally as shown in Fig. 5. The inclusion of the current density dependence is shown to substantially reduce the growth rate due to ohmic heating as illustrated in Fig. 2(a).

The revised "fast" thermal instability growth rate in Eq. 8 is verified through simulation. Material state regions for which AR is relevant and impacts resistivity are explored, and its subsequent effect on ETI growth is investigated. AR is shown to not significantly impact the striation form of ETI, but has a significant impact on the filamentation form. Which AR model is appropriate for a given situation depends on the relative strength of the drift speed to the electron and ion thermal speeds and the relative strength of the magnetic field.

Once experimental data of vacuum contaminant plasma for pulsed-power experiments becomes available, future work can explore the role of AR and current-density-dependent resistivity in a more quantitative manner for specific experimental parameters. As an alternative to experimental validation through vacuum contaminant plasmas, the gas-puff staged Z-pinch[38,39] provides accessible experimental date to validate this growth rate when using AR models. The density in a gas-puff staged Z-pinch is $1.0 \times 10^{17}\,\mathrm{cm^{-3}}$ which corresponds to a mass density of $1.0 \times 10^{-6}\,\mathrm{g\,cm^{-3}}$ at 780 kA[38]. This corresponds to an approximate current density of $1 \times 10^{7}\,\mathrm{A\,cm^{-2}}$ evaluated from the Narkis *et al.*[38] semi-analytical model which indicates AR could have a significant impact. Although the gas-puff staged Z-pinch would provide experimental validation, it is outside the scope of this paper.

ACKNOWLEDGEMENT

This work was supported through the Lawrence Livermore National Laboratory Weapons and Complex Integration (LLNL WCI) High Energy Density Fellowship, and through the US Department of Energy under grant DE-NA0003881. In addition a portion of this work was sponsored by LLNL WCI HED summer program.

A portion of this work was performed under the auspices of the U.S. Department of Energy by Lawrence Livermore National Laboratory under Contract DE-AC52-07NA27344. This document was prepared as an account of work sponsored by an agency of the United States government. Neither the United States government nor Lawrence Livermore National Security, LLC, nor any of their employees makes any warranty, expressed or implied, or assumes any legal liability or responsibility for the accuracy, completeness, or usefulness of any information, apparatus, product, or process disclosed, or represents that its use would not infringe privately owned rights. Reference herein to any specific commercial product, process, or service by trade name, trademark, manufacturer, or otherwise does not necessarily constitute or imply its endorsement, recommendation, or favoring by the United States government or Lawrence Livermore National Security, LLC. The views and opinions of authors expressed herein do not necessarily state or reflect those of the United States government or Lawrence Livermore National Security, LLC, and shall not be used for advertising or product endorsement purposes.

This document has been approved for release under the release identifier LLNL-JRNL-816903.

DATA AVAILABILITY

The data that support the findings of this study are available from the corresponding author upon reasonable request.

[1]M. Gomez, R. Gilgenbach, M. Cuneo, C. Jennings, R. McBride, E. Waisman, B. Hutsel, W. Stygar, D. Rose, and Y. Maron, Physical Review Accelerators and Beams **20**, 010401 (2017).
[2]D. Welch, N. Bennett, T. Genoni, D. Rose, C. Thoma, C. Miller, and W. Stygar, Physical Review Accelerators and Beams **22**, 070401 (2019).
[3]C. Seyler, M. R. Martin, and N. Hamlin, Physics of Plasmas **25**, 062711 (2018).
[4]V. I. Oreshkin, Physics of Plasmas **15**, 092103 (2008).
[5]K. J. Peterson, D. B. Sinars, E. P. Yu, M. C. Herrmann, M. E. Cuneo, S. A. Slutz, I. C. Smith, B. W. Atherton, M. D. Knudson, and C. Nakhleh, Physics of Plasmas **19**, 092701 (2012).
[6]D. Ryutov, M. S. Derzon, and M. K. Matzen, Reviews of Modern Physics **72**, 167 (2000).
[7]W. M. Manheimer and R. Flynn, Physical Review Letters **27**, 1175 (1971).
[8]D. Baker, L. Burkhardt, J. Dimarco, P. Forman, A. Haberstich, H. Karr, L. Mann, J. Phillips, and A. Schofield, in *Plasma Physics and Controlled Nuclear Fusion Research 1971. Vol. I. Proceedings of the Fourth International Conference on Plasma Physics and Controlled Nuclear Fusion Research* (1971).
[9]A. DeSilva, W. Dove, I. Spalding, and G. Goldenbaum, The Physics of Fluids **14**, 42 (1971).
[10]N. Bretz and A. DeSilva, Physical Review Letters **32**, 138 (1974).
[11]Y. Maron, E. Sarid, O. Zahavi, L. Perelmutter, and M. Sarfaty, Physical Review A **39**, 5842 (1989).
[12]K. McKenna, R. Kristal, and K. Thomas, Physical Review Letters **32**, 409 (1974).
[13]A. Divin, Y. V. Khotyaintsev, A. Vaivads, M. André, S. Markidis, and G. Lapenta, Journal of Geophysical Research: Space Physics **120**, 2675 (2015).
[14]M. Zhou, H. Li, X. Deng, S. Huang, Y. Pang, Z. Yuan, X. Xu, and R. Tang, Journal of Geophysical Research: Space Physics **119**, 8228 (2014).
[15]R. Torbert, J. Burch, B. Giles, D. Gershman, C. Pollock, J. Dorelli, L. Avanov, M. Argall, J. Shuster, R. Strangeway, *et al.*, Geophysical Research Letters **43**, 5918 (2016).
[16]S. C. Hsu, T. Carter, G. Fiksel, H. Ji, R. Kulsrud, and M. Yamada, Physics of Plasmas **8**, 1916 (2001).
[17]R. Commisso and H. R. Griem, Physical Review Letters **36**, 1038 (1976).
[18]H. Ji, S. Terry, M. Yamada, R. Kulsrud, A. Kuritsyn, and Y. Ren, Physical review letters **92**, 115001 (2004).
[19]K. Papadopoulos, Reviews of Geophysics **15**, 113 (1977).
[20]R. Davidson and N. Krall, Nuclear Fusion **17**, 1313 (1977).
[21]S. P. Gary, The Physics of Fluids **23**, 1193 (1980).
[22]K. Tummel, C. Ellison, W. Farmer, J. Hammer, J. Parker, and K. Lechien, Physics of Plasmas **27**, 092306 (2020).
[23]K. Wang, Z. Shi, H. Xu, and J. Zhao, Physics of Plasmas **27**, 112102 (2020).
[24]K. J. Peterson, E. P. Yu, D. B. Sinars, M. E. Cuneo, S. A. Slutz, J. M. Koning, M. M. Marinak, C. Nakhleh, and M. C. Herrmann, Physics of Plasmas **20**, 056305 (2013).
[25]T. J. Awe, "Electrothermal instability evolution on z-pinch rods and imploding liners pulsed with intense current." Tech. Rep. (Sandia National Lab.(SNL-NM), Albuquerque, NM (United States), 2016).
[26]J. M. D. Lane, K. Leung, A. P. Thompson, and M. E. Cuneo, Journal of Physics: Condensed Matter **30**, 465002 (2018).
[27]B. T. Hutsel, P. A. Corcoran, M. E. Cuneo, M. R. Gomez, M. H. Hess, D. D. Hinshelwood, C. A. Jennings, G. R. Laity, D. C. Lamppa, R. D. McBride, J. K. Moore, A. Myers, D. V. Rose, S. A. Slutz, W. A. Stygar, E. M. Waisman, D. R. Welch, and B. A. Whitney, Phys. Rev. Accel. Beams **21**, 030401 (2018).
[28]M. Desjarlais, J. Kress, and L. Collins, Physical Review E **66**, 025401 (2002).
[29]M. P. Desjarlais, Contributions to Plasma Physics **41**, 267 (2001).
[30]B. E. Morgan and J. A. Greenough, Shock Waves **26**, 355 (2016).
[31]C. L. Ellison, H. D. Whitley, C. R. D. Brown, S. R. Copeland, W. J. Garbett, H. P. Le, M. B. Schneider, Z. B. Walters, H. Chen, J. I. Castor, R. S. Craxton, M. Gatu Johnson, E. M. Garcia, F. R. Graziani, G. E. Kemp, C. M. Krauland, P. W. McKenty, B. Lahmann, J. E. Pino, M. S. Rubery, H. A. Scott, R. Shepherd, and H. Sio, Physics of Plasmas **25**, 072710 (2018), https://doi.org/10.1063/1.5025724.
[32]R. M. Darlington, T. L. McAbee, and G. Rodrigue, Computer Physics Communications **135**, 58 (2001).
[33]R. Masti, C. Ellison, J. King, P. Stoltz, and B. Srinivasan, High Energy Density Physics **38**, 100925 (2021).
[34]W. Farmer, C. Ellison, and J. Hammer, Physics of Plasmas **26**, 072120 (2019).
[35]D. B. Sinars *et al.*, Physics of Plasmas **18**, 056301 (2011), http://aip.scitation.org/doi/pdf/10.1063/1.3560911.
[36]G. B. Field, The Astrophysical Journal **142**, 531 (1965).
[37]I. Aranson, B. Meerson, and P. V. Sasorov, Physical Review E **47**, 4337 (1993).
[38]J. Narkis, H. Rahman, J. Valenzuela, F. Conti, R. McBride, D. Venosa, and F. Beg, Physics of Plasmas **26**, 032708 (2019).
[39]H. Rahman, E. Ruskov, P. Ney, F. Conti, J. Valenzuela, N. Aybar, J. Narkis, F. Beg, E. Dutra, and A. Covington, Physics of Plasmas **26**, 052706 (2019).

[40]L. Spitzer, *Physics of Fully Ionized Gases* (1956).
[41]D. Baldwin and G. Rowlands, The Physics of Fluids **9**, 2444 (1966).
[42]B. Kadomstev, A. Mikhailovskii, and A. Timofeev, rn **2**, 4ne2n0 (1965).
[43]S. L. Ossakow, Journal of Geophysical Research **73**, 6366 (1968).
[44]A. Galeev and R. Sagdeev, RvPP **7**, 257 (1979).
[45]V. N. Tsytovich, in *Nonlinear Effects in Plasma* (Springer, 1970) pp. 1–19.
[46]P. C. Liewer and N. Krall, The Physics of Fluids **16**, 1953 (1973).
[47]V. Y. Bychenkov, V. P. Silin, and S. Uryupin, Physics Reports **164**, 119 (1988).
[48]O. Buneman, Physical Review **112**, 1504 (1958).
[49]J. Huba, in *Symposium-International Astronomical Union*, Vol. 107 (Cambridge University Press, 1985) pp. 315–328.
[50]S. D. Crockett, Los Alamos National Laboratory, Los Alamos, NM, Report No. LA-UR-04-6442 (2004).
[51]R. More, K. Warren, D. Young, and G. Zimmerman, The Physics of fluids **31**, 3059 (1988).
[52]D. A. Young and E. M. Corey, Journal of applied physics **78**, 3748 (1995).
[53]F. N. Fritsch, "The leos interpolation package," Tech. Rep. (Lawrence Livermore National Lab., CA (US), 2003).

Appendix A: Anomalous Resistivity

Anomalous resistivity (AR) is an avenue by which collisionless micro-turbulent effects are incorporated into an otherwise collisional resistivity model. The inclusion of these effects is particularly important in low density regions where collisional resistivity models predict a near infinitely conductive medium in the high temperature limit. This is apparent in the Spitzer resistivity[40], which is weakly dependent on the electron density (only via the Coulomb Log) and dependent on the electron temperature ($\propto T^{-3/2}$). This section introduces how AR models are incorporated into a tabulated resistivity and investigates their effect on two relevant materials considered in this work, hydrogen and aluminum, using conditions based on Welch *et al.*[2].

The ion acoustic, Buneman, and lower-hybrid drift based micro-turbulent phenomena are chosen because they have different dependencies on magnetic field, temperature, and current density. Although which model is appropriate for a given situation is beyond the scope of this manuscript, we highlight several relevant criteria for the models to be valid. The ion acoustic instability occurs when $v_d \sim \bar{v}_i$, where v_d is the drift speed of electrons relative to ions and $\bar{v}_i$ is the ion thermal speed, and when the free electron temperature ($Z_{\text{eff}}T_e$) is greater than the ion temperature. The derivation neglects magnetic fields. In attempting to generalize this theory to include a magnetic field, the Landau-Bernstein paradox arises[41], and we know of no theory describing a magnetized ion-acoustic instability. However, the lack of a magnetic field makes it useful for the verification study in Sec. III. The Buneman instability occurs at much larger drift speeds, $v_d \sim \bar{v}_e$, where $\bar{v}_e$ is the electron thermal speed. These large drifts can occur at the current densities and temperatures relevant to vacuum contaminant plasmas, making it of interest to this study. The two lower-hybrid drift (LHD) instability models (Davidson LHD[20] and Tummel LHD[22]) are formulated using kinetic simulations and theory and are presented in Sec. A 3. The lower-hybrid model by Tummel *et al.*[22] highlights recent developments in AR models for regimes relevant to Z-machine vacuum contaminant plasmas. Although there are additional AR models in the literature, these four AR models cover a representative set of models for current-driven applications.

Quasi-linear models of these micro-turbulent phenomena produce an AR through a corresponding anomalous collisional frequency. The form of the AR is given by

$$\eta_{\text{AR}} \equiv \eta\tau_{ei}\nu_{\text{AR}} = \frac{m_e m_i}{e^2 Z_{\text{eff}}\rho}\nu_{\text{AR}}, \tag{A1}$$

where η_{AR}, τ_{ei}, m_e, m_i, e, Z_{eff}, ρ, and ν_{AR}, are AR, electron-ion collision time, electron mass, ion mass, elementary charge, effective ionization level, mass density, and AR electron scattering frequency, respectively. Note that Eq. (A1) can include multiple AR models through the addition of their corresponding AR electron scattering frequency.

The total resistivity is the addition of the classical resistivity and the AR. This effective resistivity is

$$\eta_{\text{eff}} = \eta + \eta_{\text{AR}} = \eta\left(1 + \tau_{ei}\nu_{\text{AR}}\right), \tag{A2}$$

where η is the collisional resistivity and η_{AR} is the anomalous resistivity. In this equation, η can have an analytical form such as the Spitzer resistivity formula[40], or a tabulated resistivity. By incorporating AR effects into a collisionally-based tabulated resistivity, the resistivity dependencies are expanded beyond just density and temperature. The effective resistivity becomes a function of density, temperature, current density ($\mathbf{J}$), magnetic field ($\mathbf{B}$), and effective ionization level. The expansion of the dependencies of resistivity will modify the ETI growth rate.

Sections A 1-A 3 detail the four different models used for ν_{AR} in this study. Some of these models treat the plasma using a two-temperature model, but for this work, we assume a single material temperature $T_e = T_i = T$. An analysis of how a two-temperature model influences ETI is outside of the scope of this work.

1. Ion Acoustic

The current-driven ion acoustic instability occurs when electrons traveling near the phase velocity of the ion acoustic wave interact with this ion acoustic wave. This instability has been used for anomalous transport for decades for applications ranging from fusion plasmas to atmospheric plasmas.[42–47]

For this work, the form of ν_{AR} is given by[20,44,46]

$$\nu_{\text{IA}} = 6\sqrt{\frac{\pi}{2}}\frac{\omega_e}{n_e T_e}\epsilon,$$

where $\nu_{\rm IA}$, ω_e, n_e, T_e, and ϵ, are AR collision frequency, electron plasma frequency, electron number density, electron temperature, and energy density, respectively. Using the saturated ϵ from Bychenkov, Silin, and Uryupin [47] the saturated anomalous collision frequency is

$$\nu_{\rm IA} = 2.8 \times 10^{-2} \omega_i \frac{v_d}{c_s} \frac{Z_{\rm eff} T_e}{T_i}, \tag{A3}$$

where ω_i, v_d, c_s, and T_i, are ion plasma frequency, drift speed, sound-speed, and ion temperature, respectively. Note the drift speed (j/en_e) has an inverse dependence on the mass density, thus for low density plasmas this becomes quite large. The parameter scan shown in the paper vary the mass density and electron temperature, and this AR model varies like $n^{-1}T_e^{0.5}$., and its temperature dependence will directly influences ETI growth as shown in Sec. II.

2. Buneman

The Buneman instability is the classic two-stream instability between electrons and ions.[48] It has been studied for anomalous transport extensively for a wide range of applications.[19,20,46] Specifically, the formulation from Liewer and Krall [46] with some modification is used in this work. The assumptions are that the drift speed is on the order of the electron thermal speed, the magnetic field is aligned with the perturbation growth, and the electron thermal speed is larger than the ion speed. These assumptions lead to the following form of anomalous collision frequency[46]

$$\nu_{\rm BU} = \frac{1+A^2}{A^2} \gamma_B \frac{2\epsilon_B}{n_e m_e v_d^2},$$

where A is the ratio of electron plasma frequency to electron cyclotron frequency, and γ_B is the instability growth rate. For this work the max ϵ_B of $1/2 n_e m_e v_d^2$ is used resulting in the instability growth rate

$$\gamma_B = \frac{\sqrt{3}}{2} \omega_e \left(\frac{m_e Z_{\rm eff}}{2 m_i} \right)^{\frac{1}{3}} \left(\frac{1+A^2}{A^2} \right)^{\frac{5}{6}} \exp\left[-\frac{v_e^2}{v_d^2} \right], \tag{A4}$$

where v_e is the electron thermal speed ($\sqrt{T_e/m_e}$). Unlike the ion acoustic form of the anomalous collision frequency the temperature dependence is more pronounced through the electron thermal speed. The Buneman insability is only present for large currents where the electron drift speed is large relative to the ion acoustic speed and electron thermal speed.

3. Lower-Hybrid Drift

The lower-hybrid drift instability is a kinetic instability in magnetized plasmas where the electron temperature is less than the ion temperature (opposite for ion acoustic turbulence). Davidson and Krall [20] proposed the lower-hybrid drift instability for anomalous transport in solenoidal fusion plasmas. The most widely known saturated anomalous collision frequency is given by[49]

$$\nu_{\rm DA} = \frac{(v_d/v_i)^2}{\sqrt{(\Omega_i \Omega_e)^{-1} + \omega_i^{-2}}}, \tag{A5}$$

where Ω_i, Ω_e, and v_i, are ion cyclotron frequency, electron cyclotron frequency, and ion thermal speed, respectively. The denominator is the lower-hybrid drift frequency ($1/\omega_{\rm LH}$).

Additonally, there is a newly developed form by Tummel *et al.* [22] which has direct application to these vacuum contaminant plasmas. The Tummel LHD model, a generalization of Eq. (A5), is given by

$$\nu_{\rm TU} = \frac{16\pi c^2 e^2 n_e}{5 m_e} \frac{v_e \tau^{\frac{1}{4}}}{v_i \Omega_e} \frac{m_e}{m_i} \left(\frac{\bar{j}}{1+\tau} \right)^2 \left(\frac{\Omega_e}{\omega_e} \right)^2 \left(\frac{\sqrt{\pi}}{2} \frac{\bar{j}}{1+\tau} \exp\left[-\bar{j}^2 \right] + \frac{1}{2\tau} \left(1 + \frac{\Omega_e^2}{\omega_e^2} \right) \exp\left[-\frac{\sqrt{2\tau}}{2\bar{j}} \right] \right), \tag{A6}$$

where c is the speed of light, and $\bar{j} = j/(en_e v_i)$. This form is extensive and informed through kinetic simulations of the lower-hybrid drift instability. For this study the anomalous collision is described in Equations A3, A4, A5, and A6, representing the ion acoustic, Buneman, Davidson LHD, and Tummel LHD AR models, respectively. Note that the Buneman, Davidson LHD, and Tummel LHD AR models all depend on the magnetic field via cyclotron frequency. For this work, the magnetic field for each of the models is set to the maximum magnetic field in the current annulus $|B_\theta| = \mu_0 I/(2\pi r)$ where I is the total current and r is the outer radius of the annulus.

4. Significance of AR on Tabulated Resistivity

To visualize the effect of AR on a representative configuration, we assume a uniformly distributed current in some annulus and use QLMD table 29373[28] and SESAME 3720[50] for aluminum. Using conditions from Welch *et al.* [2], 17 MA is distributed uniformly over an

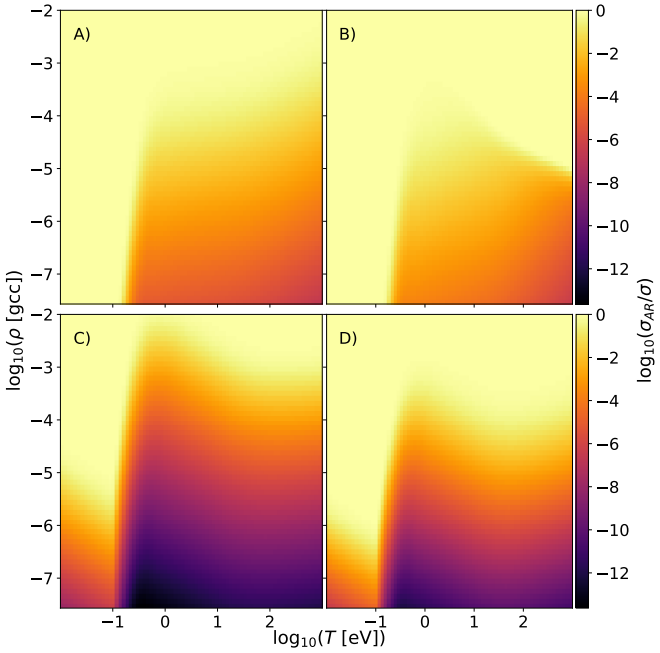

FIG. 6. Plot of $\eta_{\text{table}}/\eta_{\text{eff}}$ (note $\sigma = 1/\eta$) for aluminum with a current density of $j = 1.8 \times 10^{11}\,\text{A}\,\text{m}^{-2}$. A), B), C), and D), represent the ion acoustic, Buneman, Davidson LHD, and Tummel LHD AR models, respectively.

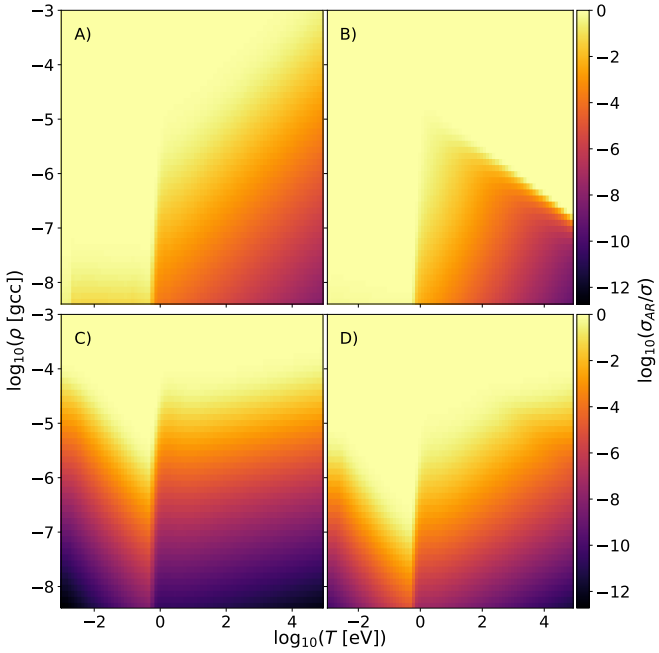

FIG. 7. Plot of $\eta_{\text{table}}/\eta_{\text{eff}}$ (note $\sigma = 1/\eta$) for hydrogen with a current density of $j = 4.0 \times 10^{10}\,\text{A}\,\text{m}^{-2}$. A), B), C), and D), represent the ion acoustic, Buneman, Davidson LHD, and Tummel LHD AR models, respectively.

annulus of outer radius 3.168 mm[35] with a thickness of 500 µm[24]. Figure 6 shows the ratio of electrical conductivity with AR to electrical conductivity without AR for a subset of QLMD 29373.[28] Notice the densities are approximately four orders of magnitude smaller than solid aluminum density ($2.7\,\text{g}\,\text{cm}^{-3}$). At low densities AR can reduce the collisionally based conductivity by more than ten orders of magnitude. The lower-hybrid drift models (Davidson LHD and Tummel LHD) show the largest reduction of conductivity given the modestly large current density ($1.8 \times 10^{11}\,\text{A}\,\text{m}^{-2}$). As expected, the ion acoustic and Buneman AR models do not significantly change the conductivity until the thermal speed becomes comparable to the sound speed at $T \approx 0.5\,\text{eV}$.

The conductivity and equation of state tables used for hydrogen in this work are QLMD 25271[29] and LEOS 1011[51–53], respectively. Figure 7 shows that incorporating AR effects is relevant only at low densities (under $10^{-4}\text{g}\,\text{cm}^{-3}$) and has a similar maximum reduction in conductivity (10-12 orders of magnitude) as Fig. 6. This provides the justification for the importance of AR in the parasitic vacuum hydrogen plasma for the conditions chosen in Sec. III

Chapter 4

The impact of anomalous resistivity in vacuum contaminant plasmas on the electrothermal instability

The impact of anomalous resistivity in vacuum contaminant plasmas on the electrothermal instability

R. L. Masti[a,b], W. A. Farmer[b], B. Srinivasan[a,*]

[a] *Virginia Polytechnic Institute and State University, Blacksburg, VA 24060, USA*
[b] *Lawrence Livermore National Laboratory, Livermore, CA 94550, USA*

Abstract

This manuscript presents an assessment of the electrothermal instability (ETI) in the presence of anomalous resistivity (AR) in vacuum contaminant plasmas (VCP) when applied to a magnetized liner inertial fusion (MagLIF)-like load. Pulsed-power driven dielectrically coated metallic liners, like in MagLIF, experience the current-driven electrothermal instability which occurs when a material's resistivity changes with temperature and is subject to ohmic heating. Large scale pulsed-power facilities that use magnetically insulated transmission lines (MITL) have been shown to generate low-density plasma which enters the target chamber and coalesces around the load. The low-density high-temperature vacuum contaminant plasmas (VCP) can parasitically divert current from the load through causing a short in the anode-cathode gap inside the target chamber. Resistive magnetohydrodynamic (MHD) simulations of these VCP experience unphysical runaway ohmic heating due to under predicting the resistivity by using a purely collisional resistivity model. AR provides a physics-based way to address this runaway heating through increasing the resistivity in a proportional way with the drift speed. In this work, 1D simulations probe the effect that AR in VCP has on the magnetic diffusion rate, and 2D simulations show how this effect manifests in the nonlinear striation form of the ETI for a MagLIF-like load. Beryllium and aluminum dielectrically coated liners are used for the 1D and 2D simulations in this work. The 1D simulations show that a VCP causes a delay in the current delivery to the load by upwards of 8 ns at 60 ns into a typical current pulse for an 1×10^7 A scale pulsed-power accelerator. The 2D simulations show the delay observed in the 1D simulations is reduced substantially (4 ns) by 2D turbulence that disrupts the VCP layer early in time. The 2D simulated ETI growth varies across AR models, more so for the beryllium liner than the aluminum liner because the beryllium liner shows an enhanced rate of penetration for the magnetic diffusion wave in comparison to the aluminum liner. The 2D simulations show the bulk dielectric thickness varies across AR models with the Davidson AR model being the largest and the Buneman AR model being the smallest, and in connection with the thickness the Rayleigh-Taylor bubble-spike distances varies correspondingly.

Keywords: electrothermal instability, MagLIF, anomalous resistivity, contaminant plasmas, magnetic diffusion wave

1. Introduction

There is an extensive effort in the pulsed-power high energy density community to understand the impact of vacuum contaminant plasmas (VCP) on current delivery[1, 2]. These conducting VCP can parasitically divert current away from the load. In resistive magnetohydrodynamic (MHD) simulations, the parasitic current in these plasmas induces runaway heating, further diverting the current from the load when a classical resistivity model is used for the contaminant plasma[3]. The resulting runaway heating causes resistive-MHD simulations to diverge from the experimentally observed current. A resolution to this discrepancy is by including anomalous resistivity, which locally increases the resistivity based on local quantities outside of density and temperature such as magnetic field, current density, and effective ionization level. In simulations of VCP, including AR effects dynamically changes the resistivity which diverts current back into the load through a physics-based method. Altering the current delivery to the load should affect the evolution of the current-driven electrothermal instability (ETI)[4, 5, 6] which is present in all HED pulsed-power configurations[7, 8, 5].

In solid-density metallic loads the resistivity increases with temperature making them susceptible to the striation form of ETI[5]. Although AR is shown not to significantly influence the striation form of ETI directly[9], it may influence the striation form of ETI indirectly. Specifically, by altering the current delivery to the load through AR in VCP the striation ETI in solid-density metallic loads should change, but this is found not to be the case in Section 3. Dielectric coatings mitigate ETI growth in both simulations[10] and experiments[7] of pulsed-power driven solid metal loads. A dielectric coating acts as a

*Corresponding Author
Email addresses: rlm7819@vt.edu (R. L. Masti), srinbhu@vt.edu (B. Srinivasan)

tamper which inhibits mode growth as the surface of the solid-metallic load expands from ohmic heating into the dielectric. One fusion concept that suffers from striation ETI is the magnetized liner inertial fusion (MagLIF) concept that involves imploding a dielectrically coated liner onto a laser-induced pre-magnetized deuterium and tritium fuel[11, 12]. This work explores the impact AR has on ETI growth for a MagLIF-like configuration following Sinars et al. [12].

As mentioned previously, AR can address the runaway heating issue encountered in resistive-MHD simulations of current-carrying VCP. This is accomplished through AR enhancing magnetic diffusion thereby reducing ohmic heating in these weakly collisional plasmas. This enhancement of magnetic diffusion arises from AR increasing a collisionally-based resistivity by incorporating micro-turbulent effects, which are fundamentally driven by plasma instabilities. An example of a plasma instability that drives collisionless micro-turbulence is the Buneman instability[13, 14, 15, 9]. The origin of AR models stems from observations of enhanced magnetic diffusion in high-temperature plasmas present in both theta pinch plasmas and screw pinch plasmas[16, 17, 18, 19, 20] as well as laboratory generated plasmas[21, 22, 23, 24, 25, 26]. These observations sparked the development of reduced models that approximate the effect of micro-turbulent plasma instabilities on material conductivity[13, 27, 28, 29]. This study applies these reduced models to assess the indirect impact it has on the simulated current delivery and the possible impact on the subsequent ETI growth for resistive-MHD simulations of a MagLIF-like load.

This paper is organized as follows. Section 2 presents the impact of AR in VCP on the magnetic diffusion wave ascertained from 1D cylindrical simulations of a MagLIF-like load. Section 3 investigates the striation form of ETI[5, 30] in the presence of a current-carrying VCP through 2D cylindrical simulations of a MagLIF-like load. The key contributions of this paper are three-fold, the first contribution shows a maximum delay of 8 ns between 1D simulations without AR and with AR in a VCP plasma. The second contribution shows that in 2D simulations the presence of a VCP does impact the growth of striation ETI in the beryllium liner simulations and to a lesser extent in the aluminum liner simulations. 2D turbulence disrupts the conducting VCP layer resulting in reduced peak liner current variation observed in 2D compared to 1D. The third contribution shows differences in the deformation of the dielectric when a VCP is present in 2D simulation of striation ETI.

2. Magnetic Diffusion Wave

Many resistive-MHD codes that simulate pulsed-power implosions often supply the current through magnetic flux at the outer radial boundary of a simulation[30]. This magnetic flux is typically determined through Ampere's law and varies with the current pulse. The injection of magnetic field at the outer boundary then diffuses through a highly resistive vacuum and accumulates in the conducting load. This process of diffusing through the vacuum (and dielectric) into and through the load is commonly referred to as the "magnetic diffusion wave". This magnetic diffusion wave is modified when the vacuum is no longer highly resistive, as is the case with these VCP. As a result the magnetic field builds up in the vacuum delaying the magnetic diffusion wave from penetrating into the load. This delay in the magnetic diffusion wave will change the dynamic distribution of current in the load.

Resolving the magnetic diffusion wave through a low-density VCP is challenging due to the restrictions high magnetosonic speeds present for the resistive-MHD equations[31, 30]. The magnetic diffusion wave occurs during the initial phases of the simulated pulse and involves resolving the radial thickness of the load, which for a MagLIF load is approximately 465 µm (aspect ratio of 6)[12]. These small spatial scales in combination with the restrictions from resolving magnetic diffusion in VCP make large 2D and 3D simulations of the magnetic diffusion wave with AR computationally expensive. A 1D simulation provides a computationally inexpensive way to probe the affect of AR on the magnetic diffusion wave. The four AR models used in this study, as described in Masti et al. [9], are the Buneman (BU)[15], Davidson (DA)[27], Tummel (KT)[29], and ion acoustic (IA)[32, 15, 27] AR models.

The density of the vacuum prior to the current pulse is on the order of $1.0 \times 10^{-13}\,\mathrm{g\,cm^{-3}}$[12], which is not computationally feasible to simulate with a fluid-based code. At these densities, the vacuum is weakly collisional causing a breakdown of the continuum approximation. Welch et al. [2] performed kinetic simulations of the magnetically insulated transmission lines (MITL) for a $1.0 \times 10^{7}\,\mathrm{MA}$ accelerator and showed that near the load the plasma would reach $1.0 \times 10^{15}\,\mathrm{cm^{-3}}$ at 1 keV (Section 4). This plasma near the load appears late in time in a current pulse, at approximately 80 ns corresponding to a current of 10 MA[1]. A number density of $1.0 \times 10^{15}\,\mathrm{g\,cm^{-3}}$ corresponds to a mass density on the order of $1.0 \times 10^{-9}\,\mathrm{g\,cm^{-3}}$ (hydrogen plasma) which is difficult to reach in fluid simulations. In this work, a minimum density is set as low as possible whilst allowing for reasonable computation time[1]. The simulations presented in this work use a mass density of $1.0 \times 10^{-7}\,\mathrm{g\,cm^{-3}}$ and a temperature of 100 eV for hydrogen VCP (with a minimum floor density of $1.0 \times 10^{-8}\,\mathrm{g\,cm^{-3}}$. Although this density is much higher than the physically present VCP at early times, it provides the best possible comparison for fluid-based codes at this time.

[1] For reference, the 1D simulations took 1 Day to run and the 2D simulations took over 2 weeks.

2.1. 1D Simulation Setup

A few conducting loads used for MagLIF include liners made of beryllium, aluminum, and copper[11, 33, 5, 34, 12]. Loads that have a dielectric coating produce more stable fuel columns at stagnation[12] and the main dielectric thickness used for MagLIF is 75 µm thick[10, 7, 12]. The dielectric coating acts as a tamper so that when the solid Be or Al expands due to heating it reduces the amplitude of surface roughness perturbations on the ETI growth[10, 7, 12]. Although ETI is a 2D phenomenon, 1D simulations provide insight into the current dynamics when VCP are present.

All simulations shown are done using Ares, a Lawrence Livermore National Laboratory multi-physics radiation-hydrodynamics code[35, 36, 37]. Ares is used to model pulsed-power experiments and has recently been used for a cross-code comparison study of ETI[30]. Additionally, Ares was used to study the impact AR has directly on ETI growth along with a comparison to linear theory[9]. This work explores the indirect impact AR may have on ETI growth in an experimentally-relevant setting based on Sinars et al. [12][2]. The 1D simulations presented here utilize the 2D cylindrical coordinate system in Ares representing the axial direction with a single zone and resolving the radial direction. For this work, Ares solves the resistive-MHD equations using purely Eulerian settings (see Masti et al. [30] for details) with tabulated equations of state (EOS) and tabulated transport coefficients [38, 39, 40, 41, 42, 43]. Radiation is included in the simulations that follow, but is found not to substantially impact the findings herein[37]. Although the Hall term in the induction equation ($\mathbf{J} \times \mathbf{B}$) for a VCP would likely impact the magnetic diffusion wave, this study looks to isolate the impact of AR alone on the induction equation[9].

Fig. 1 represents a schematic of the 1D simulation setup (excluding the perturbation) which is based on Sinars et al. [12] and Masti et al. [30]. The current drive for these simulations is from Eqs. (16) and (17) in Masti et al. [30], and as a reference, 60 ns into the drive corresponds to 7.9 MA. The radial direction uses 1884 uniformly distributed zones and the axial direction is 1 zone. The left and right boundary conditions are reflecting walls, the top boundary condition is an outflow condition, and the bottom boundary is a reflecting wall. The magnetic field is specified at the top boundary based on Ampere's law and requires a resistive buffer for numerical stability, so as these simulations progress, the top most row of zones has vacuum resistivity ($1.0 \times 10^{10}\,\mathrm{m\Omega\,cm}$). The minimum density of these simulations is $1.0 \times 10^{-8}\,\mathrm{g\,cm^{-3}}$ and zones that fall below $1.01 \times 10^{-8}\,\mathrm{g\,cm^{-3}}$ are reassigned with vacuum electrical and thermal conductivities (as shown in Fig. 1)[44]. Mixed zone treatment in Ares, is based on the recommended settings from Farmer et al. [44].

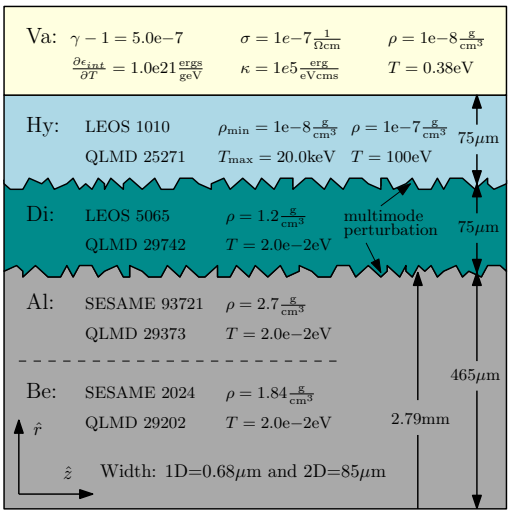

Figure 1: This schematic presents the simulation setup for both the 1D simulations (without perturbations) and the 2D simulations (with perturbations). VA, HY, DI, Al, Be, represent the vacuum region, hydrogen region, dielectric region, aluminum liner region, beryllium liner region, respectively. Each region displays the corresponding initial conditions (ρ is mass density, and T is temperature), EOS, and transport coefficients for this study. Besides the vacuum region being represented by an ideal gas EOS (γ is the adiabatic index) and constant transport coefficients, all the regions use tabulated EOS and transport coefficients. The tabulated quantities used originate from the LEOS database[38, 39, 40] and the SESAME database[41, 42, 43].

2.2. 1D Simulation Results

The impact of AR on the magnetic diffusion wave is diagnosed through its manifestation in the current density as a function of time. Fig. 2 presents the current density of the 1D lineouts at 60 ns for a few configurations involving a change of liner material and with and without the presence of the VCP. The top and bottom rows correspond to runs with an aluminum liner and beryllium liner, respectively, and the left column represents when a VCP is present and the right column when a VCP is absent. The effectiveness of an AR model depends heavily on the drift speed which is a function of current density and mass density as well as the local electron-ion collision time[3]. Without a low-density conducting VCP the effect of AR on the magnetic diffusion wave is negligble and results in no variation of the current density as shown in the right column of Fig. 2. Additionally, the KT, DA, and IA AR models are qualitatively close to the profile without a VCP present, specifically, in the location of the current density peak in the liner (0.265 µm for aluminum and 0.257 µm for beryllium at 60 ns).

The left column of Fig. 2 shows a substantial temporal variation in the current density between the different AR models used and not used. Although the temporal variation is noticeable inside the liner, the qualitative variation inside the liner is not noticeable, and is reasoned through

[2] All dimensions are gathered from the MagLIF section of Sinars et al. [12]

[3] Shorter collision times reduce the impact of AR[9]

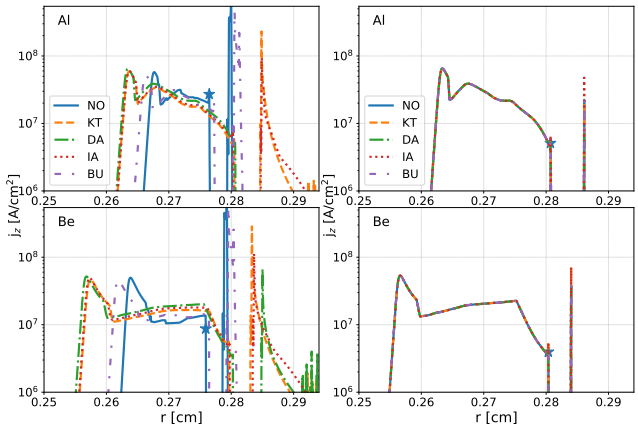

Figure 2: Log j_z as a function of radius is presented at 60 ns for when a hydrogen VCP is present (left column) and absent (right column). The top row corresponds to the simulations using an aluminum and the bottom row corresponds to the simulations using a beryllium liner. Each plot has 5 different lines which are labeled as NO, KT, DA, IA, and BU, which represent no AR model and Tummel, Davidson, ion acoustic, and Buneman, AR models, respectively[9]. The star indicates the location of the transition from liner to dielectric (note for some plots this lies below the minimum j_z shown).

there being no change in the liner and dielectric material between the simulations. The impact of AR on the qualitative behavior of these simulations is apparent in the outer radial regions where there exists ablated dielectric material that is low-density and conducting. The current density profiles in this outer region vary greatly between the AR models with the BU AR model most closely resembling the profile without AR. The KT, DA, and IA AR models show significant reduction in the current density present in the outer region near 0.28 cm.

The AR impacts the magnetic diffusion wave by reducing the delay a VCP would cause on the diffusion through the vacuum (and dielectric) and into the liner. The lower-hybrid drift based AR models, DA and TU, significantly increase the diffusion rate through the vacuum to the point that the inner liner current peak location closely resembles the location in the simulations where a VCP is absent (right column of Fig. 2). In addition to the lower-hybrid drift based AR models, the IA AR model also shows a significant increase in the diffusion rate. The KT, DA, and IA AR model simulations have penetrated approximately 50 µm farther than the simulation without AR (NO). This increase in penetration distance of the magnetic field is temporally correlated and corresponds to approximately a 8 ns reduction in the delay between the KT, DA, and IA AR models (orange, green and red lines), and without an AR model (blue line). The BU AR model (purple line) corresponds to approximately a 4 ns reduction which is half the delay reduction observed from the other AR models. Qualitatively inside the liner the KT, DA, and IA AR models closely resemble the case where a VCP is absent with similar penetration distances. These temporal delays are the same between both the aluminum liner simulations and the beryllium liner simulations which is explained by noting that AR only impacts the VCP[4].

3. Electrothermal Instability

The striation form of ETI occurs when the resistivity of a material increases with temperature and is subjected to ohmic heating[5]. This instability occurs in all pulsed-power fusion concepts that involve solid density metallic liners or wires (e.g. MagLIF). Section 2 shows that a VCP can alter the current delivery as a function of time which should manifest into a variation in ETI growth. This section shows that although the VCP delays the magnetic diffusion wave in the 1D cylindrical resistive-MHD simulations, in the 2D cylindrical resistive-MHD simulations the magnetic diffusion wave is not as significantly altered. The 2D striation ETI simulations show there is little variation across AR models for the aluminum liner and a larger variation for the beryllium liner. The main similarity between the 1D and 2D simulations is in the impact AR has on the peak current densities in the liners which varies across the different AR models.

3.1. 2D Simulation Setup

Figure 1 presents the setup of the ETI simulations in this work, which involve a perturbed liner-dielectric interface and a perturbed dielectric-hydrogen interface (unlike the 1D simulations). The form of the perturbation at the liner-dielectric interface follows Masti et al. [30] which is

$$\delta_{\mathrm{LI-DI}} = \frac{1}{32} A \sum_{m=1}^{m=32} \beta_m \cos\left[2\pi\left(\frac{m\cdot x}{\lambda_{max}} + \beta_m\right)\right] , \quad (1)$$

where A is the amplitude of the perturbation (12 µm), β is a random number from 0 to 1, and $\lambda_{max} = 200\ \mu m$ is the maximum wavelength associated with the lowest mode (see Appendix A for the coefficients used). The dielectric-hydrogen interface uses the multi-mode perturbation form of

$$\delta_{\mathrm{DI-HY}} = \frac{1}{32} A \sum_{m=1}^{m=32} \beta_m \sin\left[2\pi\left(\frac{m\cdot x}{\lambda_{max}} + \beta_m\right)\right] , \quad (2)$$

with the same β and λ_{max} as Eq. (1), but with a smaller amplitude ($A = 6$ µm). Although not shown here, the perturbation of the dielectric-hydrogen interface does not impact the growth as the wavelength and amplitude are varied. The perturbation of the perturbed dielectric-hydrogen interface is estimated from the initial radiographs in Peterson et al. [10].

Outside of the perturbed surfaces, the 2D simulations differ from the 1D simulations in the axial width and in the resolution. The 2D simulations use an axial width of

[4] AR is inversely proportional to the mass density so at higher density, i.e. collisionality, AR is not as impactful

85 µm with a axial resolution of 256 zones[30], and the same radial length as the 1D simulations except for a 1564 zone radial resolution. The 1564 zone radial resolution and the 256 axial resolution are chosen because they result in square zones of size 0.27 µm. As mentioned in Section 2, it is computationally intensive to resolve low-density plasmas at small spatial scales hence a lower radial resolution was chosen for the expensive 2D simulations.

3.2. 2D Simulation Results

The results from Section 2 suggest a large variation in the ETI growth observed across the different models, but this is not qualitatively observed in the 2D simulations. Figure 3 presents a frame of the current density across a subsection of the domain at 60 ns for both the aluminum (top row) and beryllium (bottom row) liners. Figure 4 presents the corresponding plot of density at the same instance in time. Comparing Fig 2 to Fig 3, the 1D result for the aluminum liner case does not show the same delay separation of the peak internal liner current density as the beryllium liner case. Although the magnitude of peak current density in the liner varies across the columns in the top row of Fig 3, the location of the peak in the liner is nearly identical across the different AR models. There is some underlying physical mechanism that in 2D, would allow for reduced current density peak separation across AR models for aluminum and not for beryllium. A few hypotheses to explain this are that the aluminum EOS used has a significantly different physical basis than the beryllium EOS used; the initial aluminum electrical conductivity is higher than the initial beryllium conductivity which creates a larger initial resistivity gradient[30]; the sensitivity of the aluminum resistivity to density is larger than the sensitivity of beryllium resistivity to density. For brevity, NO, KT, DA, IA, and BU, denote the simulations which used NO, KT, DA, IA, and BU AR models, respectively.

The current density plots for an aluminum liner as shown in the top row of Fig. 3 show a variation in peak current density inside the liner. The NO, KT, DA, IA, and BU simulated peak aluminum liner current density are $1.28\,\mathrm{A\,cm^{-2}}$, $1.29\times10^{8}\,\mathrm{A\,cm^{-2}}$, $1.34\times10^{8}\,\mathrm{A\,cm^{-2}}$, $1.31\times10^{8}\,\mathrm{A\,cm^{-2}}$, and $1.30\times10^{8}\,\mathrm{A\,cm^{-2}}$, respectively. For the beryllium liner case (bottom row), the peak simulated liner current density for NO, KT, DA, IA, and BU, are $8.84\times10^{7}\,\mathrm{A\,cm^{-2}}$, $9.42\times10^{7}\,\mathrm{A\,cm^{-2}}$, $9.66\times10^{7}\,\mathrm{A\,cm^{-2}}$, $9.47\times10^{7}\,\mathrm{A\,cm^{-2}}$, and $9.18\times10^{7}\,\mathrm{A\,cm^{-2}}$, respectively. All of the current densities in the aluminum liner case are greater than the beryllium liner case and this is mainly due to higher conductivities for aluminum at the location of the peak. The separation or delay across the different AR models is greater for the beryllium liner simulations than it is for aluminum and this is also seen in Fig. 2 but not to the same extent. This suggests that the 2D turbulence in the vacuum region causes enhanced magnetic diffusion through the vacuum which implies faster accumulation in the liner. This explains the reduction in variation across peak liner current density locations for the different AR models in 2D (Fig. 3) in comparison to the separation in 1D (Fig. 2). Figure 3 also highlights the impact that each AR model has on limiting the runaway current in the vacuum, with the DA model corresponding to the most effective vacuum current limiter. The weakest AR model is BU which shows nearly no variation in peak vacuum current density in comparison to the NO simulation.

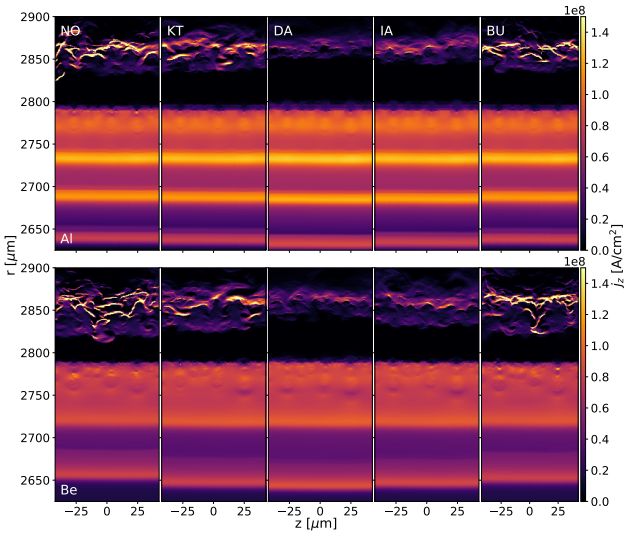

Figure 3: Current density plots of the ETI simulation outlined in Section 3 are shown at 60 ns for different configurations. The top and bottom rows correspond to ETI simulations using an aluminum and beryllium liner, respectively. The columns represent simulations using different AR implementations. NO, KT, DA, IA, and BU represent the use of no AR model, Tummel AR model, Davidson AR model, and Buneman AR model, respectively[9].

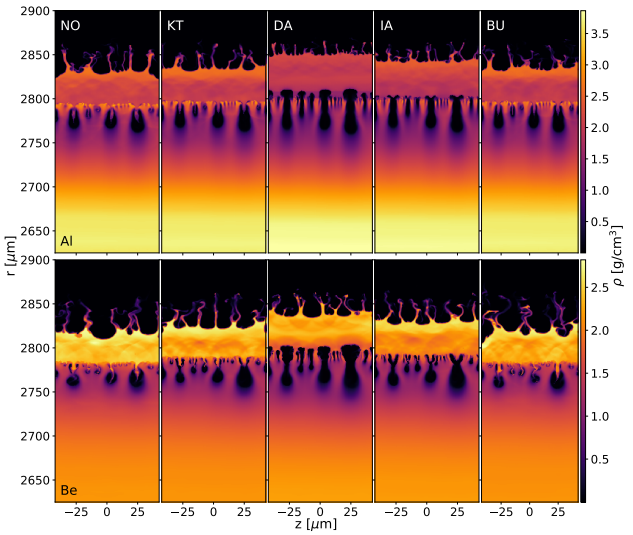

Figure 4: Density plots of the same simulations as described in Fig. 3.

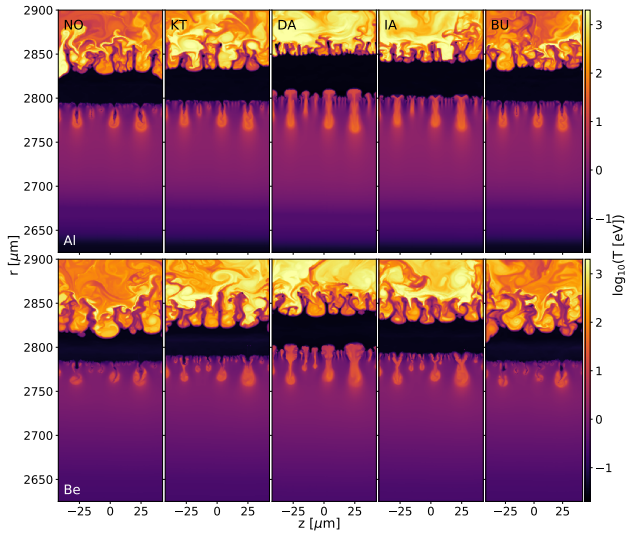

Figure 5: Temperature is plotted on a logarithmic scale for the same simulations described in Fig. 3.

Figure 4 presents mass density plots at 60 ns for the aluminum (top row) and beryllium (bottom row) liners using different AR models (columns). Since the separation across the aluminum peak liner current density does not vary greatly, there are no qualitatively observable differences across the AR models in ETI growth. The beryllium liner does have a larger variation in the location of peak current density in the liner which manifests as differences in the observed ETI growth. For the beryllium liner, the spot sizes, the size of the density void created from nonlinear ETI growth[30], between the BU and NO AR models are nearly the same and both are significantly smaller than the spot sizes of the KT, DA, and IA AR models. The spatial variation in peak current location due to the delay in the magnetic diffusion wave is the cause for the qualitative differences in ETI growth observed across the bottom row of Fig. 4. The outer dielectric interface shows significant variation in mode growth across the different AR models for both the beryllium and aluminum liners. Comparing Fig. 4 to Fig. 3 the IA and DA are the most effective at reducing the current or magnetic field accumulation in the low density outer region and forcing it to lower radii, KT is the next most effective, with BU and NO following thereafter. The Rayleigh-Taylor instability occurs when a light fluid supporting a heavier fluid under the influence of a gravitational acceleration is perturbed, and is applicable to the VCP-dielectric interface. The more effective the AR model is at reducing the current in the VCP the smaller the outer dielectric RT instability structure is. The peak bubble-spike distance for the developing RT instability in order of least to most is DA, IA, KT, BU, and NO AR models corresponds to the same order as observed in the peak internal liner current location in Fig. 2 for both aluminum and beryllium liners. The dielectric does induce mitigated ETI growth when comparing with Figs. 7 and 10 of Masti et al. [30] keeping in consideration the differences of EOS used.

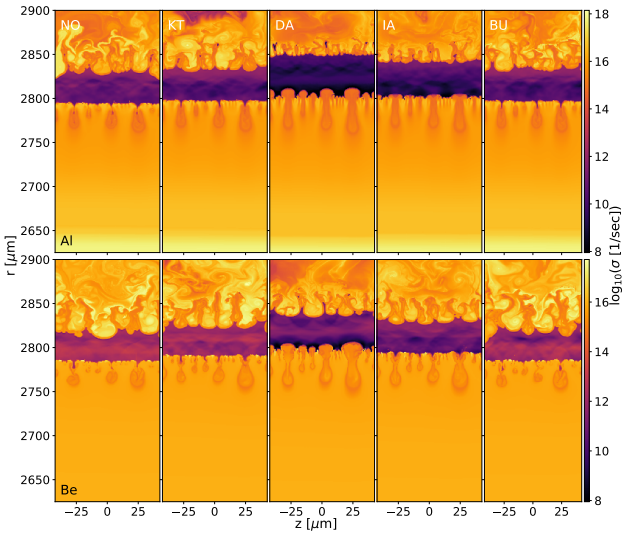

Figure 6: Electrical conductivity (including AR) is plotted on a logarithmic scale for the same simulation set described in Fig. 3.

The temperature at 60 ns is displayed in Fig. 5 where a log scale is used to highlight the low density plasma that surrounds the dielectric. The material in the upper region of these plots is primarily the dielectric where the surface of the dielectric has ablated into a low density conducting material which is subjected to ohmic heating, and is why the outer region is so hot in comparison to the ETI spots. The differences across AR models shows the peak temperature is in the DA AR model in Fig. 5. The peak temperature for DA is understood through Fig. 4 where the DA AR model shows the lowest mass density in the VCP. The peak temperature corresponding to the smallest density of the DA AR model is observed in both the beryllium and aluminum liner simulations. The bulk thickness of the dielectric varies across the AR models and is the same in both the aluminum and beryllium liner simulations and is shown in Fig. 5. Based on these simulations, the variation in bulk thickness of the dielectric would provide a useful measurement from an experiment to determine the most physically accurate AR model. Note that the bulk thickness does increase in variation across the different AR models over time.

Figure 6 displays the electrical conductivity for the same simulations shown in Fig. 3-5. In the vacuum region the density is on the order of $1.0 \times 10^{-5}\,\mathrm{g\,cm^{-3}}$ nearest to the dielectric with a corresponding temperature around 1 keV, and at this density and temperature the electrical resistivity is well represented by the Spitzer form of resistivity which has a stronger temperature dependence than density dependence[45]. The opposite is said for the liner material which is a stronger function of density[5]. This explains

the correlation of high temperature to high electrical conductivity in the low density region near the dielectric and the correlation of high density to high electrical conductivity in the liner region through comparing Fig. 5 and Fig. 4 to Fig. 6, respectively. The dielectric has a small conducting layer that varies in size based on the AR model, and is the most resistive portion of the simulation when excluding the outer most vacuum resistivity buffer. This dielectric conducting layer is due to thermal diffusion from the current carrying low density surrounding material into the bulk dielectric material causing it to heat creating a density and temperature separation inside the dielectric. The size of this layer is determined from the magnitude of current in the low density material which is highest for the NO AR model case and the lowest for the DA AR model case. Note the dielectric warm conducting layer thickness is the same for both the beryllium and aluminum simulations, as this is an interplay between the dielectric and VCP.

4. Conclusions

This work investigates striation ETI when AR is present in a VCP that is surrounding a pulsed-power-driven dielectrically-coated solid metal liner for a typical MagLIF-like load based on Sinars et al. [12]. There are four AR models chosen for the comparisons which are the Tummel, Davidson, ion acoustic, and Buneman AR models[9], and they are applied in a VCP surrounding dielectrically coated aluminum and beryllium liners[12]. First, 1D fluid simulations are used to evaluate the impact a VCP would have on the magnetic diffusion wave keeping in consideration that the vacuum density is pushed as low as feasibly possible for present computational means. 2D simulations provide striation ETI simulations and evaluate the effect a VCP, early in time, has on ETI growth. The simulations in 1D and 2D follow the setup described in Fig. 1, and the conditions used for the VCP are as close to the values reported by Welch et al. [2] as possible for density and temperature (see Section 2).

Section 2 presents the impact of AR on the magnetic diffusion wave in the presence of a VCP using 1D resistive-MHD simulations. The current density is shown to vary greatly between the different choices of AR models which is characterized by a "delay" in the magnetic diffusion wave. The delay is measured at 60 ns to be around a maximum of 8 ns which implies the magnetic field accumulation in the VCP delays the wave by 8 ns. Figure 2 shows this delay and it originates from the temporal difference between liner current density peaks between the left and right plots. The most effective AR model at reducing magnetic field accumulation in the electrically conducting vacuum is the DA AR model followed by the IA, KT, and BU AR models and this is determined by the location of the internal peak liner current compared to the simulations where a VCP is absent. The current in the VCP is substantially different across the different AR models, but the current in the liner varies less than 10 %. Between the beryllium and the aluminum, the beryllium shows the largest spatial variation in the current peaks but still has nearly the same delay as the aluminum case.

Section 3 explores how the delay impacts striation ETI growth through the use of 2D resistve-MHD ETI simulations. Unlike in 1D, the 2D simulations allow for disruption of the VCP layer early in time sourced through the dielectric-hydrogen interface perturbation. The disruption of the VCP allows for enhanced magnetic diffusion meaning the delay is slightly smaller in the 2D simulations than the 1D simulations when comparing Fig. 2 to Fig. 3. The rationale follows the same approach as Yu et al. [46] where the instead of a resistive inclusion there is a conducting inclusion and the fluid is magnetic field instead of current density. Although there were observable differences in the ETI growth for the beryllium liner (see Fig. 4), the main impact of the VCP comes from the structure and dynamics of the outer dielectric interface. The VCP is shown to cause ablation of the dielectric surface (see Fig. 5) leading to a current-carrying, low density, high temperature vacuum plasma of dielectric material. The outer surface of the dielectric is shown to develop RT-like bubbles and spikes for high Atwood number. A dielectric conducting layer develops inside the dielectric, and is sourced from thermal conduction of the low density vacuum dielectric plasma to the bulk dielectric material. This warm dielectric conducting layer has an electrical conductivity that is many orders of magnitude smaller than the electrical conductivity in the liner or vacuum themselves (excluding the resistive buffer in the axial layer at outermost radial zone). An experiment that would measure this variation in dielectric thickness can help determine the physical correctness and accuracy for the use of AR models in these regimes.

Acknowledgements

This work was supported through the Lawrence Livermore National Laboratory Weapons and Complex Integration (LLNL WCI) High Energy Density Fellowship, and through the US Department of Energy under grant DE-NA0003881.

A portion of this work was performed under the auspices of the U.S. Department of Energy by Lawrence Livermore National Laboratory under Contract DE-AC52-07NA27344. This document was prepared as an account of work sponsored by an agency of the United States government. Neither the United States government nor Lawrence Livermore National Security, LLC, nor any of their employees makes any warranty, expressed or implied, or assumes any legal liability or responsibility for the accuracy, completeness, or usefulness of any information, apparatus, product, or process disclosed, or represents that its use would not infringe privately owned rights. Reference herein to any specific commercial product, process, or service by trade name, trademark, manufacturer, or

otherwise does not necessarily constitute or imply its endorsement, recommendation, or favoring by the United States government or Lawrence Livermore National Security, LLC. The views and opinions of authors expressed herein do not necessarily state or reflect those of the United States government or Lawrence Livermore National Security, LLC, and shall not be used for advertising or product endorsement purposes.

This document has been approved for release under the release identifier LLNL-JRNL-821711.

Data Availability

The data that support the findings of this study are available from the corresponding author upon reasonable request.

References

[1] M. Gomez, R. Gilgenbach, M. Cuneo, C. Jennings, R. McBride, E. Waisman, B. Hutsel, W. Stygar, D. Rose, Y. Maron, Experimental study of current loss and plasma formation in the z machine post-hole convolute, Physical Review Accelerators and Beams 20 (2017) 010401.

[2] D. Welch, N. Bennett, T. Genoni, D. Rose, C. Thoma, C. Miller, W. Stygar, Electrode contaminant plasma effects in 1.0e7-a z pinch accelerators, Physical Review Accelerators and Beams 22 (2019) 070401.

[3] C. Seyler, M. R. Martin, N. Hamlin, Helical instability in maglif due to axial flux compression by low-density plasma, Physics of Plasmas 25 (2018) 062711.

[4] V. I. Oreshkin, Thermal instability during an electrical wire explosion, Physics of Plasmas 15 (2008) 092103.

[5] K. J. Peterson, D. B. Sinars, E. P. Yu, M. C. Herrmann, M. E. Cuneo, S. A. Slutz, I. C. Smith, B. W. Atherton, M. D. Knudson, C. Nakhleh, Electrothermal instability growth in magnetically driven pulsed power liners, Physics of Plasmas 19 (2012) 092701.

[6] D. Ryutov, M. S. Derzon, M. K. Matzen, The physics of fast z pinches, Reviews of Modern Physics 72 (2000) 167.

[7] T. J. Awe, Electrothermal Instability Evolution on Z-Pinch Rods and Imploding Liners Pulsed with Intense Current., Technical Report, Sandia National Lab.(SNL-NM), Albuquerque, NM (United States), 2016.

[8] T. M. Hutchinson, T. J. Awe, B. Bauer, K. Yates, E. P. Yu, W. G. Yelton, S. Fuelling, Experimental observation of the stratified electrothermal instability on aluminum with thickness greater than a skin depth, Physical Review E 97 (2018) 053208.

[9] R. L. Masti, C. L. Ellison, W. A. Farmer, K. Tummel, B. Srinivasan, The effect of anomalous resistivity on the fast electrothermal instability, In review (to be published in 2021).

[10] K. J. Peterson, T. J. Awe, P. Y. Edmund, D. B. Sinars, E. S. Field, M. E. Cuneo, M. C. Herrmann, M. Savage, D. Schroen, K. Tomlinson, et al., Electrothermal instability mitigation by using thick dielectric coatings on magnetically imploded conductors, Physical review letters 112 (2014) 135002.

[11] S. Slutz, M. Herrmann, R. Vesey, A. Sefkow, D. Sinars, D. Rovang, K. Peterson, M. Cuneo, Pulsed-power-driven cylindrical liner implosions of laser preheated fuel magnetized with an axial field, Physics of Plasmas 17 (2010) 056303.

[12] D. Sinars, M. Sweeney, C. Alexander, D. Ampleford, T. Ao, J. Apruzese, C. Aragon, D. Armstrong, K. Austin, T. Awe, et al., Review of pulsed power-driven high energy density physics research on z at sandia, Physics of Plasmas 27 (2020) 070501.

[13] K. Papadopoulos, A review of anomalous resistivity for the ionosphere, Reviews of Geophysics 15 (1977) 113–127.

[14] O. Buneman, Transverse plasma waves and plasma vortices, Physical Review 112 (1958) 1504.

[15] P. C. Liewer, N. Krall, Self-consistent approach to anomalous resistivity applied to theta pinch experiments, The Physics of Fluids 16 (1973) 1953–1963.

[16] D. Baker, L. Burkhardt, J. Dimarco, P. Forman, A. Haberstich, H. Karr, L. Mann, J. Phillips, A. Schofield, Z-pinch experiments with shock heating, in: Plasma Physics and Controlled Nuclear Fusion Research 1971. Vol. I. Proceedings of the Fourth International Conference on Plasma Physics and Controlled Nuclear Fusion Research, 1971.

[17] A. DeSilva, W. Dove, I. Spalding, G. Goldenbaum, Experimental study of the magnetic piston-shock wave problem in a collisionless plasma, The Physics of Fluids 14 (1971) 42–51.

[18] N. Bretz, A. DeSilva, Turbulence spectrum observed in a collision-free θ-pinch plasma by c o 2 laser scattering, Physical Review Letters 32 (1974) 138.

[19] Y. Maron, E. Sarid, O. Zahavi, L. Perelmutter, M. Sarfaty, Particle-velocity distribution and expansion of a surface-flashover plasma in the presence of magnetic fields, Physical Review A 39 (1989) 5842.

[20] K. McKenna, R. Kristal, K. Thomas, Measurements of plasma density distribution and current-sheath in the implosion phase of a theta-pinch discharge, Physical Review Letters 32 (1974) 409.

[21] A. Divin, Y. V. Khotyaintsev, A. Vaivads, M. André, S. Markidis, G. Lapenta, Evolution of the lower hybrid drift instability at reconnection jet front, Journal of Geophysical Research: Space Physics 120 (2015) 2675–2690.

[22] M. Zhou, H. Li, X. Deng, S. Huang, Y. Pang, Z. Yuan, X. Xu, R. Tang, Characteristic distribution and possible roles of waves around the lower hybrid frequency in the magnetotail reconnection region, Journal of Geophysical Research: Space Physics 119 (2014) 8228–8242.

[23] R. Torbert, J. Burch, B. Giles, D. Gershman, C. Pollock, J. Dorelli, L. Avanov, M. Argall, J. Shuster, R. Strangeway, et al., Estimates of terms in ohm's law during an encounter with an electron diffusion region, Geophysical Research Letters 43 (2016) 5918–5925.

[24] S. C. Hsu, T. Carter, G. Fiksel, H. Ji, R. Kulsrud, M. Yamada, Experimental study of ion heating and acceleration during magnetic reconnection, Physics of Plasmas 8 (2001) 1916–1928.

[25] R. Commisso, H. R. Griem, Observation of collisionless heating and thermalization of ions in a theta pinch, Physical Review Letters 36 (1976) 1038.

[26] H. Ji, S. Terry, M. Yamada, R. Kulsrud, A. Kuritsyn, Y. Ren, Electromagnetic fluctuations during fast reconnection in a laboratory plasma, Physical review letters 92 (2004) 115001.

[27] R. Davidson, N. Krall, Anomalous transport in high-temperature plasmas with applications to solenoidal fusion systems, Nuclear Fusion 17 (1977) 1313.

[28] S. P. Gary, Wave-particle transport from electrostatic instabilities, The Physics of Fluids 23 (1980) 1193–1204.

[29] K. Tummel, C. Ellison, W. Farmer, J. Hammer, J. Parker, K. Lechien, Kinetic simulations of anomalous resistivity in high-temperature current carrying plasmas, Physics of Plasmas 27 (2020) 092306.

[30] R. Masti, C. Ellison, J. King, P. Stoltz, B. Srinivasan, Cross-code verification and sensitivity analysis to effectively model the electrothermal instability, High Energy Density Physics 38 (2021) 100925.

[31] J. R. King, R. Masti, B. Srinivasan, K. Beckwith, Multidimensional tests of a finite-volume solver for mhd with a real-gas equation of state, IEEE Transactions on Plasma Science 48 (2020) 902–913.

[32] A. Galeev, R. Sagdeev, Theory of neoclassical diffusion, RvPP 7 (1979) 257.

[33] D. B. Sinars, et al., Measurements of magneto-rayleigh-taylor instability growth during the implo-

sion of initially solid metal liners, Physics of Plasmas 18 (2011) 056301. URL: http://aip.scitation.org/doi/abs/10.1063/1.3560911. doi:10.1063/1.3560911. arXiv:http://aip.scitation.org/doi/pdf/10.1063/1.3560911.
[34] K. J. Peterson, E. P. Yu, D. B. Sinars, M. E. Cuneo, S. A. Slutz, J. M. Koning, M. M. Marinak, C. Nakhleh, M. C. Herrmann, Simulations of electrothermal instability growth in solid aluminum rods, Physics of Plasmas 20 (2013) 056305.
[35] B. E. Morgan, J. A. Greenough, Large-eddy and unsteady rans simulations of a shock-accelerated heavy gas cylinder, Shock Waves 26 (2016) 355–383. URL: https://doi.org/10.1007/s00193-015-0566-3. doi:10.1007/s00193-015-0566-3.
[36] C. L. Ellison, H. D. Whitley, C. R. D. Brown, S. R. Copeland, W. J. Garbett, H. P. Le, M. B. Schneider, Z. B. Walters, H. Chen, J. I. Castor, R. S. Craxton, M. Gatu Johnson, E. M. Garcia, F. R. Graziani, G. E. Kemp, C. M. Krauland, P. W. McKenty, B. Lahmann, J. E. Pino, M. S. Rubery, H. A. Scott, R. Shepherd, H. Sio, Development and modeling of a polar-direct-drive exploding pusher platform at the national ignition facility, Physics of Plasmas 25 (2018) 072710. URL: https://doi.org/10.1063/1.5025724. doi:10.1063/1.5025724. arXiv:https://doi.org/10.1063/1.5025724.
[37] J. D. Bender, O. Schilling, K. S. Raman, R. A. Managan, B. J. Olson, S. R. Copeland, C. L. Ellison, D. J. Erskine, C. M. Huntington, B. E. Morgan, et al., Simulation and flow physics of a shocked and reshocked high-energy-density mixing layer, Journal of Fluid Mechanics 915 (2021).
[38] R. More, K. Warren, D. Young, G. Zimmerman, A new quotidian equation of state (qeos) for hot dense matter, The Physics of fluids 31 (1988) 3059–3078.
[39] D. A. Young, E. M. Corey, A new global equation of state model for hot, dense matter, Journal of applied physics 78 (1995) 3748–3755.
[40] F. N. Fritsch, The LEOS Interpolation Package, Technical Report, Lawrence Livermore National Lab., CA (US), 2003.
[41] M. P. Desjarlais, Practical improvements to the lee-more conductivity near the metal-insulator transition, Contributions to Plasma Physics 41 (2001) 267–270.
[42] M. Desjarlais, J. Kress, L. Collins, Electrical conductivity for warm, dense aluminum plasmas and liquids, Physical Review E 66 (2002) 025401.
[43] T. Sjostrom, S. Crockett, S. Rudin, Multiphase aluminum equations of state via density functional theory, Physical Review B 94 (2016) 144101.
[44] W. A. Farmer, C. L. Ellison, K. R. LeChein, C. E. Myers, K. Ruman, K. Tummel, J. H. Hammer, R. L. Masti, C. Jennings, M. Hess, Magnetohydrodynamics modeling of near-target vacuum plasmas in pulsed power simulations, In review (to be published in 2021).
[45] L. Spitzer, Physics of Fully Ionized Gases, 1956.
[46] E. P. Yu, T. J. Awe, K. R. Cochrane, K. C. Yates, T. M. Hutchinson, K. J. Peterson, B. S. Bauer, Use of hydrodynamic theory to estimate electrical current redistribution in metals, Physics of Plasmas 27 (2020) 052703.

Appendix A. Coefficients of the multimode perturbation

mode (i)	β_i
1	0.883494
2	0.313251
3	0.139670
4	0.438109
5	0.642904
6	0.176107
7	0.856669
8	0.630685
9	0.682887
10	0.941226
11	0.236611
12	0.699510
13	0.440243
14	0.124690
15	0.643533
16	0.018313
17	0.415389
18	0.403712
19	0.122180
20	0.313884
21	0.207358
22	0.915150
23	0.038463
24	0.991615
25	0.755673
26	0.558353
27	0.586421
28	0.896183
29	0.305981
30	0.495188
31	0.476349
32	0.057556

Table A.1: These coefficients are the same as the ones from Masti et al. [30], and are used in Eqs. (1) and (2).

Chapter 5

Conclusions and Future Work

This dissertation's main focus is in the study of ETI with AR. The result of this study features three peer reviewed papers in which various aspects of ETI are investigated. The first paper provides a code comparison of nonlinear ETI simulations including verification tests. The second paper investigates the role of AR on the linear ETI growth. The third paper investigates the indirect role of AR on nonlinear ETI growth for a setup similar to the one used in the first paper. In totality, these three papers describe effective and accurate modeling of ETI simulations, the direct impact of AR on linear ETI, and the indirect impact AR has on nonlinear ETI evolution. The first and third papers study the striation form of ETI, while the second paper studies both but only verifies with the filamentation form of ETI[1].

Chapter 2 uses Ares[1], a multi-physics rad-hydro code developed by LLNL, and USim, a multi-physics code developed by Tech-X[2], to model the important physical aspects relevant to simulating nonlinear ETI growth (see Chapter 2.2 for details about the codes). Chapter 2.3 provides two test cases which investigates the necessary contributions to capturing nonlinear ETI evolution. Specifically, the magnetic diffusion test case (Chapter 2.3.1) determines a code's ability to solve the induction equation, and the linear ETI test case (Chapter 2.3.2) determines how the code couples the magnetic diffusion to the resistive-MHD energy equation. The later case provides a direct comparison to theoretical growth which can be used to obtain convergence information about a code's numerical scheme. With both of the codes verified using these test cases, they are then used to simulate nonlinear ETI growth in Chapter 2.4. The nonlinear ETI simulations are compared qualitatively and quantitatively and are shown to give similar characteristics, but the differences in evaluating the spatial derivative lead to the most stark differences as described in Chapter 2.4. Once compared across USim and Ares, Ares is then used to perform a sensitivity analysis of the nonlinear ETI. Chapter 2.4.2 shows that the nonlinear ETI growth is highly sensitive to EOS, and also highlights the need for high fidelity tabulated EOS interpolation algorithms. Chapter 2.4.3 shows the nonlinear ETI growth sensitivity to vacuum resistivity, which results in guidance on appropriate choices of vacuum resistivity. The optimal vacuum resistivity was found to be approximately 1×10^4 times higher than the initial liner resistivity, as this provides a

[1]These forms of ETI are attributed to the "fast" form which assumes the skin depth is much greater than the current thickness, i.e, no radial variation only azimuthal and axial.

converged[2] result. Lastly, Chapter 2.4.4 presents the sensitivity of nonlinear ETI growth to vacuum density, and shows that it is not sensitive to vacuum density to the extent that it is to vacuum resistivity and EOS.

Chapter 3 presents new linear ETI theory incorporating the added dependence resistivity has on current density when AR is present extending its dependencies beyond just density and temperature. The new linear theory is then verified through filamentation ETI simulations in Ares. Chapter 3.2 presents the derivation of the new linear growth rate from conservation of energy, Ampere's law, Faraday's law, and Ohm's law. The new form is then used to probe the striation and filamentation form of ETI and assess the impact of AR for those configurations. Even without the added dependence of current density, the linear filamentation ETI growth rate increases greatly when AR effects are included, see Chapter 3.2.1. The added dependence is shown to have a stabilizing impact on filamentation ETI growth when AR is included, see Chapter 3.2.2. Chapter 3.2.3 presents the impact of AR on the striation ETI linear growth rate, and is found to not have an impact with the current densities achievable today[3]. The linear growth rate derived in Chapter 3.2 is then verified through simulation in Chapter 3.3. A filamentation ETI growth in a wedge is used for this verification, note the comparison to theory is not as direct as it is for striation linear ETI. The indirectness is due to striation linear ETI having a constant growth rate, while the filamentation ETI growth rate is inherently dynamic due to its dependence on η and j_z. One of the subtle discoveries in Chapter 3.3 comes from the comparison of radiation with and without AR, which shows that radiative cooling does not become dominant until higher temperatures in the 1 keV range for a $1.0 \times 10^{-6}\,\mathrm{g\,cm^{-3}}$ plasma.

Chapter 4 dives into the indirect role of AR in VCP on the striation nonlinear ETI growth. Specifically a dielectric-coated, MagLIF-like liner is simulated with a surrounding VCP using the lowest possible density settings and temperature settings based on Welch et al. [3]. In fluid simulations of pulsed-power implosions the current is driven by setting a magnetic field at the outer boundary which diffuses through the vacuum, dielectric, and accumulates in the liner. In resistive-MHD simulations, this process is not instantaneous which is denoted as the magnetic diffusion wave. Chapter 4.2 shows that the presence of a VCP without AR can delay the magnetic diffusion wave by upwards of 8 ns when the current pulse has reached the 60 ns mark. Three AR models almost entirely remove the delay (Davidson, Tummel, and ion acoustic AR models), and one AR model only partially removes the delay (Buneman AR model). A delay in the magnetic diffusion wave causes the current evolution to change because they are inherently tied through Ampere's law ($\mathbf{J} = \nabla \times \mathbf{B}/\mu_0$ for electrostatic fields), and this subsequently influences nonlinear ETI development. The impact of altering the current evolution is more noticeable for beryllium liners vs aluminum liners. The 2D simulations in Chapter 4.5 show that the delay of the magnetic diffusion wave is significantly

[2]Converged meaning the simulation is identical to a simulation which uses a near infinitely resistive vacuum

[3]With large enough current densities AR can have a prominent role in the striation form of ETI growth ($1.0 \times 10^{14}\,\mathrm{A\,m^{-2}}$).

overpredicted by the 1D simulations in Chapter 4.2. The reduction in the delay is due to 2D turbulence disrupting the VCP layer early in time. The most impactful finding of this chapter is the variation across the dielectric for the different AR models which can provide an avenue for AR validation through experiments.

During this journey many ideas and concepts could not be pursued due to time constraints, some are presented in the sections that follow and others are mentioned briefly here. First, the simulations in Chapter 4 could have used a mass flux source at the outer boundary instead of pre-existing VCP. The density would then be able to ramp up, and in combination with a temperature ramp, provide an even more physically accurate representation of AR in a VCP. Another interesting avenue forward is to investigate metallically coated MagLIF liners instead of dielectrically coated liners, as this would alter the dynamics of the magnetic diffusion wave and provide improved integration with a VCP. Although it was mentioned heavily in Chapter 1 that the axial magnetic field in MagLIF is critical, none of the ETI simulations presented here used an axial magnetic field or assess its impact on ETI which would provide fruitful future work, specifically with AR in 3D. Lastly, one of the main arguments against the use of AR in the pulsed-power HED community is their lack of experimental validation. The next two sections discuss an in depth analysis that would hypothetically address these concerns, the first uses MAGPIE experiments of wire-array explosions[4] and the latter explores gas puff Z-pinches[5, 6].

MAGPIE Experiments

Although the Z-machine was the sole pulsed-power device modeled in this dissertation, many other pulsed-power devices exist. The Mega Ampere Generator for Plasma Implosion Experiments (MAGPIE) at Imperial College London is a pulsed-power machine that can reach 1 MA in 250 ns, and was one of the first pulsed-power machines to observe azimuthal structure in wire-array implosions[7]. Recent experiments on MAGPIE have explored magnetized plasmas[8] and astrophysical plasmas[9] through this wire-array configuration. These university-based accelerators provide valuable open access to HED regimes that would otherwise not be accessible.

Hare et al. [4] performed a wire array explosion, schematic shown in Figure 5.1, near a barrier to drive magnetized turbulence, and observed azimuthal structure when using tungsten wires as shown in Figure 5.2. The origin of the azimuthal structure is unknown, but was not present when aluminum wires were used as shown in Figure 5.3. There are currently three hypotheses as to the origin of the observed structure: a two-stream instability, radiative condensation instability, and the ETI. The plasma at the time of the observed structure is magnetized with a plasma beta of approximately 0.8, which is the ratio of dynamic pressure to magnetic pressure. At this instance in time, the plasma density is $5.0 \times 10^{17}\,\mathrm{cm}^{-3}$ which is ideally suited for the use of AR models, see Chapter 1.6. Masti et al. [10] provides an avenue to address the aforementioned third hypothesis, that with a combination of ETI and AR, the

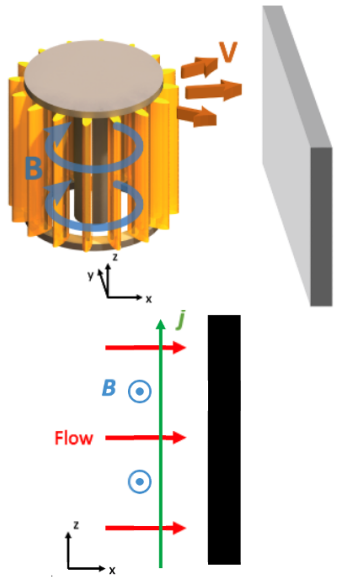

Figure 5.1: Schematic of the MAGPIE wire array experiment for aluminum and tungsten wires[4].

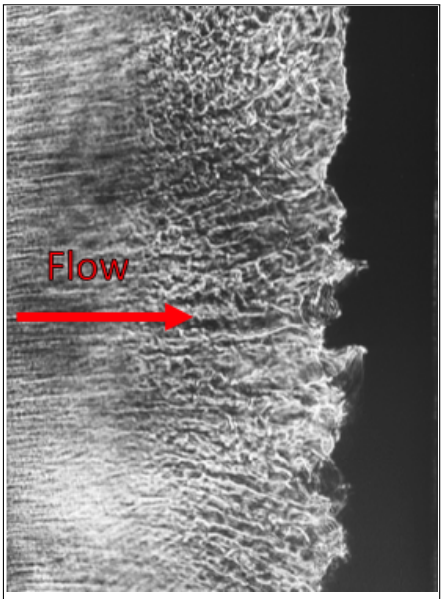

Figure 5.2: Tungsten radiography of the MAGPIE experiment[4] showing the stratified structure.

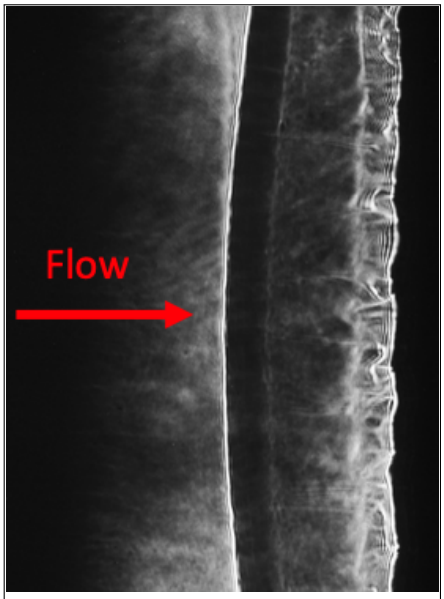

Figure 5.3: Aluminum radiography of the MAGPIE experiment[4] showing absence of structure (does show a reverse shock).

observed striation structure may be explained.

The radiography images in Figures 5.3 and 5.2 are taken in the x-z plane where $\hat{x}$ is directed from the wire array center to the barrier, and $\hat{z}$ is directed in the axial current direction. Figure 5.3 shows striations aligned with a k_z perturbation, this implies the possible presence of striation ETI[11, 12, 13]. Masti et al. [10] shows that the striation form of ETI is insensitive to AR effects for aluminum, which could explain the lack of observed structure from the aluminum radiograph. The same study will be applied to tungsten, and will hopefully validate experimentally the AR models that are being used. The validation would provide confidence in the physics-based applicability of AR which can be an integral part in studying the seeding structure of MagLIF.

Gas-Puff Z-pinch

The work in Chapter 2 utilizes the techniques presented in a semi-analytical model of MagLIF, SAMM[14]. Narkis et al. [6] presents a semi-analytical model for a gas-puff staged Z-pinch. The gas-puff staged Z-pinch, as shown in Figure 5.4, is similar to the MagLIF concept with the main difference being in how the fuel is pre-magnetized. In gas-puff Z-pinches the liner is gaseous instead of the solid metal in MagLIF. A current is driven in the same way

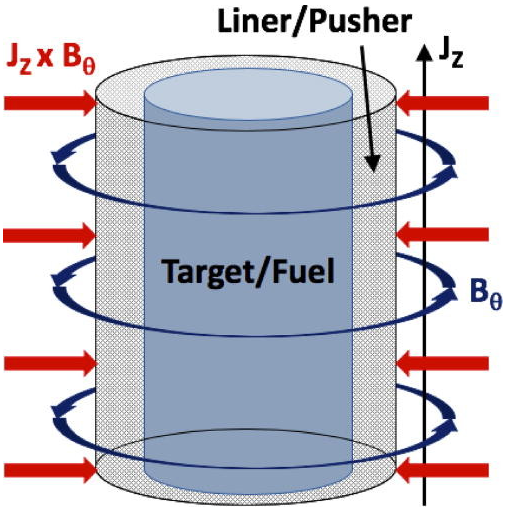

Figure 5.4: This schematic is Figure 1 from Narkis et al. [6] displaying a gas-puff staged Z-pinch.

through this gaseous liner, but the dynamics of the problem change significantly. Because of its low-density, the gaseous liner will accelerate to very high speeds as the current is driven. The large acceleration would push the plasma fuel into a supersonic state which induces a shock front. The shock front then heats the plasma fuel resulting in its magnetization. Although very similar to MagLIF, this concept has a very different setup from a simulation standpoint. Particularly, the gas-puff Z-pinch simulations require separate electron and ion temperatures, anisotropic transport coefficients, and radiation physics to name a few.

The densities proposed for the gas-puff staged Z-pinch are $1.0 \times 10^{17}\,\mathrm{cm}^{-3}$ which corresponds to roughly $1.0 \times 10^{-6}\,\mathrm{g\,cm}^{-3}$. Although Chapter 4 used very low density plasmas to simulate the VCP they were still not at the experimentally reported values[16]. The staged gas-puff Z-pinch provides a good platform to test the role of AR on ETI growth. A density of $1.0 \times 10^{-6}\,\mathrm{g\,cm}^{-3}$ is on the edge of simulation capability for nanosecond time scales and micro metre spatial scales[10]. The proposed concept from Narkis et al. [6] investigates an experiment conducted on the Zebra pulsed-power driver which is capable of achieving 1 MA currents in 100 ns. The use of AR should be validated against experiments of the model proposed by Narkis et al. [6], but comparing to this semi-analytical model would be a first step to investigate AR in gas-puff Z-pinches. Additionally, upon further consultation with the author, the estimated current density is approximately $1.0 \times 10^{7}\,\mathrm{A\,cm}^{-3}$ at a modest 780 kA!

Rahman et al. [15] preformed experiments on the Zebra facility using Ar and Kr gas-puff staged Z-pinches with deuterium as fuel. The experiments were conducted both with and without an axial magnetic field. Figure 5.5 shows the result without an axial field in which there are significant MRT fingers that have developed and are more noticeable in the krypton shots. Figure 5.6 shows the radiographs when an axial magnetic field is present resulting in

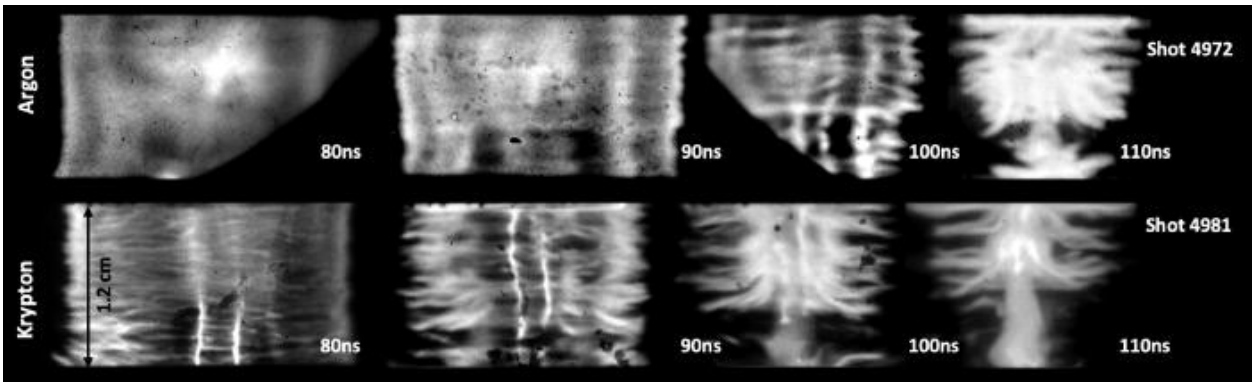

Figure 5.5: These radiographs are from Figure 7 of Rahman et al. [15] displaying a gas-puff Z-pinch when an axial field is absent for argon (top row) and krypton (bottom row).

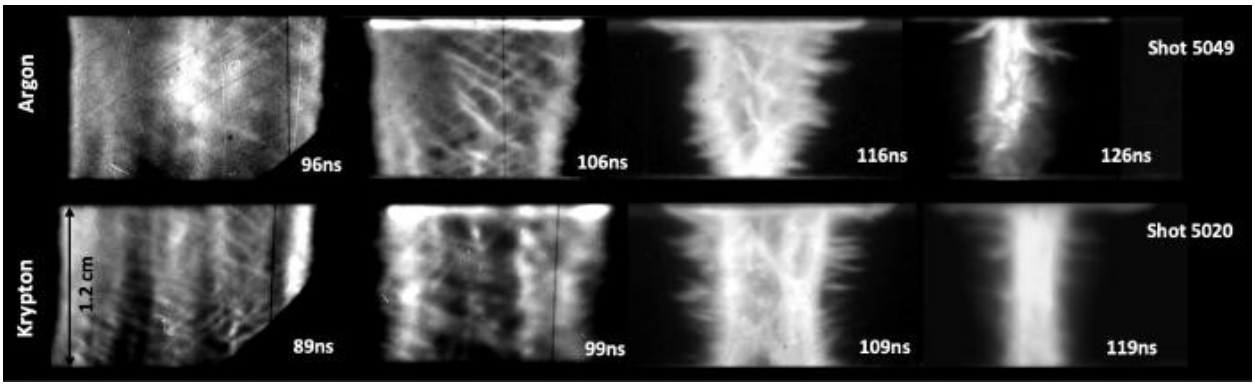

Figure 5.6: These radiographs are from Figure 8 of Rahman et al. [15] displaying the result of using an axial field.

two key observations. First, without an axial field larger convergence ratios are achieved due to the lack of additional pressure through magnetic flux compression. Second, the magnitude of MRT growth with the axial magnetic field is significantly reduced, which was one of the main benefits of using axially magnetized cylindrical loads[17]. Future work can benefit from using the semi-analytical model from Narkis et al. [6] to verify the setup of a simulated gas-puff staged Z-pinch, followed by using the data from Rahman et al. [15] to validate the simulation and to understand the accuracy of AR models in these regimes.

The helical structure in Figure 5.6 can be compared between simulations using AR in resistive-MHD for ETI growth and $\mathbf{J} \times \mathbf{B}$ in Hall-MHD for an axially magnetized current-carrying VCP. ETI has the aforementioned filamentation and striation form of growth corresponding to azimuthally and axially growing modes, respectively. AR has a dependence on the local magnetic field which changes the transition from one form of ETI to another and could provide an explanation for the helical structure's origin. Seyler et al. [18] determined the helical structure originates from the $\mathbf{J} \times \mathbf{B}$ force in Hall-MHD simulations of magnetized current-carrying VCP, but there were assumptions on the VCP resistivity such

that the simulation resulted in a match to the experimental observations of Awe et al. [19]. A study of the helical structure origin using an axially magnetized gas-puff staged Z-pinch would provide novel insight and potentially validate the findings of Seyler et al. [18].

Bibliography

[1] RL Masti, CL Ellison, JR King, PH Stoltz, and B Srinivasan. Cross-code verification and sensitivity analysis to effectively model the electrothermal instability. *High Energy Density Physics*, 38:100925, 2021.

[2] USIM. Usim version 3.0. *Tech-X Corp.*, 2019.

[3] DR Welch, N Bennett, TC Genoni, DV Rose, C Thoma, C Miller, and WA Stygar. Electrode contaminant plasma effects in 1.0e7-a z pinch accelerators. *Physical Review Accelerators and Beams*, 22(7):070401, 2019.

[4] Jack Hare, GC Burdiak, SN Bland, T Clayson, JWD Halliday, S Merlini, DR Russell, RA Smith, N Stuart, LG Suttle, et al. Generating and diagnosing turbulence in pulsed-power driven magnetised plasmas. *Bulletin of the American Physical Society*, 2020.

[5] J Narkis, HU Rahman, P Ney, MP Desjarlais, FJ Wessel, F Conti, JC Valenzuela, and FN Beg. Shock formation in ne, ar, kr, and xe on deuterium gas puff implosions. *Physics of Plasmas*, 23(12):122706, 2016.

[6] J Narkis, HU Rahman, JC Valenzuela, F Conti, RD McBride, D Venosa, and FN Beg. A semi-analytic model of gas-puff liner-on-target magneto-inertial fusion. *Physics of Plasmas*, 26(3):032708, 2019.

[7] SV Lebedev, IH Mitchell, R Aliaga-Rossel, SN Bland, JP Chittenden, AE Dangor, and MG Haines. Azimuthal structure and global instability in the implosion phase of wire array z-pinch experiments. *Physical review letters*, 81(19):4152, 1998.

[8] L G Suttle, G C Burdiak, C L Cheung, T Clayson, J W D Halliday, J D Hare, S Rusli, D R Russell, E R Tubman, A Ciardi, N F Loureiro, J Li, A Frank, and S V Lebedev. Interactions of magnetized plasma flows in pulsed-power driven experiments. *Plasma Physics and Controlled Fusion*, 62(1):014020, dec 2019. doi: 10.1088/1361-6587/ab5296. URL https://doi.org/10.1088/1361-6587/ab5296.

[9] S. V. Lebedev, A. Frank, and D. D. Ryutov. Exploring astrophysics-relevant magnetohydrodynamics with pulsed-power laboratory facilities. *Rev. Mod. Phys.*, 91:025002, Apr 2019. doi: 10.1103/RevModPhys.91.025002. URL https://link.aps.org/doi/10.1103/RevModPhys.91.025002.

[10] Robert L. Masti, Charles L. Ellison, William A. Farmer, Kurt Tummel, and Bhuvana Srinivasan. The effect of anomalous resistivity on the fast electrothermal instability. *In review*, to be published in 2021.

[11] DD Ryutov, MARK S Derzon, and M KEITH Matzen. The physics of fast z pinches. *Reviews of Modern Physics*, 72(1):167, 2000.

[12] Vladimir Ivanovich Oreshkin. Thermal instability during an electrical wire explosion. *Physics of Plasmas*, 15(9):092103, 2008.

[13] K. J. Peterson et al. Electrothermal instability growth in magnetically driven pulsed power liners. *Physics of Plasmas*, 19(9):092701, 2012. doi: http://dx.doi.org/10.1063/1.4751868. URL http://scitation.aip.org/content/aip/journal/pop/19/9/10.1063/1.4751868.

[14] Ryan D McBride and Stephen A Slutz. A semi-analytic model of magnetized liner inertial fusion. *Physics of Plasmas*, 22(5):052708, 2015.

[15] HU Rahman, E Ruskov, P Ney, F Conti, JC Valenzuela, N Aybar, J Narkis, FN Beg, E Dutra, and A Covington. Ar and kr on deuterium gas-puff staged z-pinch implosions on a 1-ma driver: Experiment and simulation. *Physics of Plasmas*, 26(5):052706, 2019.

[16] MR Gomez, RM Gilgenbach, ME Cuneo, CA Jennings, RD McBride, EM Waisman, BT Hutsel, WA Stygar, DV Rose, and Yitzhak Maron. Experimental study of current loss and plasma formation in the z machine post-hole convolute. *Physical Review Accelerators and Beams*, 20(1):010401, 2017.

[17] S. A. Slutz et al. Pulsed-power-driven cylindrical liner implosions of laser preheated fuel magnetized with an axial fielda). *Physics of Plasmas*, 17(5):056303, 2010. doi: http://dx.doi.org/10.1063/1.3333505. URL http://scitation.aip.org/content/aip/journal/pop/17/5/10.1063/1.3333505.

[18] CE Seyler, Matthew R Martin, and ND Hamlin. Helical instability in maglif due to axial flux compression by low-density plasma. *Physics of Plasmas*, 25(6):062711, 2018.

[19] T. J. Awe, K. J. Peterson, E. P. Yu, R. D. McBride, D. B. Sinars, M. R. Gomez, C. A. Jennings, M. R. Martin, S. E. Rosenthal, D. G. Schroen, A. B. Sefkow, S. A. , Slutz, K. Tomlinson, and R. A. Vesey. Experimental demonstration of the stabilizing effect of dielectric coatings on magnetically accelerated imploding metallic liners. *Phys. Rev. Lett.*, 116:065001, Feb 2016. doi: 10.1103/PhysRevLett.116.065001. URL https://link.aps.org/doi/10.1103/PhysRevLett.116.065001.